Two-Dimensional Kinematics and Dynamical Modelling of SLACS Lenses: Insights from Deep MUSE Observation

HANNAH CHARLOTTE TURNER

Two-Dimensional Kinematics and Dynamical Modelling of SLACS Lenses:

Insights from Deep MUSE Observations

Hannah Charlotte Turner

A Thesis presented for the degree of
Doctor of Philosophy

Centre for Extragalactic Astronomy
Durham University
United Kingdom

September 2024

Two-Dimensional Kinematics and Dynamical Modelling of SLACS Lenses:

Insights from Deep MUSE Observations

Hannah Charlotte Turner

Submitted for the degree of Doctor of Philosophy

September 2024

Abstract:

Early-type galaxies (ETGs) hold a wealth of information regarding galaxy evolution and the processes shaping the large-scale structure of the Universe. Within the ΛCDM cosmological framework, their observed properties serve as crucial tests for the hierarchical merging paradigm and, as the end products of this process, ETGs are sculpted by successive mergers of increasingly massive objects, offering a window into the entirety of galaxy formation and evolution. While lacking the grand, ordered disk and spiral arms characteristic of their more prominent counterparts, ETGs offer unique opportunities to study stellar populations, probe the nature of dark matter (DM), and constrain models of galaxy formation and interaction through their distinct morphologies and stellar kinematics.

The unification of mass and structure constraints from kinematic and dynamical modelling with the larger scale mass information from strong lensing allows great insight into the intrinsic properties of ETGs and the nature of DM. Access to a diverse range of spatial scales makes combined lensing and dynamical studies powerful in disentangling the stellar and the DM mass distributions of lens galaxies at their characteristic radii, and thus breaking the degeneracies between these two components.

We present results from the first spatially resolved kinematic and dynamical modelling analysis of the unique SDSSJ0946+1006 (‘Jackpot’) triple-source lens system, where a

single massive foreground $z = 0.222$ galaxy multiple-images three background sources at different redshifts. Deep IFU spectroscopic data were obtained using the MUSE instrument on the VLT, which, compared to previous single-slit observations, provides full azimuthal area coverage, high sensitivity (5 hour integration) and high angular resolution (0.5 arcsec FWHM). To account for the strong continuum contributions from the $z = 0.609$ source, a multiple-component stellar template fitting technique is adopted to fit to the spectra of both the lens galaxy and the bright lensed background arc simultaneously. Through this, we robustly measure the first and second moments of the two-dimensional stellar kinematics out to about 10 kpc from the centre of the lens, as well as resolving the inner profile inwards to ∼1 kpc. The two-dimensional kinematic maps show a steep velocity dispersion gradient and a clear rotational component. We constrain the characteristic properties of the stellar and DM mass components with a sufficiently flexible parameterised dynamical model and an imposed lensing mass and find a DM density slope of $\gamma = 1.73^{+0.17}_{-0.26}$, i.e. significantly steeper than an unmodified NFW profile ($\gamma = 1$) and consistent with a contracted DM halo. Our fitted models have a lensing-equivalent density slope of $\eta = 0.96 \pm 0.02$, and thus we confirm most pure lensing results in finding a near isothermal profile for this galaxy.

In a direct extension of this work, these kinematic and dynamical modelling techniques are generalised and applied to a broader sample of 9 additional SLACS early-type lens galaxies. The gravitational lens systems within our sample span a lens and source redshift range of $0.087 \leq z_{\rm lens} \leq 0.347$ and $0.324 \leq z_{\rm source} \leq 0.630$ respectively. This broader analysis yields a robust determination of the first and second moments of the two-dimensional stellar kinematics for the entire sample. Among the galaxies in this sample, J1250-0135 is a particularly noteworthy case. Previously excluded from sample studies due to the presence of bright spiral arms, which significantly hinder any accurate lensing analysis, this complex lens system now benefits from the wealth of information provided by MUSE IFU data. The intricate structured light is definitively confirmed to be at the redshift of the background source, allowing the 2D stellar kinematics of the foreground elliptical lens galaxy to be measured for the first time. Furthermore, we detect a clear signature of a kinematically-decoupled core in J1250, characterised by two counter-rotating components

at the lens redshift. We employ the anisotropic Jeans modelling framework and sample the posterior PDF for the model parameters under the assumptions of an NFW-like DM halo and a rigidly enforced lensing mass at the Einstein radius. We additionally explore models in which the imposed lensing mass is no longer rigidly enforced at the Einstein radius. Instead, it is permitted to vary, scaled by a free parameter, ζ. The inferred ζ for a significant fraction of lenses in our sample is greater than unity at about the 10% level, with an ensemble average across the galaxies of $\zeta = 1.22$ ranging between 1.00 and 1.88. A significant deviation of ζ from unity might indicate systematic uncertainties in the lensing or dynamical model, or limitations imposed by the quality of the available data. Thus, we discuss the implications of this finding and comment on possible deficiencies in the modelling techniques commonly used for analysing early-type lens galaxies.

Declaration

The work described in this thesis was undertaken between October 2020 and September 2024 while the author was a research student under the supervision of Dr. Russell Smith in the Centre for Extragalactic Astronomy at Durham University, England. No part of this thesis has been submitted for any degree or qualification at Durham University or elsewhere.

The material in this thesis is based on the analyses presented in two publications. Both publications share common analytical techniques, as described in Chapters 3 and 4. The results presented in Chapter 5 have been published as part of a paper in Monthly Notices of the Royal Astronomical Society (MNRAS) as Turner et al. (2024). The results in Chapter 6 are being prepared for publication in a subsequent paper in MNRAS.

This thesis makes use of public data collected by co-authors, but all stages of the data reduction and analysis, except where explicitly stated otherwise, are the work of the author.

All figures in this thesis were prepared by the author, or have been properly attributed in the figure caption.

Acknowledgements

First and foremost, I am forever grateful to my parents for their unwavering support and guidance throughout every stage of my life. You have instilled in me a relentless pursuit of excellence that I hope to always carry with me. Your constant encouragement has been instrumental in fostering my passions and aspirations. From the countless hours that we spent together deciphering my maths and physics homework at the dining room table, to standing in as film crew for my movies (film festival award winning, no less!), and even taking me to see a live rocket launch at NASA Kennedy Space Centre, you have continually stopped at nothing to support my dreams. Thank you for always encouraging me to be curious about the world. I owe everything to you both.

To my sister, Abby, my partner in crime from day one: thank you for always brightening my day. Through countless late nights fighting with telescope proposals and those frantic pre-conference panics, I've always been able to count on you. You are a constant source of joy and wisdom in my life (even when you're mardy), and I feel incredibly fortunate to have you on my team. Thank you for always explaining who popular musicians are, and what Gen Z slang means so that I can pretend that I'm still young. Thanks for being the best pal, advisor, second half to our comedic duo, therapist, confidante and gossiper that I could have asked for.

I also wish to thank Giovanni, without whom I would not have made it to the end of this PhD. Thank you for inspiring me each day to be a better scientist and for your tireless support. Thank you for listening with an ungodly amount of patience to my (somewhat regular) complaints, and for the countless memories that we have shared together so far,

filled with good food and great adventures. Thank you for getting me through the bad times, and for making the good times so much better. Here's to surely the greatest collaboration to come out of EAS 2022. *Grazie mille per tutto; non avrei potuto farlo senza di te.*

My time as a PhD student would not have been the same had I not met such an incredible group of friends along the way. Carolina, Filip, Martina, Scott, Thomas; thank you for being the source of so much laughter and warm memories. I consider myself very fortunate to have been surrounded by such an incredible group of people over the years. Thank you for the gossip, the cheese and wine nights, the broken hiking boots, and most importantly, the stories. I'm so grateful for having met you and I know that you will all go on to do amazing things.

Finally, I extend my sincerest gratitude to my supervisor, Dr. Russell Smith, for his continual support and mentorship throughout the past 4 years. Thank you for listening, with no small amount of patience, to my silly questions over the years, and for treating them as though they weren't quite so silly. Thank you for all of the scribbles in red pen on my drafts, and for pushing me to set high standards. I truly feel as though I have become a much more skilled and confident scientist under your supervision. Your seemingly endless source of knowledge, along with your encouragement, have been invaluable in helping me to reach this milestone.

This thesis is dedicated to you all.

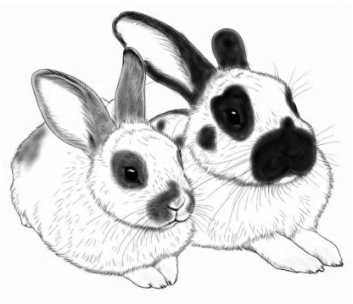

The rightful co-authors of this thesis

Contents

List of Figures

List of Tables

CHAPTER 1

Introduction

Equipped with his five senses, man explores the universe around him and calls the adventure Science

~ **Edwin Hubble**

1.1 Galaxy Morphological Classifications

The quest to categorise the vast tapestry of galaxies (massive systems of stars, interstellar gas, dust, and dark matter (DM) bound together by gravity) in the cosmos has a rich history, intricately woven with the evolution of telescopic power and our deepening understanding of galactic formation. Galaxy morphological classification, the visual classification of galaxies based on their shape and structure, serves as a foundational tool for astronomers. It underpins our understanding of galactic formation, evolution, and the interplay between structure and function. Far from being a mere aesthetic exercise, by systematically dissecting a galaxy's visual characteristics, we unveil profound insights into its formation history, evolution, and internal dynamics.

Early attempts relied on basic visual descriptions, but the 20^{th} century witnessed a paradigm shift with the introduction of the Hubble sequence (Hubble, 1926). This system and its

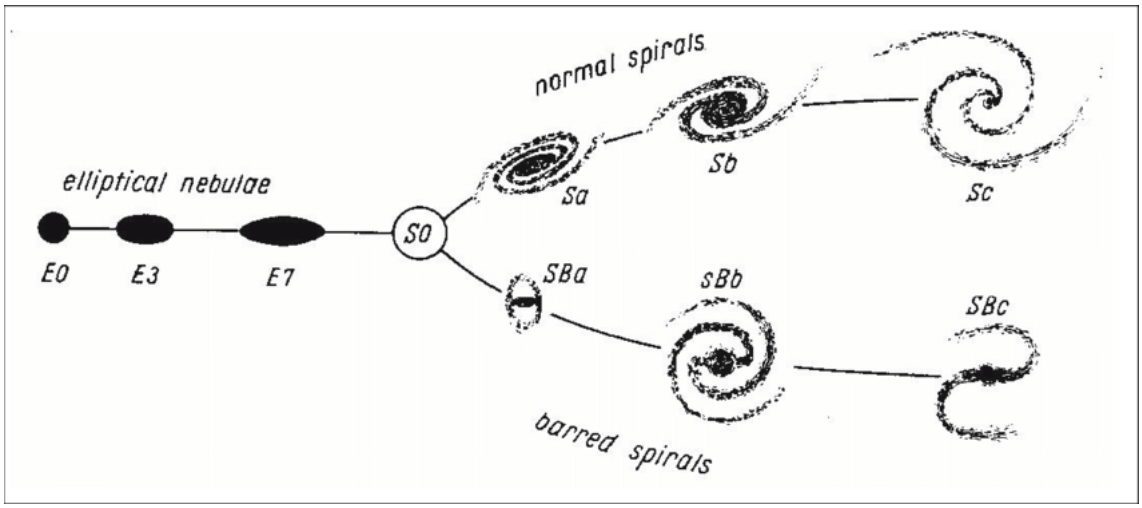

Figure 1.1
The Hubble tuning fork. Image credit: NASA/STScI

subsequent refinements (de Vaucouleurs, 1959; Sandage, 1961), illustrated in Figure 1.1, remains the most widely used today and divides galaxies into three primary morphological types:

- **Elliptical galaxies, *E*:** These galaxies are characterised by their smooth, elliptical shapes and lack of any prominent structure or star formation. They are further classified based on their apparent ellipticity, ranging from E0 (nearly spherical) to E7 (highly elongated), where the specific ellipticity is dependent on the ratio of the semi-major and semi-minor axes.

- **Spiral Galaxies, *S/SB*:** Spiral galaxies generally exhibit a central stellar bulge encircled by a flattened, rotating disk of stars and interstellar medium, characterised by the presence of prominent spiral arms. They are further divided into two main subtypes: normal spirals (S) and barred spirals (SB). Barred spirals are distinguished by a prominent central bar-shaped structure that extends from the galactic bulge, with the spiral arms originating from the ends of this bar. Both subtypes are classified according to the detailed appearance of their spiral structures, ranging from tightly wound, smooth arms and a prominent central bulge (Sa/SBa) to loosely wound spiral arms that are discernible as individual populations and a less prominent, fainter bulge (Sc/SBc).

- **Lenticular galaxies, *S0*:** This intermediate galaxy class features a bright central bulge, resembling that of an elliptical galaxy, encircled by an extended, disk-like structure. However, unlike spiral galaxies, lenticular galaxies lack discernible spiral arms and exhibit minimal ongoing star formation within their disks.

Galaxies that deviate from the Hubble sequence due to their irregular structure, lacking a discernible disk-like or ellipsoidal morphology, are classified as irregular galaxies, *Irr*. Elliptical and lenticular galaxies are collectively classified as 'early-type' galaxies, while spiral and irregular galaxies are categorised as 'late-type' galaxies. The origin of the term 'early-type' lies with the common, yet erroneous, interpretation of the Hubble sequence (Baldry, 2008). This assumes a chronological evolutionary progression from elliptical to lenticular and then to spiral galaxies, despite Hubble unequivocally stating that no such evolutionary implication was intended.

1.2 Early-Type Galaxies: An Overview

Early-type galaxies (ETGs) are widely regarded as the products of violent and disruptive processes primarily driven by a complex interplay of mergers and interactions within a hierarchically structured Universe. The structural characteristics of the most massive elliptical galaxies provide a window onto the primordial stages of galaxy formation, the evolution of galactic structures, and the role of mergers and interactions in shaping the Universe. The currently-popular 'two-phase' formation history of such galaxies (e.g. Oser et al., 2010) – with an early starburst-driven phase and subsequent accretion through mergers – offers a vital framework for understanding the assembly and evolution of galaxies, and the distribution of stars and DM within them.

ETGs are predominantly comprised of stellar populations that are significantly older with less massive stars, and that are redder than those observed in spiral galaxies. Star formation within them is generally minimal, although sporadic bursts of star formation may occur during mergers with other galaxies. They are typically enveloped within a sparse

interstellar medium, and are frequently accompanied by extensive populations of globular clusters. ETGs constitute a substantial fraction ($\sim 40\%$) of the total stellar mass density in the Universe (Fukugita et al., 2007; Bernardi et al., 2010) and exhibit a diverse range of sizes, encompassing dwarf ellipticals with mere tens of millions of stars to supergiants that dominate their respective galaxy clusters.

1.2.1 The Formation and Evolution of Early-Type Galaxies

The observed disparity in the dynamical structure of ETGs compared to their more ordered disk-dominated counterparts unequivocally suggests a more violent formation history. Indeed, all prevailing theories regarding the formation of ETGs posit a pivotal role for violent relaxation during some phase of their evolutionary trajectory. The term "violent relaxation" here pertains to a relaxation mechanism that describes the rapid evolution of an N-body system that has coalesced in a configuration substantially deviating from equilibrium. During the process of violent relaxation, the orbits of individual stars undergo significant transformations due to the alterations in the system's gravitational potential (Lynden-Bell, 1967). The observed dynamical structure of ETGs, characterised by their chaotic kinematics and the lack of a discernible disk, aligns with a formation paradigm predominantly shaped by such violent processes.

The formation and evolution of ETGs, despite their ostensibly simple appearance, remains somewhat unclear. While the ΛCDM cosmological paradigm (e.g. Spergel et al., 2003, 2007; Komatsu et al., 2011) offers a widely accepted framework for galaxy formation, it remains incomplete in explaining certain observational phenomena. Prior to the establishment of the contemporary structure formation paradigm, two competing scenarios emerged to explain the genesis of elliptical galaxies: the monolithic collapse scenario and the major merger scenario. The former posits that ETGs formed rapidly in a primordial epoch through the dissipational collapse of gas clouds, subsequently undergoing only passive evolution. In contrast, the merger scenario proposes that stars initially form within galactic disks, and elliptical galaxies arise from the coalescence of these disk-dominated

systems.

Driven by the empirical observation that elliptical galaxies appear to exhibit a remarkable degree of homogeneity, characterised by uniformly old stellar populations, the monolithic collapse scenario (Larson, 1969) posits galaxies that formed the majority of their stars in a single, intense burst of star formation at high redshift, subsequently undergoing passive evolution of their stellar populations to the present epoch (Partridge & Peebles, 1967; Larson, 1975). The monolithic collapse model offers a compelling explanation for the observed tightness of the fundamental scaling relations exhibited by ETGs as well as the evolution of these relations with redshift, but lacks a cogent explanation for the observed mass and environmental dependencies of stellar formation histories and is incompatible with the empirically determined sizes of $z \sim 1.4$ ellipticals (e.g. Daddi et al., 2005; Trujillo et al., 2006). Furthermore, to ensure consistency with the observed size of ETGs, the primordial collapse within the monolithic collapse scenario must be exceptionally dissipative. This dissipation naturally gives rise to the formation of radial gradients in the metallicities and ages of the resultant stellar populations. According to this model, star formation commences ubiquitously during the collapse phase, with stars remaining in orbit with minimal net inward motion. In contrast, the gaseous component continues to contract towards the galactic center due to dissipative processes, becoming enriched by the evolving stellar populations (Arimoto & Yoshii, 1987). Consequently, stars that form at later epochs near the galactic nucleus exhibit higher metallicities and are somewhat younger than those that formed earlier in the more peripheral regions. Overall, monolithic collapse models tend to generate metallicity gradients that are excessively steep (e.g. Larson, 1975).

In contradistinction, the major merger scenario (Toomre & Toomre, 1972) postulates ETGs arising from the coalescence of two or more progenitor disk galaxies. This proposition is substantiated by empirical observations, which reveal that star formation in the Local Universe is predominantly confined to spiral galaxies and starburst systems, while galaxy mergers are indeed observed. Moreover, numerical simulations (e.g. Farouki & Shapiro, 1982; Negroponte & White, 1983) demonstrate that the merger of two stellar disks can result in galaxies exhibiting structural and photometric properties analogous to contemporary

ellipticals.

Despite having proven effective in explaining many global observed properties of ETGs, the merger scenario encounters discrepancies with certain empirical findings. Notably, luminous ellipticals consistently exhibit relatively modest ellipticities, typically less than or equal to 0.3, a characteristic that stands in contrast to simulations predicting that the majority should possess ellipticities exceeding 0.3. Furthermore, the remnants generated by the mergers of purely stellar disks often exhibit insufficient central concentration, characterised by constant density cores that are substantially larger than those observed in bright ellipticals (e.g. Cox et al., 2006). Dissipational mergers typically more effectively replicate observational data (e.g. Burkert et al., 2008). The processes of gas dissipation and associated star formation yield remnant galaxies that exhibit more compact, spheroidal morphologies, possess higher central velocity dispersions and rotational velocities, and demonstrate a more isotropic dynamical structure compared to their non-dissipational counterparts. Notwithstanding that, however, dissipational mergers encounter challenges in reproducing remnants characterised by slow rotation and boxy isophotes. In particular, the presence of a dissipative component inevitably leads to the formation of a steep central cusp, which not only deviates from the observed shallow cusps in massive ellipticals but also destabilises the box orbits responsible for the boxiness of the isophotes (see Section 1.2.2.1).

The widely accepted ΛCDM paradigm (e.g. Spergel et al., 2003, 2007; Komatsu et al., 2011) posits a hierarchical merger framework predicated upon the validity of general relativity on cosmic scales in which smaller galaxies gradually merge and grow over time from the epoch of reionization to the present day, offering our most comprehensive picture of galaxy formation. The ΛCDM model successfully describes observations of the Universe on ~Mpc scales and above (see e.g Bullock & Boylan-Kolchin, 2017), such as the hierarchical formation of large scale structure (Anderson et al., 2014; Hildebrandt et al., 2017) and is consistent with the observed distribution of galaxies in the Universe, providing a natural explanation for the observed diversity of galaxy morphologies. The ΛCDM model incorporates three fundamental constituents: a cosmological constant, Λ,

accounting for dark energy and the observed accelerated expansion of the universe; the postulated cold dark matter, CDM, characterised by non-baryonic, collisionless matter moving at sub-light speeds; and ordinary baryonic matter. See Efstathiou (2024) for a review of the ΛCDM model and its contemporary challenges.

1.2.2 Basic Early-Type Galaxy Properties

One of the defining characteristics of ETGs is their high degree of homogeneity. They typically consist of stellar populations much older than those found in spiral galaxies, although sometimes with a younger component present (Trager et al., 2000), are preferentially located in massive dark matter haloes (e.g. Dressler, 1980), and are observed to adhere to a series of stringent, well-defined scaling relations that correlate their kinematic and photometric properties (e.g. Faber & Jackson, 1976; Visvanathan & Sandage, 1977; Djorgovski & Davis, 1987). According to their kinematic and photometric characteristics, ETGs can be broadly categorised into three distinct sub-classes based on their absolute magnitude in the B band. The most luminous ETGs ($M_B \lesssim -20.5$) typically exhibit minimal rotation, boxy isophotes, and relatively shallow central surface brightness profiles. In contrast, ellipticals of intermediate luminosity ($-20.5 \lesssim M_B \lesssim -18$) demonstrate a degree of rotational support, exhibit disky isophotes, and feature pronounced central surface brightness cusps. Finally, at the faint end ($M_B \gtrsim -18$), the preponderance of dwarf ellipticals and dwarf spheroidals exhibit negligible or no rotation and possess approximately exponential surface brightness profiles (e.g. Sandage & Binggeli, 1984; Kormendy & Djorgovski, 1989; Kormendy et al., 2009; Tolstoy et al., 2009).

1.2.2.1 Structural Properties

A foundational approach to characterising the morphology of galaxies involves examining their surface brightness profiles. The luminous distribution of a galaxy is described by the function $I(x, y)$, where I denotes the intensity, or surface brightness, measured in units of luminosity per unit area at the coordinate (x, y). This area can be expressed in either

physical units, such as square parsecs, or angular units, such as square arcseconds. To facilitate analysis, the intensity is frequently represented by a radially averaged function, $I(R)$. The total luminosity of a galaxy can then be determined by integrating this function over its spatial extent, such that

$$L_{tot} = 2\pi \int_0^\infty I(R) R dR \tag{1.2.1}$$

The Sérsic profile (Sérsic, 1963) is a versatile mathematical function that has become a standard tool for modelling the surface brightness profiles of galaxies and can be expressed as

$$I(R) = I_0 \exp\left[-\beta_n \left(\frac{R}{R_e}\right)^{1/n}\right] = I_e \exp\left[-\beta_n \left\{\left(\frac{R}{R_e}\right)^{1/n} - 1\right\}\right], \tag{1.2.2}$$

where I_0 is the central surface brightness, β_n can be well-approximated by $2n - 0.32$ for $n \gtrsim 1$, R_e is the half-light radius, n is the Sérsic index that determines the slope of the profile (see Figure 1.2) and $I_e = I(R_e)$.

Most galaxies are fit by Sérsic profiles with indices in the range $0.5 < n < 10$. The best-fit value of n correlates with the physical properties of the galaxy, such that galaxies with high Sérsic indices are typically more massive and more luminous than those with low Sérsic indices (Caon et al., 1993; Young & Currie, 1994). Setting $n = 4$ gives the de Vaucouleurs profile (de Vaucouleurs, 1948), which serves as a good approximation for typical ETGs.

In conjunction with their surface brightness profiles, the isophotes of ETGs are frequently employed to characterise their structural properties. Isophotes represent contours of uniform surface brightness, thereby revealing the galaxy's shape and symmetry. The common approach to modelling the isophotes of ETGs involves fitting a series of ellipses, each characterised by its minor-to-major axis ratio, b/a, and its position angle. Detailed surface brightness modelling shows that the isophotes of ETGs frequently deviate from a strictly elliptical form, often exhibiting variations across the system. To quantify these deviations from elliptical symmetry, the angular intensity along the best-fit ellipse is

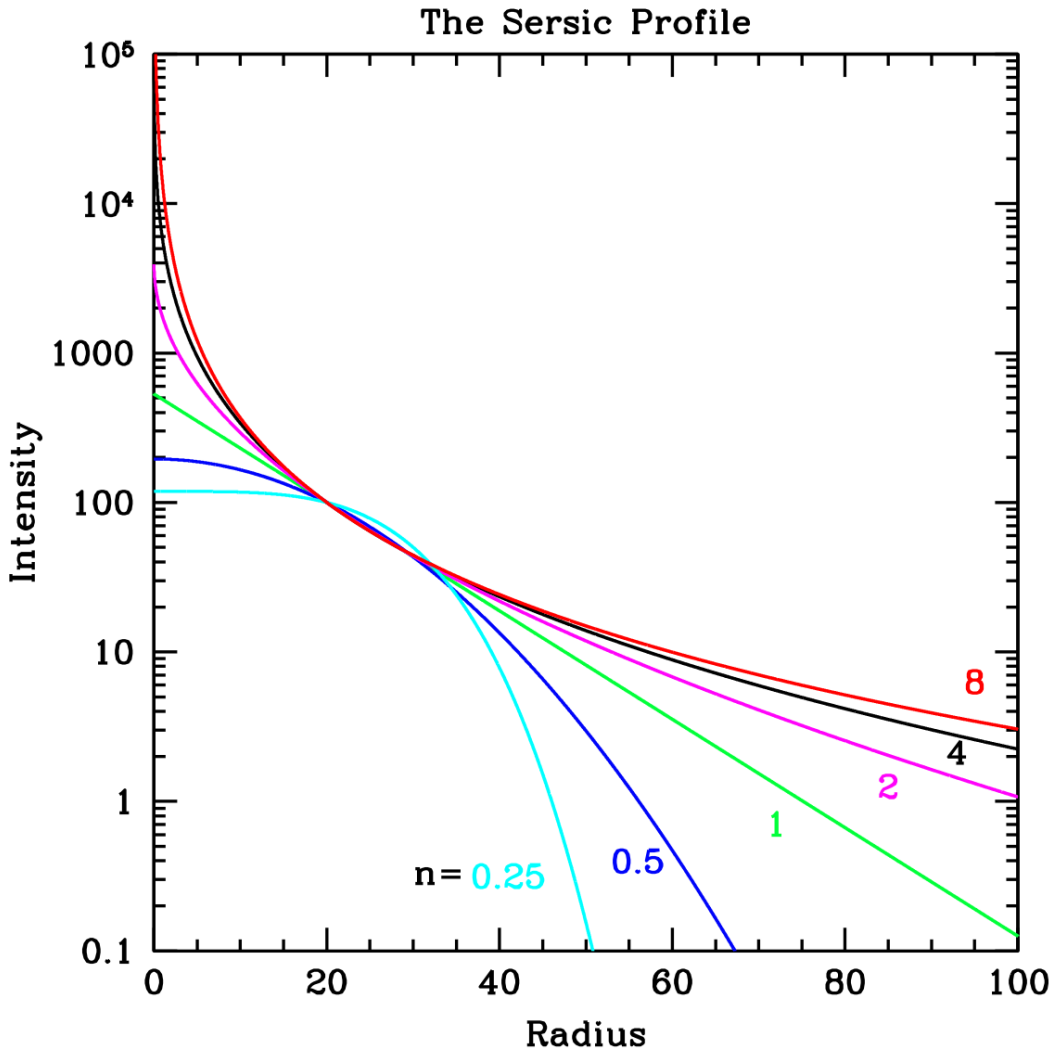

Figure 1.2
Sérsic profiles for varying Sérsic indices values. Image credit: Peng et al. (2010).

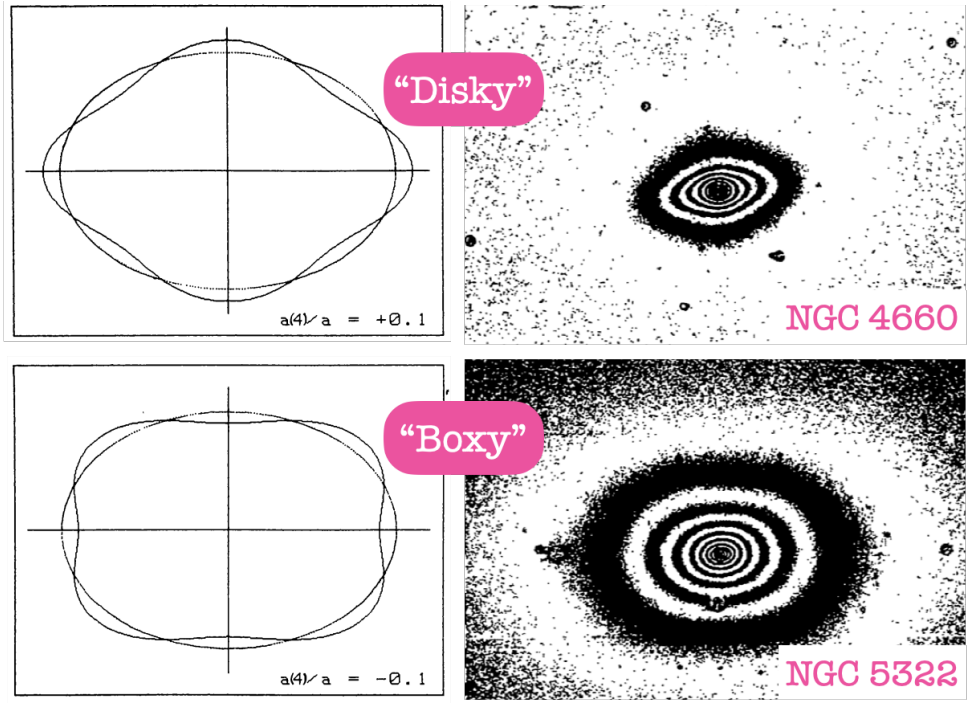

Figure 1.3
Examples of "boxy" and "disky" galaxy isophotes from Bender et al. (1988).

expanded in Fourier series (e.g. Bender & Moellenhoff, 1987; Bender et al., 1988; Hao et al., 2006; Goullaud et al., 2018), such that

$$I(\theta) = I_0 + \sum A_n \cos n\theta + B_n \sin n\theta, \tag{1.2.3}$$

where I_0 is the surface brightness averaged over the ellipse and A_n and B_n are the higher order Fourier coefficients. Non-zero A_n and B_n for $n \geq 3$ denote deviations from pure ellipticity. The most significant Fourier coefficient, however, is when $n = 4$, which quantifies deviations along the major and minor axes. Such $n = 4$ multipoles may result in a positive A_4 value, giving rise to a "disky" ETG, suggesting a flattened structure with a prominent central bulge, or in a negative value of A_4, which produces a "boxy" or rectangular shape, indicative of a more triaxial structure, as illustrated in Figure 1.3.

In addition to the ellipticity, variations in the position angle of isophotes as a function of radius may arise. This phenomenon is known as isophote "twisting" and is explored in further detail in Section 1.2.3.

1.2.2.2 Kinematics and Dynamics

ETGs are prime examples of collisionless systems and, as we will explore in Section 1.3, their dynamics are intimately linked to their mass distributions, which can be probed via spectral analysis. Through long-slit spectroscopy, the mean velocity and velocity dispersion can be measured. The characteristic velocity dispersion profile for ETGs shows a pronounced peak at the galaxy centre that flattens out at larger radii.

ETG rotation velocities are much too small to explain their observed flattening (Bertola & Capaccioli, 1975; Illingworth, 1977), and thus their kinematics are thought to be largely dominated by chaotic motions, with $\sigma > v_{\rm rot}$. Observationally, this can be characterised by the ratio of maximum line-of-sight streaming motion relative to the mean velocity of the galaxy, $v_{\rm m}$, to the average value of the line-of-sight velocity dispersion, $\bar{\sigma}$.

It has also been shown that the dichotomous nature observed in the photometric properties of ETGs is mirrored in their kinematic characteristics (Davies et al., 1983). While luminous, boxy ETGs demonstrate minimal rotation and are predominantly supported by anisotropic velocity dispersions, their less luminous, disky counterparts typically exhibit substantially higher rotational velocities, often consistent with a purely rotationally flattened scenario. This is particularly highlighted in Figure 1.4, which demonstrates the systematically divergent kinematics of disky and boxy ellipticals.

Despite the historical characterisation of ETGs as relatively simple, dynamically relaxed systems, more recent studies of their individual kinematic structures are increasingly revealing a greater degree of complexity. These deviations from the canonical paradigm offer valuable insights into the formation and evolution of these galaxies.

Approximately 25% of all elliptical galaxies exhibit inner regions that are kinematically decoupled from their host galaxy (Kormendy & Djorgovski, 1989). These kinematically decoupled cores (KDCs) represent central stellar components with kinematic properties that are distinct from those of the main body of the galaxy (e.g. Bender et al., 1988; McDermid et al., 2006; Krajnović et al., 2011; Toloba et al., 2014). In extreme cases, the KDC may even exhibit counter-rotation relative to the outer regions and, in the case of fast-rotating

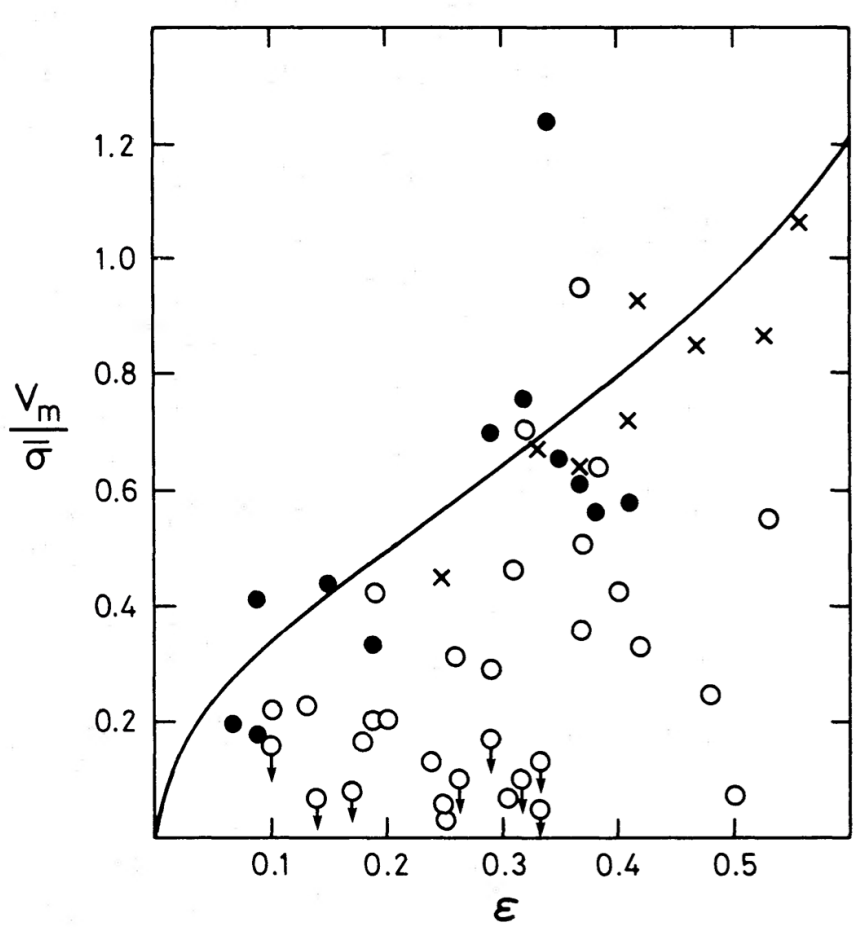

Figure 1.4

The ratio $v_m/\bar{\sigma}$ against ellipticity, ϵ, from Davies et al. (1983). Ellipticals with $M_B > -20.5$ are shown as filled circles, ellipticals with $M_B < -20.5$ as open circles, and the bulges of disk galaxies as crosses. The solid line marks the expected relation for an oblate galaxy flattened by rotation.

ETGs, often appears to harbour distinct stellar populations characterised by high metallicity (Bender & Surma, 1992; McDermid et al., 2006). This is usually attributed to dynamically distinct subsystems that represent remnants of accreted companions. Notwithstanding, KDCs can also arise from the projection of circulating orbits within a triaxial potential, without necessarily requiring the core to constitute a separate dynamical subsystem (Statler, 1991).

In the innermost regions of the majority of nearby ETGs, as well as most spirals, a pronounced increase in velocity dispersion is observed that cannot be adequately explained solely by the gravitational influence of the visible stellar populations. This phenomenon is widely attributed to the presence of a central supermassive black hole (e.g. Gebhardt et al., 2000a; Valluri et al., 2005; van den Bosch et al., 2012). Indeed, it is widely believed that such black holes are ubiquitous within galaxies exhibiting a substantial spheroidal component. Furthermore, their masses exhibit a well-established empirical correlation with the velocity dispersion of their host galaxies, often referred to as the M-sigma relation. This relationship can be approximated by the power law $M_{\rm BH} \propto \sigma^n$, where the slope parameter, n, exhibits variability within the range of 3.75 to 5.3, attributable to systematic discrepancies in the velocity dispersion measurements (e.g. Gebhardt et al., 2000b; Tremaine et al., 2002; Thomas et al., 2016; van den Bosch, 2016).

1.2.3 Complex Morphologies: Radial Variations in the Form of Gradients and Twists

A number of studies have observed a significant fraction of ETGs whose isophotes imply complex morphological structures characterised by radial variations in the form of gradients and twists (e.g. Kormendy & Djorgovski, 1989; Cappellari, 2002; Hao et al., 2006; Sonnenfeld et al., 2018).

Systematic variations in position angle as a function of radius, referred to as isophotal twists (depicted in Figure 1.5), are a frequently observed phenomena (Jedrzejewski, 1987; Kormendy & Djorgovski, 1989, etc.). These twists are generally interpreted as

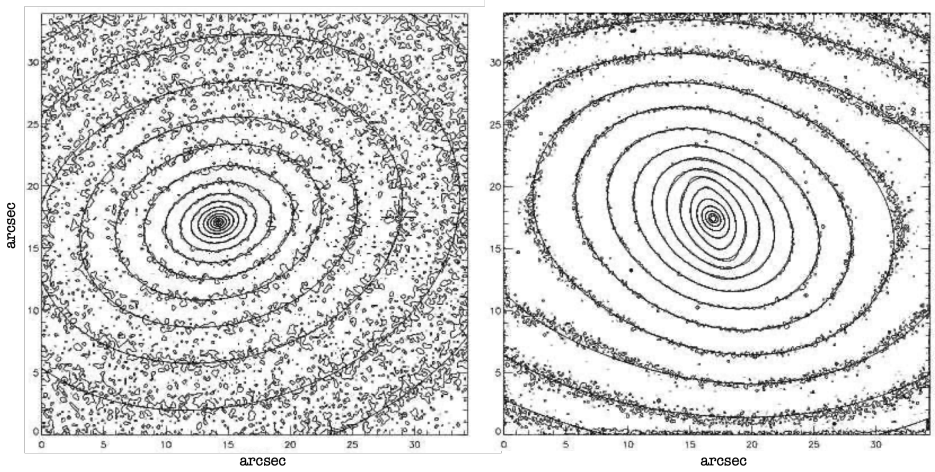

Figure 1.5
Example isophotal contour maps of the F814W images of M32 (left) and the barred S0 galaxy NGC 2950 (right) from Cappellari (2002). Sharply twisted and non elliptical isophotes are clearly present in the image of NGC 2950.

direct indicators of triaxiality, in contrast to oblate or prolate configurations, and are often associated with radial variations in the intrinsic axis ratios of the galaxy (King, 1978). Physically, the observed twists in ETGs are hypothesised to originate from either tidal interactions (e.g. Goullaud et al., 2018; Amvrosiadis et al., 2024) or the inherent two-component nature of many ellipticals (Nieto et al., 1992). Moreover, the frequent misalignment between the kinematic and photometric position angles of real galaxies provides additional evidence for their triaxial structures. This triaxiality presents a fundamental challenge in constructing and interpreting dynamical models of ETGs, as many such models are constrained to axisymmetric mass distributions (e.g. Jeans anisotropic models; Cappellari, 2008), and serves as the motivation for the triaxial implementation of dynamical models (e.g. Pilawa et al., 2022; Quenneville et al., 2022), which are able to account for such features.

While ETGs are generally characterised by global properties indicative of predominantly old, massive, red, and metal-rich stellar populations, in-depth investigations of stellar populations within individual galaxies often reveal evidence of radial gradients. Numerous observations have demonstrated a tendency for ETGs to exhibit a reddening trend toward their central regions. Two primary explanations for these gradients have been invoked in the literature: either the central regions of these galaxies are characterised by older or more

metal-rich stellar populations (e.g. Davies et al., 1993; Trager et al., 2000; Tortora et al., 2010; Sonnenfeld et al., 2018), or there may exist a radial gradient in the stellar initial mass function ($IMF_\star$; Martín-Navarro et al., 2015; La Barbera et al., 2017; van Dokkum et al., 2017; Smith, 2020, etc.).

When investigating gradients in stellar age or metallicity, a common approach involves examining the variations in stellar absorption features within the integrated spectra of ETGs. Hydrogen lines, indicative of young stellar populations, exhibit diminishing strength as the stellar population ages. Conversely, lines associated with magnesium, for example, demonstrate heightened strength in metal-rich populations. Studies of ETG absorption line reveal a diverse array of behaviors, suggesting a multiplicity of formation scenarios that can culminate in markedly distinct metallicity structures (Kuntschner et al., 2006; Greene et al., 2015).

In addition, the precise determination of the $IMF_\star$ within massive ETGs constitutes a prominent unresolved challenge within astrophysics. Acquiring more stringent constraints on the $IMF_\star$ will facilitate a better comprehension of star formation processes in extreme environments, such as the cores of massive galaxies. Furthermore, the $IMF_\star$ currently represents an important systematic source of uncertainty in the measurement of galaxy stellar masses.

The structural complexities observed in the light distribution of galaxies, both in the form of gradients and twists, are anticipated to be mirrored in their underlying mass distributions. As detailed in Section 1.5, the phenomenon of strong gravitational lensing serves as a potent instrument for understanding the mass distribution of galaxies acting as lenses. Leveraging the power of strong lensing, numerous contemporary investigations have demonstrated compelling evidence for angular complexity in the mass distribution, leading to interesting implications for our understanding of the structure and formation of ETGs (e.g. Powell et al., 2022; Van de Vyvere et al., 2022; Cohen et al., 2024; Nightingale et al., 2024; Stacey et al., 2024).

1.2.4 The Dark Side of Early-Type Galaxies

ETGs have been indirectly observed to reside within extensive DM haloes. The distribution of the DM within these haloes can exhibit variability, with some galaxies displaying more concentrated cores and others characterised by more extended profiles. These haloes are understood to play a pivotal role in the formation and evolution of galaxies, providing the gravitational potential that serves to coalesce visible matter.

However, prior to exploring the role of DM within ETGs, it is imperative to first establish a foundational context by examining a concise historical overview of DM research.

1.2.4.1 A Brief History of Dark Matter

In his investigations of the Coma Cluster of galaxies, Zwicky (1933) observed an anomalous velocity dispersion among the cluster members, indicative of a substantial unseen mass component that he termed *dunkle Materie* (German for dark matter). This observation, while previously noted by Hubble & Humason (1931), was further substantiated by Zwicky's application of the virial theorem to estimate the cluster's total mass, revealing a discrepancy of approximately 400 times between the visible and inferred mass.

Zwicky's *dunkle Materie* is frequently cited in the literature as the inaugural usage of the term dark matter. This is, however, not true. The phrase actually made its debut many years prior when, drawing inspiration from Kelvin (1904)'s appendix to a book on a series of lectures from 1884 – where he mused that "*Many of our supposed thousand million stars, perhaps a great majority of them, may be dark bodies*" – Poincare (1906) explicitly introduced the concept of *matière obscure* (French for dark matter).

It was not until the 1970s, aided by the substantial advancements in spectroscopic observations and the consequent robust galaxy rotation curve measurements, that the hypothesis of dark matter gained widespread acceptance. Analyses of spiral galaxy rotation curves (e.g. Roberts & Rots, 1973; Rubin et al., 1978, 1980) demonstrated profiles that flatten at large radii, deviating from the anticipated behavior if the visible stellar and gaseous components

constituted the sole mass within the system. This discrepancy provided compelling evidence for the presence of DM haloes (Einasto et al., 1974; Ostriker et al., 1974). Concurrent with these developments, a plethora of hypotheses were proposed concerning the potential nature of this DM component. These proposals encompassed a spectrum of possibilities, ranging from baryonic objects, such as brown dwarfs, white dwarfs, and black holes (e.g. White & Rees, 1978; Carr & Rees, 1984), to more exotic, elementary particles, such as massive neutrinos (e.g. Gershtein & Zel'dovich, 1966).

Unlike their spiral counterparts, where neutral hydrogen gas serves as a reliable tracer, ETGs lack simple dynamical tracers at large radii. Consequently, the unequivocal presence of DM haloes within ETGs remained a subject of conjecture for an extended period. As cosmological models increasingly advocated for the existence of DM haloes (e.g. Spergel et al., 2003), a compelling motivation emerged, yet direct observational evidence was lacking. This uncertainty persisted until the advent of surveys capable of probing extended kinematics and gravitational lensing phenomena. By the late 90s, the notion of universal density profiles for DM haloes, exemplified by the Navarro-Frenk-White (NFW) profile that characterises the variation of DM density with radial distance from the halo's centre (Navarro et al., 1997), had gained widespread acceptance within the scientific community. This NFW profile predicts DM haloes with an inner density profile that is well described as a power law with a slope of -1 and has served as a foundational framework for understanding the structural properties of DM haloes across a wide range of scales.

1.2.4.2 The Dark Matter Content of Early-Type Galaxies

As previously described, the gas rotation curves of spiral galaxies offer compelling evidence for them being found within extended dark haloes. In accordance with the standard paradigm of galaxy formation, it is anticipated that ETGs should be similarly enveloped by analogous dark haloes. However, empirical evidence regarding the presence of DM haloes in ETGs has historically proven challenging to obtain. This is primarily attributed to the paucity of mass tracers at radii greatly exceeding the effective radius, where the influence of DM dominates. Furthermore, the inherent degeneracies encountered

in interpreting projected data within the context of three-dimensional mass distributions for pressure-supported systems pose additional challenges. Among these degeneracies, the mass-anisotropy degeneracy (Binney & Mamon, 1982; Merritt, 1987; Gerhard, 1993; Treu & Koopmans, 2002b), must be broken. This degeneracy arises from the ambiguity between the total mass density profile and the anisotropy of the observed kinematics. Specifically, the observed stellar motions can be explained by different combinations of mass distribution and velocity anisotropy, which can lead to erroneous mass estimates. The observed velocity dispersion profile is not sufficient to determine the mass profile without hypotheses on the anisotropy of the stellar orbits. In simpler terms, you can't uniquely determine whether a galaxy is massive with isotropic orbits, or less massive with highly anisotropic orbits, based solely on observed stellar velocities. This is typically broken with the assumption of constant anisotropy, or even isotropic orbits. Nonetheless, a substantial body of empirical evidence, derived from extensive stellar dynamics studies (e.g. Bertin et al., 1994; Carollo et al., 1995; Rix et al., 1997; Gerhard et al., 2001; de Zeeuw et al., 2002; van den Bosch et al., 2008; Thomas et al., 2007, 2011; Cappellari et al., 2011; Sonnenfeld et al., 2012, etc.), clearly supports the existence of dark haloes hosting ETGs. These studies compellingly demonstrate that dark haloes are generally required in explaining the dynamical properties of massive ETGs.

As explored in detail in Section 1.5, strong gravitational lensing observations have also aided in unequivocally establishing the existence of DM haloes hosting individual massive ETGs, both independently and in conjunction with other observational probes. Lensing studies compellingly demonstrate that the mass enclosed within the Einstein radius surpasses the observable stellar mass. A particularly potent approach to detecting DM haloes involves leveraging stellar kinematics within the lens galaxy to ascertain the mass distribution in the high surface brightness regions within the effective radius, while simultaneously employing strong lensing to mitigate the mass-anisotropy degeneracy (e.g. Treu & Koopmans, 2004; Barnabè et al., 2009, and Chapters 5 and 6 of this thesis). In addition, weak gravitational lensing studies enable the characterisation of the outer regions of DM haloes within statistical samples of ETGs extending to intermediate redshifts (e.g. Gavazzi et al., 2007;

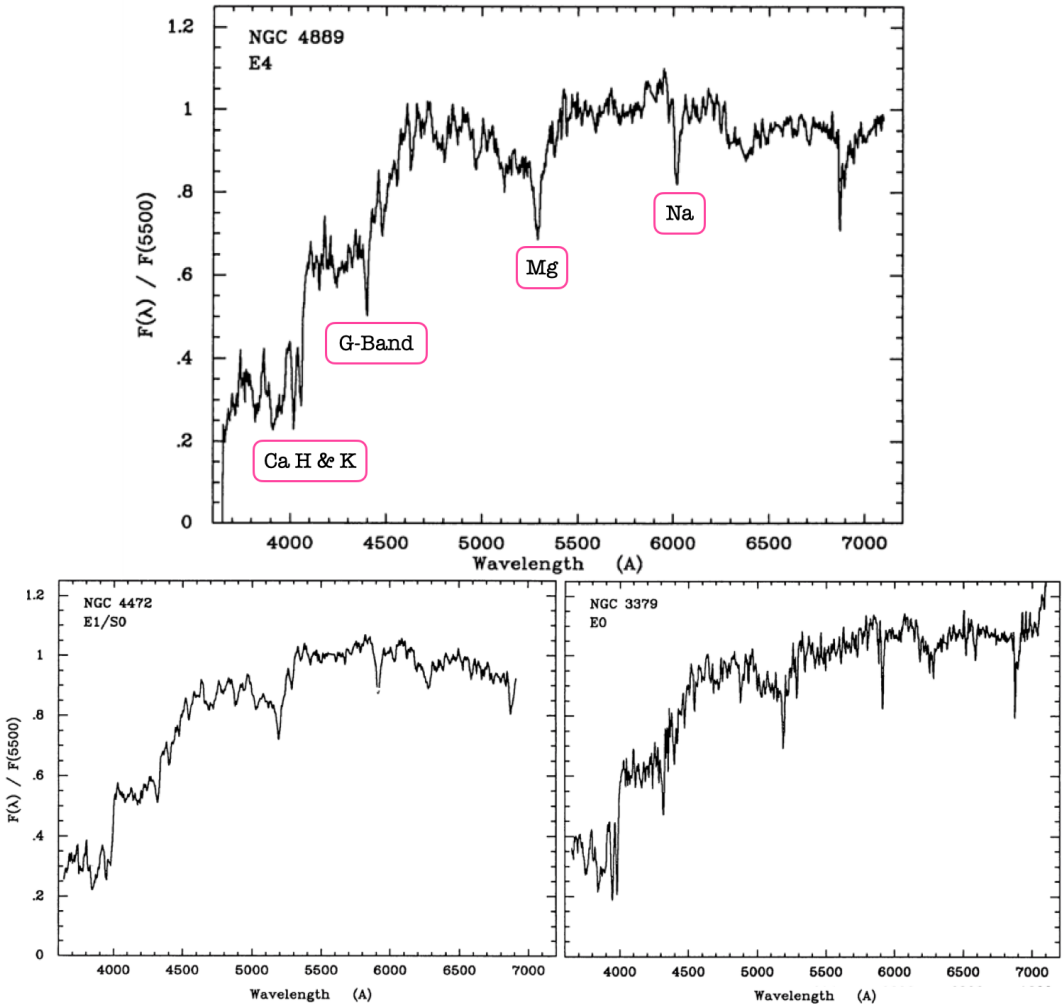

Figure 1.6
Example of 3 early-type galaxy spectra. Adapted from Kennicutt (1992).

Lagattuta et al., 2010; Auger et al., 2010a).

1.3 Spectroscopy: An Overview

Spectroscopic analysis plays a fundamental role in understanding the intrinsic physical properties of galaxies. For ETGs, spectroscopy provides valuable insights into their stellar populations, dynamical structure, and the scaling relations that govern them.

Galaxy spectra are generally characterised by a prominent continuum component, a smoothly varying component arising from the confluence of the individual spectra of the galaxy's constituent stars and other radiating matter. Against this backdrop, localised

absorption and emission features are superimposed. ETGs typically exhibit fairly homogeneous spectra, dominated by pronounced absorption lines indicative of an older stellar population, with prominent features including the calcium-H and -K lines, the G-band, and the magnesium and sodium lines. Due to their low star formation rates, ETGs generally display few, if any, emission lines. The integrated spectra of 3 example ETGs are shown in Figure 1.6.

At optical wavelengths, spectroscopic analysis is typically conducted by directing the light from a luminous target toward a spectrograph, where it is dispersed according to wavelength. For example, in multi-object fiber spectroscopy, exemplified by the Sloan Digital Sky Survey (SDSS, York et al., 2000), spectra of numerous objects within a shared field of view (FOV) are acquired simultaneously through the strategic placement of specialised optical fibers over individual targets. These fibers are subsequently connected to the spectrograph's pseudo-slit, facilitating the dispersion of light from each object into its constituent wavelengths. Such spectroscopic techniques yield composite spectra that that provide insights into the galaxy's properties as a whole, but inherently disregard the spatial distribution of a these properties within the circular aperture defined by the end of the fiber. In contrast, long-slit spectroscopy utilises a narrow, elongated aperture, facilitating the acquisition of spectra from objects situated along a designated line-of-sight. This approach enables the recovery of spatial information, albeit only along the slit, as it produces a distinct spectrum for each point of the target that intersects the aperture.

Two of the most fundamental properties discernible from a galaxy's spectrum are its redshift and its kinematics. The Doppler effect (Doppler, 1842) describes the phenomenon whereby the spectra of objects approaching an observer exhibit a blueshift, or a shortening of wavelength, therefore appearing bluer than the source light. Conversely, objects in motion away from the observer experience a redshift, characterised by a longer wavelength and described by

$$\frac{\lambda - \lambda_0}{\lambda_0} = \frac{v}{c}, \tag{1.3.1}$$

where λ and λ_0 are the observed and emitted wavelengths respectively, v is the galaxy's velocity and c is the speed of light.

In atomic physics, Doppler broadening is a phenomenon in which the spectral lines of an object are broadened due to the random thermal motion of the emitting or absorbing atoms. In the context of galaxies, Doppler broadening arises from the random motions of the stars and gas within the galaxy. The radial velocity of these constituents can be ascertained by measuring the Doppler width of spectral lines. In practice, this can be effectively achieved through the implementation of stellar template fitting software (e.g. PPXF; Cappellari & Emsellem, 2004; Cappellari, 2017), which work by fitting a series of template spectra to the observed spectrum, thereby extracting the moments of the line-of-sight velocity distribution. For a detailed description of stellar kinematic template fitting, see Chapter 3.

Expanding upon the seminal works of Slipher (1913, 1914, 1915, etc.), which not only documented the prevalence of redshift among observed galaxies but also described the methodology for determining their radial velocities, Hubble was able to derive his eponymous Hubble's Law (Hubble, 1929). When combined with the Doppler effect, this provides a key relationship between a galaxy's redshift, z, and distance from Earth, d, such that

$$v = H_0 d \quad \Rightarrow \quad z = \frac{H_0 d}{c}, \tag{1.3.2}$$

where H_0 is the Hubble constant.

As previously explored in Section 1.2.4.1, the discovery of galaxies exhibiting an excess of mass beyond that attributable to visible matter served as a cornerstone of early DM research. Central to this understanding was the study of galaxy kinematics, derived from the Doppler shift and broadening of galaxy spectral features. Measurements of the radial, or line-of-sight velocities from individual stellar spectra enable the measurement of a galaxy's velocity dispersion, σ, a statistical measure of the spread of stellar velocities within the galaxy. This offers valuable insights into the dynamical structure and mass distribution of the galaxy, as an estimation of its velocity dispersion can be employed to derive its mass through the application of the virial theorem, which can be expressed as

$$\frac{1}{2}\frac{d^2I}{dt^2} = 2K + U, \tag{1.3.3}$$

where I is the moment of inertia of the system, the time derivative of which is the *virial*. In order to deduce the *virial theorem*, we take the time derivative of the virial. K and U denote the total kinetic and potential energies respectively. For a bound system in equilibrium, the first term may be assumed to be zero, and thus the virial theorem can be given simply as

$$\langle K \rangle = -\frac{1}{2}\langle U \rangle. \tag{1.3.4}$$

In the case of an elliptical galaxy described by a spherical, isotropic model, it follows that the velocities of the constituent stars have an average squared value $\langle v_{\rm 3D}^2 \rangle = \sigma_{\rm 3D}^2 = 3\sigma_{\rm 1D}^2$, such that the kinetic energy is given by

$$\langle K \rangle = \frac{1}{2}m\langle v_{\rm 3D}^2 \rangle = \frac{3}{2}m\sigma_{\rm LOS}^2, \tag{1.3.5}$$

where $\sigma_{\rm LOS}$ denotes the velocity dispersion along the line-of-sight. Under the assumption of a total galaxy mass of M, the total potential energy can be given as

$$\langle U \rangle = -\frac{GMm}{r}. \tag{1.3.6}$$

Thus, in combining Equations 1.3.5 and 1.3.6 with the virial theorem, we obtain an expression that relates the total mass of a galaxy to the LOS velocity dispersion of its stars

$$M = \frac{3\sigma_{LOS}^2 r}{G}. \tag{1.3.7}$$

1.3.1 Integral Field Spectroscopy

Integral field units (IFUs) have fundamentally transformed the spectroscopic study of extended objects, such as nebulae, galaxies and clusters, by enabling the acquisition of spatially resolved spectra. This technique, known as integral field spectroscopy (IFS),

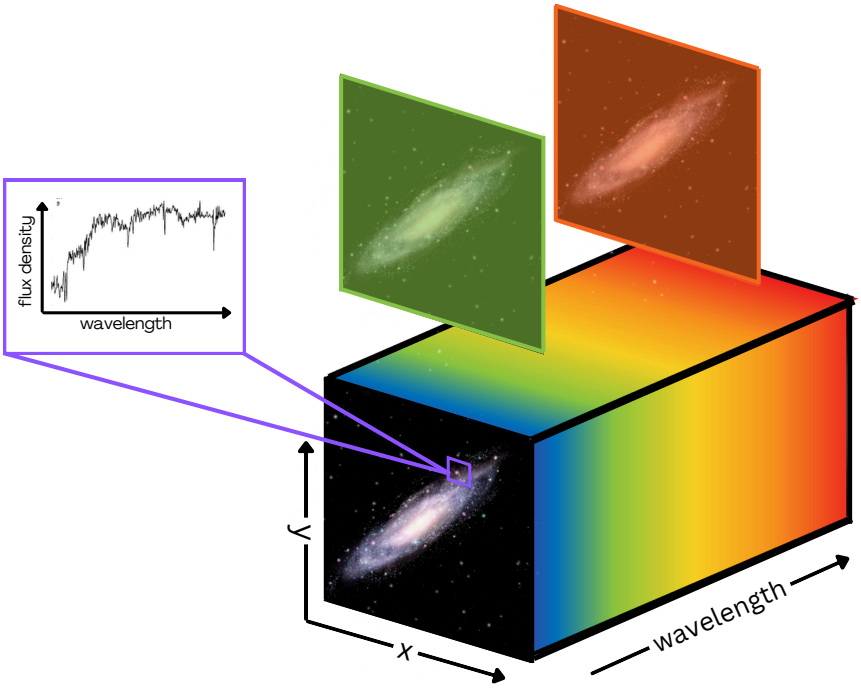

Figure 1.7
Illustration of an IFU datacube.

involves the simultaneous measurement of light from multiple points within a FOV, thereby facilitating detailed investigations of the spatial distribution of a target's inherent physical properties.

IFUs typically incorporate arrays of fibers, lenslets or mirrors arranged in hexagonal or square configurations. Each array component collects light from a circumscribed region of the sky, effectively partitioning the FOV into a grid of sub-apertures, or "spaxels". Light from each spaxel is then transmitted to a spectrograph, where it undergoes dispersion into its constituent wavelengths, thereby generating a unique spectrum for each individual spaxel. This process ultimately yields a three-dimensional data cube (as depicted in Figure 1.7), comprising two spatial dimensions covering the entire FOV, and one spectral dimension.

One of the earliest and most influential instruments in the field of IFS was the TIGER spectrograph (Bacon et al., 1995), deployed on the Canada-France-Hawaii Telescope (CFHT) and seeing first light in 1987. TIGER successfully implemented the theoretical framework outlined by Courtes (1982) to acquire three-dimensional data of an extended

object without the sensitivity degradation inherent to prior methodologies. An array of microlenses serve as a spatial sampler, channelling the collected light into a spectrograph for spectral analysis.

Present day, a burgeoning landscape of IFU projects, both ongoing and concluded, is dedicated to addressing a diverse array of scientific objectives. The SAURON project (de Zeeuw et al., 2002), a pioneering endeavour in galactic dynamics, leverages the Spectroscopic Areal Unit for Research on Optical Nebulae (SAURON; Bacon et al., 2001) IFS mounted on the William Herschel Telescope (WHT). This instrument, specifically designed for investigating the stellar kinematics, gas dynamics, and line-strength distributions of nearby ETGs, is rooted in the foundational principles established by its predecessor, the TIGER prototype IFS. The ATLAS^{3D} project (Cappellari et al., 2011) represents a comprehensive, multi-wavelength survey, encompassing observations across the radio, millimeter, and optical spectrum. The project has yielded spatially resolved stellar kinematics and dynamics for a complete sample of 260 ETGs. The IFS data for the ATLAS^{3D} project were acquired using the SAURON instrument. To complement these optical observations, the project also incorporated radio data from the Westerbork Synthesis Radio Telescope (WSRT; Józsa et al., 2009; Morganti et al., 2006; Oosterloo et al., 2010; Serra et al., 2012), millimeter observations from the IRAM 30-meter telescope (Young et al., 2011), and data from the Combined Array for Research in Millimeter-wave Astronomy (CARMA; Alatalo et al., 2011). A primary limitation inherent to surveys of this nature is the trade-off between acquiring detailed, resolved physical measurements and assembling a statistically robust sample size. As these surveys typically target galaxies individually, their efficiency in constructing large, representative datasets is inherently limited. This limitation can hinder the ability to draw meaningful statistical conclusions.

Other IFU instruments, such as the Fibre Large Array Multi Element Spectrograph (FLAMES; Pasquini et al., 2002) and the second-generation K-band Multi Object Spectrograph (KMOS; Sharples et al., 2013) mounted on The European Southern Observatory's (ESO) Very Large Telescope (VLT), offer additional capabilities. Each instrument possesses unique characteristics in terms of wavelength sensitivity, FOV, and spectral resolu-

tion, making them well-suited for observing a diverse range of objects and addressing a broad range of research objectives.

1.3.2 Adaptive Optics

One of the major impediments to ground-based astronomical observations is atmospheric turbulence. This phenomenon causes the Earth's atmosphere to act like a turbulent lens, distorting the incoming light from source objects. As a result, images become blurred and the angular resolution of telescopes is limited. The advent of adaptive optics (AO), first theorised by Babcock (1953), signifies a paradigm shift in ground-based astronomical observations. By correcting for atmospheric distortion in real-time (Rousset et al., 1990), AO systems enable the attainment of diffraction-limited imaging, thereby facilitating the achievement of resolving power exceeding the limit imposed by atmospheric seeing. This capability obviates the necessity of relocating astronomical observations to the extra-atmospheric environment, as is the case with space telescopes such as the James Webb Space Telescope (JWST). AO systems address the problem of atmospheric turbulence by employing deformable mirrors to counteract the distortions introduced by the atmosphere (e.g. Rousset et al., 1990; Herriot et al., 1998; Fusco et al., 2001). These mirrors are controlled by a wavefront sensor, which measures the atmospheric aberrations in real-time (e.g. Esposito et al., 2010). By rapidly adjusting the shape of the deformable mirror, the AO system can compensate for the atmospheric turbulence and produce images that are much sharper than those obtained without AO. See Davies & Kasper (2012) for a detailed review on AO and its applications.

1.3.3 The Advent of MUSE

One of the most impactful examples of AO for IFS, and most prevalent to this thesis, is the Multi Unit Spectroscopic Explorer (Bacon et al., 2010, MUSE;), a powerful ground-based optical-infrared IFU mounted on the VLT. With its large simultaneous spectral range (470-930 nm) and high spatial and spectral resolution ($R \sim 2000$ to $R \sim 4000$), the instrument

represents a significant leap forward in astronomical instrumentation.

MUSE comprises 24 identical modules, each incorporating an advanced slicer, spectrograph, and detector. The design was meticulously engineered to capitalise on the exquisite spatial resolution afforded by the GALACSI Adaptive Optics system (Arsenault et al., 2008; Ströbele et al., 2012). MUSE saw first light in January 2014 and offers a FOV spanning 1×1 arcmin and a spatial sampling of 0.2×0.2 arcsec in its wide field mode (WFM).

MUSE possesses a versatile range of astrophysical applications. At lower redshifts, MUSE is capable of delivering spatially resolved, high-resolution maps of the kinematic properties and stellar populations within galaxies of diverse morphological types. This capability represents a direct expansion upon the pioneering work of the SAURON project, enabling the exploration of dynamical properties within galaxies of a larger radii and at greater cosmological distances.

At higher redshifts, MUSE demonstrates its capacity to construct maps of the metallicity distribution within galaxies while simultaneously imposing constraints on their dynamical structures. By coupling these observations with environmental information derived from MUSE's wide FOV, it becomes feasible to explore the influence of the galactic environment on the properties of galaxies.

1.4 Dynamical Modelling of ETGs

Lacking spatially extended gas tracers, dynamical modelling represents the primary tool for studying the internal structure and total mass distribution of massive ETGs (Cappellari, 2016). Within gas-poor, luminous galaxies, the mass distribution is anticipated to be predominantly dominated by baryonic matter, primarily stars, in the central regions, transitioning to a DM-dominated regime in the outer region.

Within the context of disk galaxies, the relatively simple dynamics inherent to a predominantly two-dimensional, rotationally supported configuration facilitate the straightforward

determination of the mass profile from observed rotation curves. In the case of ETGs, however, the interplay between the mass profile and the observed kinematics is confounded by the orbital distribution of stars (the *mass-anisotropy degeneracy*; e.g. Binney & Mamon, 1982; Merritt, 1987; Gerhard, 1993; Treu & Koopmans, 2002b) and the situation becomes more complicated. Moreover, the available observables are restricted to projected quantities, namely the surface brightness and the line-of-sight velocities. In contrast, the dynamics of these systems are characterised by deprojected, three-dimensional densities and velocities.

Two principal methodologies employed to investigate the dynamics of ETGs are the equations of stellar hydrodynamics (the Jeans equations; Jeans, 1915, 1922) and the orbit-superposition method (Schwarzschild, 1979). These modelling techniques are predicated upon the fundamental principle that the dynamics of galaxies can be comprehensively characterised by the stellar distribution function and the gravitational potential exerted by the galaxy.

1.4.1 Jeans Modelling

The Jeans formalism offers a statistical framework for the modelling of stellar motions. The Jeans equations (Jeans, 1915, 1922), originally derived by James Clerk Maxwell, relate the second-order velocity moments to the density and potential profiles of collisionless stellar systems. They are derived from the collisionless Boltzmann equation, a fundamental equation relating the changes in the distribution function of a system to the forces acting on individual stars, which is given by

$$\frac{\partial f}{\partial t} + v\frac{\partial f}{\partial r} - \frac{\partial \Phi}{\partial r}\frac{\partial f}{\partial v} = 0, \tag{1.4.1}$$

where Φ is the gravitational potential. The collisionless Boltzmann equation can be combined with the Poisson equation for a gravitational field,

$$\nabla^2\phi = 4\pi G\rho, \tag{1.4.2}$$

to form the Jeans equations. For a given stellar density, n, as a function of position, x, and time, t, the Jeans equations are given by Binney & Tremaine (1988) as

$$\frac{\partial n}{\partial t} + \sum_i \frac{\partial (n \langle v_i \rangle)}{\partial x_i} = 0, \tag{1.4.3}$$

$$\frac{\partial (n \langle v_j \rangle)}{\partial t} + n\frac{\partial \Phi}{\partial x_j} + \sum_i \frac{\partial (n \langle v_i v_j \rangle)}{\partial x_i} = 0. \tag{1.4.4}$$

Jeans modelling involves solving these equations by assuming a density profile and velocity anisotropy to predict the velocity dispersion of a stellar system. Anisotropy, a crucial aspect of the formalism, refers to the non-uniform distribution of stellar velocities, quantified by the anisotropy parameter, β. Within the cylindrically-aligned paradigm, which is assumed in the work in this thesis, the orbital anisotropy parameter is defined as $\beta_z = 1 - \overline{v_z^2}/\overline{v_R^2}$ (Cappellari, 2008), such that $\beta_z > 0$ corresponds to flattening of the velocity dispersion ellipsoid in the vertical direction.

Assuming a constant mass-to-light (M/L) ratio , a velocity ellipsoid aligned with cylindrical coordinates (R, z, ϕ), and a system characterised by constant anisotropy quantified by $\overline{v_R^2} = b\overline{v_z^2}$, the solution to the axisymmetric radial and vertical Jeans equations is given by Cappellari (2008) such that

$$\nu\overline{v_z^2}(R, z) = \int_z^\infty \nu \frac{\partial \Phi}{\partial z} dz, \tag{1.4.5}$$

$$\nu\overline{v_\phi^2}(R, z) = b\left[R\frac{\partial (\nu\overline{v_z^2})}{\partial R} + \nu\overline{v_z^2}\right] + R\nu\frac{\partial \Phi}{\partial R}, \tag{1.4.6}$$

where Φ is a smooth potential generated by the luminosity density, ν. The separation of the 2nd moment about the symmetry axis, $\overline{v_\phi^2}$, into ordered and random motions is defined by an oblate velocity ellipsoid with a streaming velocity of

$$\overline{v_\phi}^2 = \overline{v_\phi^2} - b\sigma_z^2. \tag{1.4.7}$$

For a given observed surface brightness and assumed total mass distribution, the projection of Equations 1.4.5 and 1.4.6 onto the plane of the sky, followed by integration along the LOS, yields a singular prediction for the observed second-order moment, v^2_{LOS}, which is well-approximated by $v^2_{rms} = V^2 + \sigma^2$.

The Jeans formalism offers notable advantages through its inherent versatility and broad applicability across diverse stellar systems, facilitating the exploration of a wide range of models (e.g. Cappellari, 2008; Cappellari et al., 2013; Read & Steger, 2017). Furthermore, in comparison to computationally expensive simulations, Jeans models offer a significantly more efficient analytical approach, have predictive power, and can compute reproducible results to numerical accuracy (Cappellari, 2016). However, the deprojection of stellar surface brightness into an intrinsic luminosity density presents an inherent mathematical non-uniqueness, even under the assumption of axisymmetry, except for the specific case of edge-on galaxy orientations (Rybicki, 1987; Gerhard & Binney, 1996; van den Bosch, 1997). Furthermore, for axisymmetric systems it is typically assumed that the system is isotropic in the meridional plane, i.e. $\sigma_R = \sigma_\phi$. There is, however, no reason to believe that this should hold for real systems, and furthermore, real galaxies need not have velocity ellipsoids that are perfectly cylindrically oriented. Jeans models are also sensitively dependent on prior assumptions (e.g. Chang & Necib, 2021) and lack the robustness of orbit- or particle-based models (e.g. de Lorenzi et al., 2007; van der Marel et al., 1998). Notwithstanding these disadvantages, the Jeans method is still sufficient as a first order approximation to the dynamics of individual systems (Cappellari, 2008), such as those considered throughout this thesis.

For a detailed description of the JAM package (Cappellari, 2008) implementation of a solution to the Jeans equations, see Chapter 4.

1.4.2 Orbit Based Modelling

Orbit modelling (Schwarzschild, 1979; Richstone & Tremaine, 1984) represents a robust method for ascertaining the properties of ETGs without the necessity of a priori assumptions

regarding the nature of orbits. This approach involves constructing a galaxy model through the linear combination of a multitude of orbits that minimises the residuals between predicted and observed observables, such as energy and angular momentum.

Schwarzschild's method has been extensively employed to quantify the masses of supermassive black holes residing within galaxies (e.g. van der Marel et al., 1998; Cretton & van den Bosch, 1999; Gebhardt et al., 2003; Valluri et al., 2004), to ascertain the M/L ratio or DM profiles (e.g. Cappellari et al., 2006; Thomas et al., 2007; Weijmans et al., 2009), and to investigate the orbital anisotropy of stellar populations (e.g. Cappellari et al., 2007; van den Bosch et al., 2008). These applications underscore the versatility of Schwarzschild's method in probing the intricate dynamics of galaxies and their constituent components.

van den Bosch et al. (2008) successfully extended this methodology to encompass triaxial systems, subsequently employing it to ascertain the internal orbital distribution of NGC 4365, an E3 galaxy characterised by a kinematically decoupled core and a pronounced misalignment between its kinematic and photometric major axes. While more computationally intensive than Jeans analyses, orbit-based approaches represent the contemporary paradigm for kinematic modelling.

1.4.3 Degeneracies and Limitations

Dynamical mass modelling, while a powerful tool for studying the inherent properties of ETGs, is not without its limitations. In the absence of detailed observations from high resolution data, analyses at any significant redshift are limited to simple dynamical Jeans type models (e.g. Cappellari, 2008), as opposed to more general triaxial orbit based models (e.g. Schwarzschild, 1979; van den Bosch et al., 2008). Additionally, due to the dependence on luminous mass tracers, of which there is an absence of at large radii, and the sensitivity to many model dependant degeneracies (e.g. Bender et al., 1994; Carollo et al., 1995; Gerhard & Binney, 1996; Romanowsky & Kochanek, 1997; van den Bosch, 1997; Weijmans et al., 2009; Oldham & Auger, 2016), galaxy dynamics alone do not provide sufficient information to disentangle the stellar and dark mass contributions, and hence

place robust constraints on the physics of the DM particle.

As detailed in Section 1.2.4.2, the acquisition of direct, dynamical evidence for the presence of DM haloes enshrouding ETGs proved challenging due to the paucity of suitable and readily interpretable tracers at large radii. Moreover, the process of modelling the stellar dynamics of ETGs is considerably more complex than that of spiral galaxies, necessitating the simultaneous solution of the gravitational potential and the distribution of stellar orbits given the observed kinematics. In addition, due to the precipitous decrease in surface brightness exhibited by ETGs at larger radii, reliable dynamical measurements much beyond one effective radius are often severely hindered.

One of the most significant degeneracies in dynamical studies of ETGs is the mass-anisotropy degeneracy (Binney & Mamon, 1982; Merritt, 1987; Gerhard, 1993; Treu & Koopmans, 2002b). This degeneracy arises from the fact that the observed velocity dispersion profile of a galaxy can be influenced by both its underlying mass distribution and the anisotropy of its stellar orbits. Consequently, disentangling the effects of these two factors solely through spectroscopic data presents a challenge.

The mass-anisotropy degeneracy can be particularly problematic in studies of ETGs, as these galaxies often have complex dynamical structures and may exhibit significant anisotropy in their stellar orbits. To address this degeneracy, it is often necessary to combine spectroscopic data with constraints at different characteristic spatial scales, such as from gravitational lensing (e.g. Treu & Koopmans, 2004; Koopmans et al., 2006; Barnabè et al., 2009; Treu et al., 2010; Shajib et al., 2021), to constrain the galaxy's mass distribution and dynamical structure.

Furthermore, high spectral resolution is needed to adequately resolve targeted emission lines and absorption features needed for accurate velocity dispersion measurements, but the acquisition of high-quality spectroscopic data is inherently more resource-intensive with respect to imaging.

two high order h3 and h4, which mea- sure deviations from the simple Gaussian profile

Measuring higher-order Gauss-Hermite moments provides a more detailed picture of the

stellar dynamics of a system and can help to alleviate some of these limitations by revealing subtle dynamical features that would be missed by simpler models (e.g. Bender, 1990; Rix & White, 1992; Gerhard, 1993). The two higher-order moments h_3 and h_4 measure deviations from a standard Gaussian distribution. The third-order velocity moment, h_3, denotes the "skewness" and measures the asymmetry of the velocity distribution. The uneven distribution of velocities in different directions denotes anisotropy (Schneider et al., 2011). The fourth-order moment, h_4, measures the "peakedness" or "tailedness" of the velocity distribution and is known as the "kurtosis". An overabundance of high-velocity stars gives a characteristic leptokurtic profile to the velocity distribution, marked by extended wings and a sharpened modal peak. Conversely, a deficit of such components yields a platykurtic profile, defined by a widened central region and diminished wing amplitudes. Such parameters can indicate the presence of kinematic substructures, distinct stellar populations, or non-equilibrium dynamics. In particular, rotation accompanied by a non-zero h_3 can represent the characteristic signature of a rotating population embedded within a pressure supported system, or remnants of a merger (Balcells, 1991). However, robust measurements of the higher-order velocity moments demand high S/N spectra. Furthermore, there exists a degeneracy between σ and h_4, particularly in cases where the S/N ratio is low, or two distinct kinematic components have roughly equal luminosities (see Cappellari & Emsellem, 2004).

1.5 Strong Gravitational Lensing

In the rare cases of galaxies that gravitationally lens more distant sources, additional constraints are made available on their properties and evolution. At its simplest, strong gravitational lensing provides a robust single estimate of the mass projected within the Einstein radius (Treu, 2010). With a more sophisticated pixel-based analysis (e.g. following Dye & Warren, 2005), lensing can also probe the slope and shape of the mass density profile in the vicinity of the lensed images, at large radii where dynamical studies are not as sensitive (e.g. Ritondale et al., 2019; Shajib et al., 2021; Etherington et al., 2022).

However, lensing-only studies can be susceptible to degeneracies in the lens modelling and inherently lack sensitivity to the distribution of matter far from the lensed arcs. These degeneracies are independent of those affecting kinematic studies (Courteau et al., 2014).

1.5.1 A Brief History of Lensing

The theoretical foundation for gravitational lensing was laid by Albert Einstein in his Theory of General Relativity (GR) (Einstein, 1915). This revolutionary paradigm shift, a significant departure from Newton's classical understanding of gravity, introduced the concept of spacetime curvature induced by mass. Einstein's theory predicted that the trajectory of light would be deflected in the presence of a massive object, a phenomenon subsequently referred to as gravitational lensing. While Einstein himself did not explicitly discuss gravitational lensing in his original papers, the implications of his theory were quickly recognised by other physicists. In 1919, Sir Arthur Eddington led an expedition to observe a solar eclipse, during which the apparent positions of stars near the Sun were measured. As predicted by general relativity, the stars appeared slightly shifted due to the bending of light by the Sun's gravitational field (Dyson et al., 1920). This observation provided early evidence for Einstein's theory and marked a significant milestone in the history of gravitational lensing. Subsequent contributions, such as Zwicky (1937)'s proposition of gravitational lensing by extragalactic nebulae as a potential explanation for fluctuating distant galaxy brightness and Refsdal (1964)'s prediction of multiple quasar images, further enriched the field.

Despite the early validation, the study of gravitational lensing remained largely theoretical for several decades. Not until 1979 did the first observational confirmation of a galaxy-scale gravitational lens occur, with the discovery of the double quasar Q0957+561 by Walsh et al. (1979). Initially, the authors proposed a conventional explanation, suggesting that the two images were distinct, individual quasars with similar physical properties that happened to be in close proximity. However, they also entertained a less conventional hypothesis: that the two images were multiple manifestations of the same source. Subsequent studies from

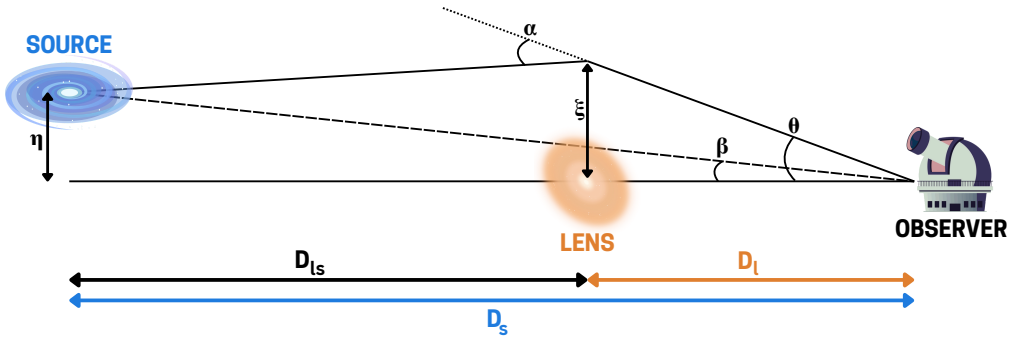

Figure 1.8
Illustration of a strong gravitational lens system.

(Gorenstein et al., 1988) and (Garrett et al., 1994), focusing on the structure of the radio jets present in the quasar's two images, validated the lensing hypothesis by demonstrating their mirror-image configuration. The discovery of this quasar, coupled with the later detection of the first quadruply imaged quasar (Weymann et al., 1980), marked a pivotal moment in the evolution of gravitational lensing research, ushering in a new era of astrophysical investigation through the study of multiply-imaged gravitational lenses.

In the decades that followed, the introduction of large-scale surveys, such as the SLACS survey (Section 1.5.4, see Bolton et al., 2006, and subsequent SLACS papers), and improved imaging techniques has led to the discovery and analysis of a growing number of lens systems. The launch of space-based telescopes like Hubble and the development of ground-based telescopes with adaptive optics have enabled us to observe fainter and more distant objects, revealing a wealth of new gravitational lensing phenomena and applications (Section 1.5.3). Lensing has been used to measure the masses of galaxies and galaxy clusters, to study the distribution of dark matter in the universe, and to detect distant galaxies and quasars that would otherwise be too faint to observe. Moreover, gravitational lensing has played a crucial role in our understanding of the nature of dark energy.

1.5.2 Gravitational Lensing Formalism

Let us consider a general lens system, such as the one illustrated in Figure 1.8, from which the lens equation can be derived. This equation serves as a mathematical correspondence between the unperturbed source position, as it would be observed in the absence of gravitational lensing, and the image position detected on the sky. The lens equation gives an unlensed angular source position described by the observed source position, θ, and the reduced deflection angle, α, such that

$$\beta = \theta - \alpha(\theta) = \theta - \frac{D_{ls}}{D_s}\hat{\alpha}(\xi). \tag{1.5.1}$$

According to the general relativistic framework describing the propagation of light, the angle of deflection of light by a point mass, M, at a distance of r from the deflector is described by

$$\hat{\alpha} = \frac{4GM}{c^2 r}. \tag{1.5.2}$$

However, in the analysis of strong lensing, where distances between the source, lens, and observer are much larger than the size of the lens, we can assume that the deflection is dominated by a single object along the line-of-sight whose size is thin as compared with cosmological distances. Under this "thin lens" approximation, we can generalise the lensing effect as

$$\hat{\alpha}(\xi) = \frac{4G}{c^2}\int d^2\xi' \int dz \rho(\xi', z)\frac{\xi - \xi'}{|\xi - \xi'|^2}, \tag{1.5.3}$$

where z is the line-of-sight coordinate and ξ' is a vector in the plane of the lens.

We now introduce the critical surface density, Σ_{cr}, which marks the threshold for the formation of multiple images, and the convergence, a dimensionless surface mass density denoted by $\kappa(\theta)$, as

$$\Sigma_{cr} = \frac{c^2 D_s}{4\pi G D_l D_{ls}}, \quad \kappa(\theta) = \frac{\Sigma(\theta)}{\Sigma_{cr}} = \frac{4\pi G D_l D_{ls} \Sigma(\theta)}{c^2 D_s}, \tag{1.5.4}$$

such that the reduced deflection angle may now be expressed as

$$\alpha(\theta) = \frac{1}{\pi} \int \kappa(\theta') \frac{\theta - \theta'}{|\theta - \theta'|^2} d^2\theta'. \tag{1.5.5}$$

In defining the lensing potential, $\psi(\theta)$, such that the scaled deflection angle is just the gradient of the potential and the convergence is half the Laplacian of the potential, we see that

$$\psi(\theta) = \frac{1}{\pi} \int \kappa(\theta') \ln \left| \theta - \theta' \right| d^2\theta' \quad \Rightarrow \quad \alpha(\theta) = \nabla\psi(\theta), \quad \kappa(\theta) = \frac{1}{2}\nabla^2\psi(\theta). \tag{1.5.6}$$

Thus, by combining Equation 1.5.4 with our understanding of circular mass distributions – specifically, the relationship between mass and enclosed convergence – we can derive the Einstein radius, θ_{Ein},

$$\theta_E^2 = \frac{4GM(\theta_E)}{c^2} \frac{D_{ls}}{D_l D_s}. \tag{1.5.7}$$

This characteristic angular scale, intrinsic to gravitational lensing, signifies the radius at which a background source will be distorted into a ring and, with the availability of high quality data, provides a direct probe of the mass distribution of the foreground deflector.

1.5.3 Applications of Strong Lensing

The applications of galaxy-scale strong gravitational lensing are multifaceted. Through the meticulous analysis of distorted images of lensed sources, it is feasible to extract key information pertaining to the properties of both the lensing galaxy and the source object.

Strong lensing offers a distinctive perspective on the mass distribution, dynamics, and evolutionary history of galaxies. Moreover, it possesses the capability to probe the

characteristics of DM haloes and the nature of their constituent DM particle, and to constrain cosmological parameters, such as the Hubble constant and the matter density parameter. Here, we focus on highlighting the application and significance of strong lensing...

1.5.3.1 ... as a cosmological probe

Gravitational lensing acts as a powerful and independent probe into the large-scale structure and evolution of the universe. Among its most notable applications is the measurement of the Hubble constant, H_0 (e.g. Vanderriest et al., 1989; Keeton & Kochanek, 1997; Kochanek, 2003; Koopmans et al., 2003; Oguri, 2007; Suyu et al., 2010, 2013; Birrer et al., 2019, etc.), a figure that, since its first measurement almost a century ago, continues to provide arguably the greatest source of contention within the cosmological community. A notable tension persists between local measurements of H_0 and inferences drawn from early-Universe probes within the context of a flat ΛCDM cosmology (see Verde et al., 2019, for a summary). Should this disparity prove to be genuine, rather than a consequence of systematic errors, it would necessitate a reassessment of the standard ΛCDM paradigm.

As first proposed by Refsdal (1964), time-delay cosmography provides robust measurements of the time delay between the arrival of light from multiple images of a single gravitationally lensed time-variable source, such as a quasar or a supernova. This temporal disparity is contingent upon the path lengths traversed by the photons and the varying gravitational potentials that they encounter. Due to the sensitivity of the ratio of angular diameter distances to H_0, this method provides a powerful approach to measuring the Hubble constant, with precision at the level of a few percent for a single strong lens system (e.g. Suyu et al., 2010; Shajib et al., 2018; Birrer & Treu, 2021). Notably, this approach operates entirely independent of other H_0 probes, providing a window into the expansion rate of the universe. As the pace of discovery and characterisation of strong lens systems accelerates, the overall precision from combining multiple systems promises to improve rapidly.

As we enter a critical time for strong gravitational lensing, the era of big data, forthcoming large-scale surveys are set to map the entire sky and are expected to deliver orders of magnitudes more lensed galaxies, quasars and supernovae. These new data have the potential to revolutionise our understanding of the large-scale structure of the Universe and offer unprecedented cosmological applications. For example, the TDCOSMO collaboration (see Gilman et al., 2020; Millon et al., 2020; Birrer & Treu, 2021; Van de Vyvere et al., 2022, etc.) will gather deep, spatially resolved James Webb Space Telescope (JWST) NIRspec IFU observations of eight galaxy-scale lens galaxies with measured time delays. These rich observations, combined with existing data, will deliver measurements of H_0 to 1.9% precision, allowing for differentiation between the values obtained by SH0ES and Planck at 4-sigma (Treu et al., 2023). However, in order to make measurements at this level of precision, it is crucial to first reduce all systematic uncertainties in the mass distribution, as the recovered value of H_0 is highly sensitive to this.

1.5.3.2 ... in understanding the properties of ETGs

Gravitational lensing has been instrumental in advancing our understanding of galaxy evolution. Given that the majority of known galaxy-scale lenses are classified as ETGs, this technique offers a unique perspective on the internal structure and fundamental properties intrinsic to such objects.

Numerous strong lensing studies have found the total density profile in ETGs to be well-approximated by a power law profile of $\rho(r) \propto r^{-\gamma}$, where the power law profile is nearly isothermal, with $\gamma \sim 2$ (e.g. Auger et al., 2009; Bolton et al., 2012; Sonnenfeld et al., 2013; Shajib et al., 2020; Etherington et al., 2022, etc.). By incorporating this robust constraint and conducting comparative analyses with cosmological hydrodynamical simulations, constraints can be imposed upon galaxy formation models and the fundamental descriptions of baryonic physics that underpin them. This was highlighted by Mukherjee et al. (2021), whose findings categorically ruled out certain feedback scenarios in ETG formation such as the absence of AGN feedback and environment-dependent stellar feedback.

To accommodate a more nuanced description of the total density profile than that afforded by the standard power law, numerous investigations have employed a two-component model to characterise the mass distribution in ETGs. This approach typically involves an NFW profile to describe the DM halo, while an additional mass profile is employed to describe the stellar mass distribution. However, the literature reveals some disagreement regarding a potential deviation of the DM halo profile from the canonical NFW form.

Dutton et al. (2007) described a halo response parameter to represent the contraction of a DM halo in response to baryonic infall, based on the adiabatic contraction model of Blumenthal et al. (1986). Numerous studies since have incorporated halo contraction as a free parameter in their analyses, with many finding inner DM profile slopes that are consistent with the standard, non-contracted NFW profile (e.g. Dye & Warren, 2005; Dutton & Treu, 2014; Shajib et al., 2021). In contrast, however, several studies have instead shown strong evidence supporting the contraction of DM haloes (e.g. Gnedin et al., 2004; Duffy et al., 2010; Grillo, 2012; Sonnenfeld et al., 2012, see also Chapter 5 of this thesis). Moreover, Oldham & Auger (2018) identified a bimodal distribution within their sample, wherein one subset exhibited a profile shallower than the NFW profile describes, while the other subset displayed a contracted profile. They attributed this bimodality to the influence of the environment on the evolution of these galaxies. Further complicating the matter, Sonnenfeld et al. (2018) reported that a M/L gradient within the stellar mass profile, rather than a deviation from the canonical NFW profile, provides the best fit to the combined dataset derived from strong lensing, dynamics, and weak lensing. It is understood that these discrepancies derive from a systematic dependence on the chosen treatment of the DM, anisotropy and light profile parameterisations, an effect that is yet to be investigated fully.

As we saw in Section 1.2.3, the precise determination of the $\mathrm{IMF}_\star$ within massive ETGs currently represents the primary systematic source of uncertainty in the measurement of their stellar masses and poses a major unresolved challenge within astrophysics. Measurements of the Einstein radius from lensing studies can provide constraints on a lens galaxy's total enclosed mass, and through the combination of stellar dynamics with lensing

constraints, robust measurements of the $\mathrm{IMF}_\star$ can be obtained (e.g. Treu et al., 2010; Auger et al., 2010a; Smith et al., 2015, etc.). Whilst most strong lensing studies find $\mathrm{IMF}_\star$ values that are heavier than that found in the Milky Way (i.e. a Salpeter IMF; Treu et al., 2010; Spiniello et al., 2011; Sonnenfeld et al., 2012), some lensing-based studies instead report a lighter $\mathrm{IMF}_\star$ (e.g. Ferreras et al., 2010; Smith et al., 2015; Sonnenfeld et al., 2019). This contention is a possible systematic effect deriving from the parameterisation choice of the DM profile, the M/L ratio and the stellar anisotropy.

1.5.3.3 ... in substructure detection

The nature of the DM particle remains an open question, with competing models leading to vastly different predictions for the distribution of halo masses as well as their populations. Cold DM scenarios posit a universe with a vast population of low-mass subhaloes. Conversely, warm DM models, characterised by free-streaming of few-keV mass particles (Benson et al., 2013), impose a lower mass limit on these subhaloes, restricting them to a range of $10^6 - 10^9\ M_\odot$, and additionally suppress the number of low-mass subhaloes (e.g. Lovell et al., 2014, 2021). Given their small size, these haloes are incapable of harboring luminous galaxies, necessitating indirect methods to probe their existence and inherent properties. The most promising method is by observing the detailed appearance of gravitationally-lensed galaxies, where perturbers (both true subhaloes and those along the line-of-sight) can cause measurable flux-ratio anomalies in lensed point-sources (e.g. Gilman et al., 2020) or distortions in extended arcs (e.g. Vegetti & Koopmans, 2009), thereby providing an excellent test of the small–scale predictions of ΛCDM.

Analysing extended lensed sources hinges on finding a foreground mass distribution which consistently reproduces the observed image pixels, given a flexible yet realistic distribution of light in the background source plane (e.g. Warren & Dye, 2003; Suyu et al., 2006). Evidence for individual substructures (e.g. Vegetti et al., 2010) arises when their inclusion improves source reconstruction and accounts for the observed pixel fluxes.

The Jackpot system, as studied in detail in Chapter 5, hosts one of only a few cases of a dark substructure detected through lensing perturbations (Vegetti et al., 2010). The substructure

is cited as having a mass high enough that one would expect it to host a luminous galaxy, as well as having a surprisingly high central density. The peculiar inferred properties of the subhalo may be a signature of a deviation from the CDM paradigm with respect to the particle physics of DM, such as dark matter self-interactions (i.e. Colín et al., 2002; Vogelsberger et al., 2012; Zavala et al., 2019; Turner et al., 2021).

1.5.4 The Sloan Lens ACS (SLACS) Survey

Before lenses can be modelled and analysed, they must first be discovered, and a variety of techniques have been explored to find lenses in a systematic way. The lens galaxies in the Sloan Lens ACS (SLACS) Survey (see Bolton et al., 2006, and subsequent SLACS papers) represent a powerful test-bed for probing the nature of massive ETGs. By leveraging the extensive spectroscopic data from the Sloan Digital Sky Survey (SDSS), an initial 85 galaxy-scale lenses were identified. The SLACS survey is optimised to detect bright early-type lens galaxies with faint lensed sources, and as such, lenses were selected from within the SDSS spectroscopic database for having multiple emission lines at a redshift significantly higher than that of the SDSS target galaxy. Follow-up high-resolution imaging with the Advanced Camera for Surveys (ACS) aboard the Hubble Space Telescope (HST) (Auger et al., 2009) allowed for the confirmation of strong gravitational lensing events. This approach has yielded a statistically significant, uniform sample of strong lenses and, as numerous studies have shown the SLACS lens galaxies to be a representative sample of the massive SDSS ETGs (e.g. Treu et al., 2006; Grillo et al., 2009; Auger et al., 2009), establishes the SLACS Survey as a cornerstone for probing the structure of elliptical galaxies. The SLACS for the Masses (S4TM; Shu et al., 2015) further expanded the sample with the addition of 40 new systems with smaller lens masses and the SDSS Quasar Lens Search (SQLS; Oguri et al., 2006) contributed an additional 28 galaxy–quasar lenses.

1.5.5 Degeneracies and Limitations

While strong gravitational lensing provides a powerful tool for studying galaxy properties and cosmology, it is not without its limitations and challenges.

For example, within the application of substructure detection using lens systems, deficiencies in the mass model, either in the macro-scale halo, or due to the presence of lower-mass dark-matter subhaloes, cause unmodelled deflections in one or more of the multiple images. The crux lies in distinguishing pixel configurations explainable by a valid source morphology from those demanding adjustments to the mass model. However, mass modelling of galaxy-scale lenses often relies on simplified single power law (SPL) or singular isothermal ellipsoid (SIE) profiles. These models belie the true complexity of real galaxies, where higher-order moments such as diskiness or boxiness (see Section 1.2.2.1), radial variations in the form of gradients and twists (Section 1.2.3), and features like merger remnants (e.g. Shajib et al., 2021) demand more nuanced approaches to capture the full richness of a galaxy's mass distribution. Indeed, in the analysis presented in Chapter 6, clear rotational signatures are identified within a significant fraction of the lens galaxy sample, which might be expected to indicate the presence of disks or other higher order structure in the mass distribution.

Arguably the most prominent degeneracy impacting lensing studies is the mass-sheet degeneracy (*MSD*; Falco et al., 1985), which is intrinsic to imaging observables in lensing and arises from the ambiguity in determining the mass distribution of a lensing galaxy from the observed lensing distortions. The MSD originates from the mathematical mass-sheet transform (MST) in the lens equation that leaves the lensing observables unchanged, other than the Hubble constant and time-delays. The mathematical form of the MST is an infinitely extending sheet of constant projected mass density (e.g. Birrer et al., 2020). There is no physically viable interpretation that results in a pure MST. This degeneracy occurs because the observed lensing distortions are primarily sensitive to the gradient of the lensing potential, rather than its absolute value. As a result, adding a distortion to the lensing potential will result in the same dimensionless observables (image positions, image

shapes and magnification ratios). The distortion can be internal to the lensing galaxy or due to intervening objects along the line of sight. Breaking the degeneracy of mass-sheet transformations on the lens plane is achievable through the use of kinematic data, whereas the line-of-sight mass-sheet contribution may be discerned via a combined analysis of line-of-sight observations and cosmological simulations (e.g. Romanowsky & Kochanek, 1999; Treu & Koopmans, 2002a; Barnabè et al., 2011, 2012).

Furthermore, strong gravitational lensing is inherently restricted in its capacity to quantify the enclosed mass across a broad range of radii, being primarily confined to the mass distribution at the Einstein radius. Consequently, to effectively break the MSD and extend the measurement of the mass profile to encompass both smaller and larger radii, it is advantageous to combine strong lensing with complementary methods, such as stellar kinematics, in analyses such as the ones described in this thesis.

1.6 Lensing + Dynamical Modelling: A Powerful Probe of Mass at a Diverse Range of Spatial Scales

The unification of mass and structure constraints from kinematic and dynamical modelling with the larger scale mass information from strong lensing allows further insight into the intrinsic properties of galaxies and the nature of DM. Access to a diverse range of spatial scales makes combined lensing and dynamical studies powerful in disentangling the stellar and the DM mass distributions of lens galaxies at their characteristic radii, and thus breaking the degeneracies between these two components (e.g. Treu & Koopmans, 2004; Koopmans et al., 2006; Barnabè et al., 2009; Auger et al., 2010a; Treu et al., 2010; Oldham & Auger, 2018; Shajib et al., 2021). For example, measurements of the Einstein radius from lensing studies can provide constraints on a lens galaxy's total enclosed mass, and by combining stellar dynamics with lensing studies, galaxy-scale strong lensing can provide robust measurements of the stellar IMF (e.g. Treu et al., 2010; Auger et al., 2010a; Smith et al., 2015).

The sensitivity of joint lensing and dynamical studies to different mass scales also gives direct insight into the apparent and surprising near-isothermality of mass in early-type galaxies (ETGs) (e.g. Koopmans et al., 2009; Auger et al., 2010b; Li et al., 2018). More pertinently, this 'bulge-halo conspiracy' describes how the total mass distribution of ETGs can be described by a power law, but the mass profile of neither the baryonic nor dark matter components can be described by a power law on their own (Treu & Koopmans, 2004; Treu et al., 2006; Humphrey & Buote, 2010; Dutton & Treu, 2014).

The foundational requirement for a joint lensing and dynamical modelling analysis entails the acquisition of an Einstein mass and a velocity dispersion profile (e.g. the SLACS analyses of Treu & Koopmans, 2004; Bolton et al., 2006; Treu et al., 2006; Bolton et al., 2008a). As such, early analyses were typically implemented by combining the lens equation with the Jeans equations, while often adopting the simplifying assumption of a constant velocity anisotropy profile. Alternatively, more sophisticated methods have been devised to construct distribution functions of lensing galaxies using the Schwarzschild method (e.g. Romanowsky & Kochanek, 1999; Barnabè & Koopmans, 2007).

While a single estimate of the mass projected within the Einstein radius and an aperture velocity dispersion constitute the minimum requirement for analyses of this nature, the process necessitates assumptions regarding the gravitational potential and orbital dynamics of the foreground deflector. The SLACS survey adopted the convention of singular isothermal ellipsoids (Bolton et al., 2008b; Auger et al., 2009, etc.), while Treu et al. (2010) assumed a constant anisotropy profile. These assumptions inevitably introduce a systematic dependence upon the chosen model parameterisations. The acquisition of spatially resolved kinematics enables a more robust determination of these parameters, thereby facilitating inferences that are significantly less contingent upon such restrictive assumptions (e.g. Barnabè et al., 2009; Spiniello et al., 2015; Etherington et al., 2023). With the contemporary availability of IFU data from instruments such as MUSE and the upcoming HARMONI spectrograph (Thatte et al., 2021, 2022), there exists a substantial opportunity to refine these methodologies.

1.7 Thesis Structure

The content of this thesis is arranged as follows. Chapter 2 details the exquisite deep IFU adaptive-optics-assisted spectroscopic data used in the individual analysis of SDSSJ0946+1006 and introduces the sample of 9 early-type SLACS lens galaxies that the same analysis techniques are subsequently generalised to. Chapter 3 outlines the standard approach to stellar template fitting, designed to ascertain the first and second order moments of a lens galaxy's two-dimensional stellar velocity distribution. This chapter also introduces a multiple-component fitting technique to account for the significant continuum contributions from the higher-redshift background source, thus enabling the robust characterisation of the lens galaxy's kinematics. In Chapter 4 is a detailed description of the JAM package (Cappellari, 2008) implementation of a solution to the Jeans equations in order to model the spatially-binned kinematic measurements from Chapter 3. Also in this chapter is a detailed description of the mass model, and its constituent components, used in the subsequent analyses. Chapter 5 presents results from a comprehensive kinematic and dynamical analysis of the Jackpot lens galaxy, yielding measurements of the total 2D-projected density profile slope of the lens galaxy. We explore parameter space for two distinct model sets with velocity dispersion ellipsoids aligned with the cylindrical (R, z) polar coordinate system; a set of models with the DM density slope as a free parameter, and a further set of models with the DM density fixed as a NFW profile. These kinematic and dynamical modelling techniques are then generalised and applied to a broader sample of 9 further lens galaxies in Chapter 6. Ensemble measurements of the lens parameters are presented, and an additional set of models are explored wherein the imposed lensing mass is permitted to vary, scaled by a free parameter, ζ. We discuss our findings in Chapter 7 and place them in the context of previous studies of the SLACS lenses within the literature. We also consider the robustness of our assumptions and the fundamental limitations of our modelling approach. Results are summarised in Chapter 8.

CHAPTER 2

Data

To write it, it took three months; to conceive it - three minutes; to collect the data in it - all my life

~ F. Scott Fitzgerald

The data analysed in this work consists of deep, high-resolution, adaptive-optics-assisted MUSE spectroscopic data and photometric *Hubble* Space Telescope (HST) observations of a subset of 10 SLACS lens galaxies. The physical properties of each target are presented in Table 2.2, and each of the individual observations are summarised in Tables 2.1 and 2.3, and detailed in the sections below. All MUSE spectroscopic data presented in this chapter were obtained in Narrow Field Mode (NFM) with a field-of-view of 7.5×7.5 arcsec.

Table 2.1
Details of the MUSE observations of the lens sample. The J0946+1006 'Jackpot' lens serves as a representative example and is explored in detail to describe the methods employed throughout this thesis in Chapters 3 and 4.

Lens Name	Prog. ID	Exp. Time (s)	Target S/N
J0216-0813	0106.A-0872(A)	7852	40
J0912+0029	0102.B-0907(A)	5188	50
J0935-0003	0106.A-0872(A)	7852	30
J0946+1006	0102.A-0950(A)	18804	50
J1020+1122	0106.A-0872(A)	7852	50
J1029+0420	0102.B-0907(A)	2682	50
J1112+0826	0106.A-0872(A)	7852	30
J1143-0144	0102.B-0907(A)	2682	50
J1250-0135	0102.B-0907(A)	2682	50
J1451-0239	0102.B-0907(A)	8046	50

2.1 The MUSE Data

2.1.1 Exquisite Deep IFU Adaptive-Optics-Assisted Spectroscopic Data for SDSSJ0946+1006

In Chapter 5, we present a detailed kinematic and dynamical modelling study of the Jackpot (SDSSJ0946+1006) lens galaxy. Deep integral field unit (IFU) adaptive-optics-assisted spectroscopic data (project ID 0102.A-0950; as described in Collett & Smith, 2020; Smith & Collett, 2021) were obtained from a 5.2 hour total integration time with the MUSE instrument on the VLT, operating in Wide Field Mode (WFM). When compared to previous single-slit observations, this data provides full azimuthal area coverage, high sensitivity and a high angular resolution (0.5 arcsec FWHM). As a result, we can measure the two-dimensional stellar kinematic properties out to ~ 10 kpc (~ 2.7 arcsec) from the centre of the lens, as well as resolving the inner profile inwards to $\sim$1 kpc. Measuring the kinematics out to larger radii with greater precision than previous studies helps to break the degeneracies between the stellar and DM mass components by probing the radii where DM contributions become more significant. Thus, allowing us to span the relevant range

for projected mass slope measurements at the Einstein radius that allow us to place our results into the context of previous pure lensing studies.

Figure 2.1 shows a collapsed MUSE image of the lens and its environment. Denoted are the extent of the stellar kinematic measurements and the locations of the foreground lens galaxy and the first Einstein ring. Some of the structure visible at low surface brightness is caused by MUSE sensitivity variations, but the overall asymmetry, with an extended plume to the north, is reproduced in other imaging, e.g. Figure 3 of Sonnenfeld et al. (2012).

The physical scale resolution of our observations (1.86 kpc for a 0.5 arcsec FWHM at $z = 0.222$) is an order of magnitude coarser than that of the typical dynamical analyses of nearby ETGs. For example, the ATLAS^{3D} survey (Cappellari et al., 2011) which, with an angular FWHM of 1.5 arcsec and galaxy redshift of $z \lesssim 0.01$, has a physical spatial resolution typically ∼0.15 kpc. However, the modelling techniques that we use here are also routinely applied to galaxies with comparable physical resolutions to our data. For example, the MaNGA Survey galaxies (Bundy et al., 2015), which have a poorer median spatial resolution of 2.54 arcsec FWHM for a median redshift of $z = 0.037$, leading to a physical FWHM of 1.8 kpc (Law et al., 2016).

2.1.2 A Sample of SLACS Early-Type Lens Galaxies

Chapter 6 is a direct extension of the work described in Chapter 5 and generalises the methods described therein. The analysis presented in Chapter 6 focuses on the kinematic and dynamical modelling of a sample of 9 early-type lens galaxies discovered via the SLACS survey and previously studied in several papers (e.g. Bolton et al., 2008a; Grillo et al., 2009; Auger et al., 2009). The physical properties of each target are presented in Table 2.2, and the stellar mass, redshift and Einstein radius of our sample are shown in relation to that of the SLACS parent sample in Figure 2.2. The gravitational lens systems within our sample span a lens and source redshift range of $0.087 \leq z_{\rm lens} \leq 0.347$ and $0.324 \leq z_{\rm source} \leq 0.630$ respectively, have Einstein radii within the range $0.87 \leq R_{\rm Ein} \leq 1.68$ arcsec, or $1.92 \leq R_{\rm Ein} \leq 6.19$ kpc, and effective radii in the range

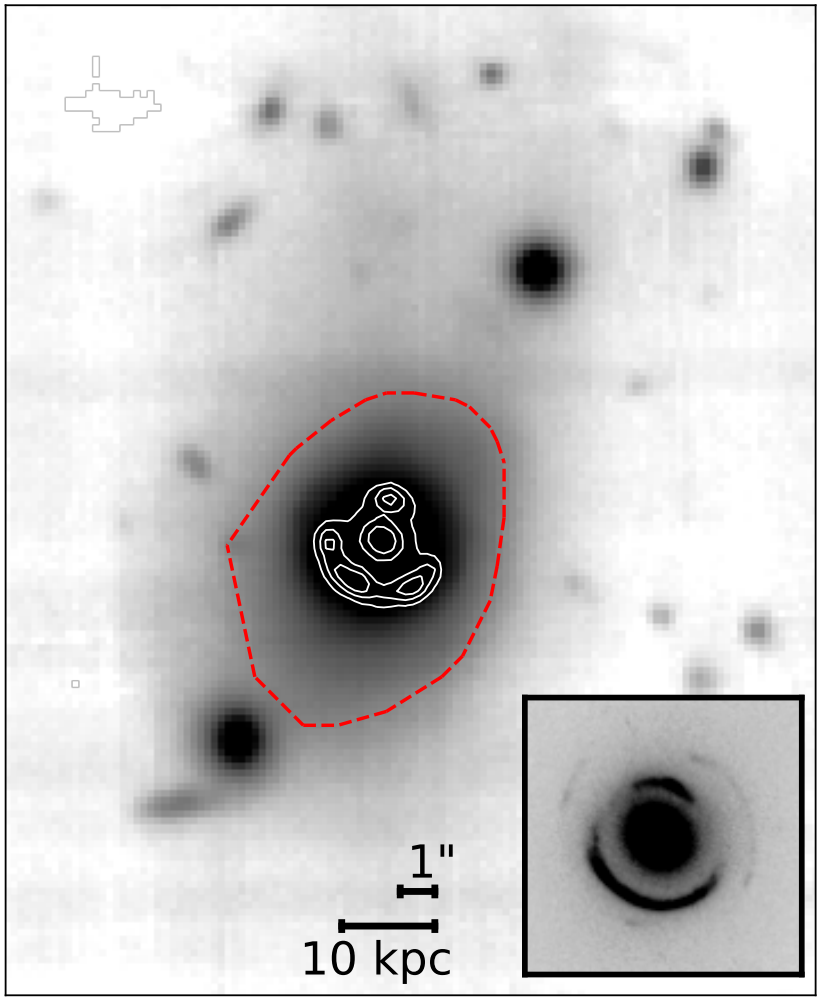

Figure 2.1
Collapsed MUSE image of the Jackpot triple-source lens system and its environment. The red dashed line denotes the extent of the stellar kinematic measurements, and the white contours highlight the location of the foreground lens galaxy and the first Einstein ring. Inset is the SLACS F814W *Hubble Space Telescope* (HST) image of the Jackpot lens and the first and second Einstein rings (2096 sec exposure; Programme 10886; PI: Bolton).

Table 2.2

Properties of the early-type lens galaxies comprising our sample. Redshifts $z_{\rm lens}$ and $z_{\rm source}$ are measured from SDSS data and reported in Auger et al. (2009), as are lens galaxy velocity dispersions, $\sigma_{\rm SDSS}$, and stellar mass estimates assuming a Chabrier IMF, $M_*^{\rm Chab}$. Effective radii, $R_{\rm eff}$, are quoted at the intermediate axis, and with Einstein radii, $R_{\rm Ein}$, are taken from Bolton et al. (2008a). Note that in the absence of an Einstein radius for J1250 in the literature (see main text for details), the value given in this table derives from a simple lens modelling analysis under the assumption that the complex spiral structure is at the redshift of the source. This determination made use of a code provided by a collaborator. The J0946+1006 'Jackpot' lens serves as a representative case study in Chapters 3 and 4.

Lens Name	$z_{\rm lens}$	$z_{\rm source}$	$R_{\rm eff}$ (")	$R_{\rm Ein}$ (")	$\sigma_{\rm SDSS}$ (km s^{-1})	$\log[M_*^{\rm Chab}/M_\odot]$
J0216-0813	0.332	0.524	2.67	1.16	333 ± 23	11.79 ± 0.07
J0912+0029	0.164	0.324	3.87	1.63	326 ± 12	11.71 ± 0.07
J0935-0003	0.347	0.467	4.24	0.87	396 ± 35	11.72 ± 0.07
J0946+1006	0.222	0.609	2.35	1.40	263 ± 21	11.34 ± 0.12
J1020+1122	0.282	0.553	1.59	1.20	282 ± 18	11.54 ± 0.12
J1029+0420	0.104	0.615	1.56	1.01	210 ± 9	11.04 ± 0.12
J1112+0826	0.273	0.630	1.50	1.49	320 ± 20	11.48 ± 0.09
J1143-0144	0.106	0.402	4.80	1.68	269 ± 5	11.36 ± 0.09
J1250-0135	0.087	0.353	2.93	1.10	246 ± 9	11.13 ± 0.06
J1451-0239	0.125	0.520	2.48	1.04	223 ± 14	11.17 ± 0.07

$1.5 \leq R_{\rm Ein} \leq 4.8$ arcsec.

Our sample selection was driven by the availability of deep, high-resolution, AO-assisted Multi Unit Spectroscopic Explorer (MUSE) spectroscopic archival data. As demonstrated in Chapter 5, in order to fully exploit the additional advantages that kinematic data can bring to breaking degeneracies, it is critical that IFU data with good spatial and angular resolution are obtained. Given the typical angular distances between lens and source, and the typical coverage of single-slit observations, the improved radial extent and resolution afforded by MUSE IFU data allows analyses to extend beyond the Einstein radius and probe out into the crucial radial ranges at which DM contributions become more significant. Additionally, robust mass modelling techniques often suffer from intrinsic degeneracies that, in order to overcome, demand much more stringent requirements on the data, with a necessity for a very high signal-to-noise (S/N) ratio that is only achievable with MUSE-like

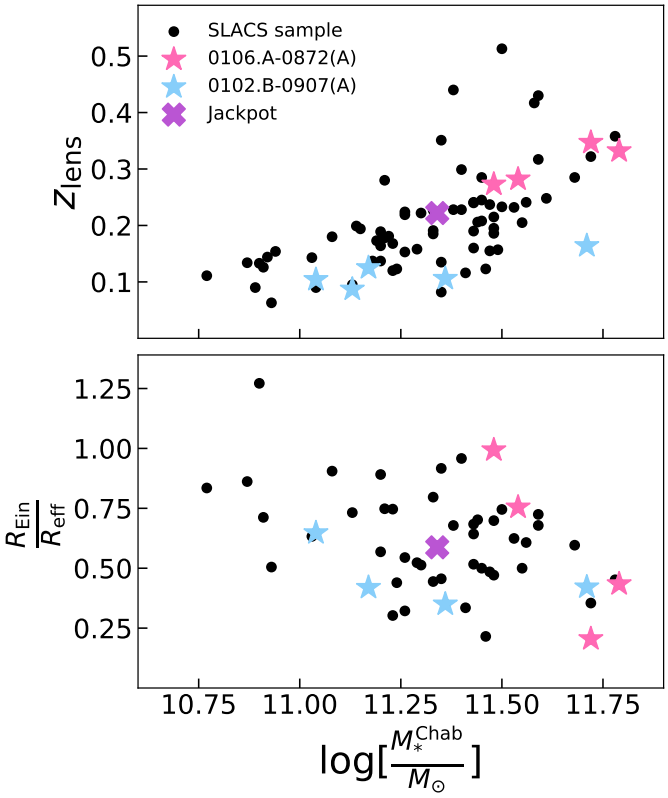

Figure 2.2

The physical properties of our sample of lenses in relation to that of the parent SLACS sample. The pink and blue stars correspond to lenses whose MUSE spectroscopic data derive from ESO programmes 0106.A-0872(A) (PI: Smith) and 0102.B-0907(A) (PI: Collett), respectively. The purple cross denotes the SDSSJ0946+1006 'Jackpot' lens that serves as a representative example in Chapters 3 and4. The properties of our sample span a reasonable range in terms of the stellar mass estimate (assuming a Chabrier IMF), redshift and Einstein and effective radii.

instruments.

Exemplifying the power of MUSE IFU data in disentangling the lens and source light contributions, we demonstrate in Chapter 6 how, with a total exposure time of only ~ 0.75 hours, it is possible to achieve robust first- and second-order two-dimensional stellar kinematic measurements of SDSSJ1250-0135. This complex lens system has previously been excluded from sample studies of lens galaxies due to the presence of spiral arms, which severely hinder any accurate lensing analysis due to the necessity to disentangle the intricate light contributions from these arms and the superimposed Einstein ring (e.g. Bolton et al., 2008b; Auger et al., 2009). The additional wealth of information afforded by MUSE IFU data conclusively demonstrates that the complex structured light is at the redshift of the background source, allowing the 2D stellar kinematics of the foreground elliptical lens galaxy to be measured for the first time.

Our deep MUSE spectroscopic data are taken from two pre-existing observing programmes, each driven by distinct scientific motivations and selection criteria. Observations taken from ESO programme 0106.A-0872(A) (PI: Smith) targeted known lens galaxies with a large lensing cross-section. These galaxies were further selected for their cosmographically optimal redshifts and bright background sources. This strategic selection enables the detection of additional faint emission-line sources residing behind the targeted lens galaxies, effectively converting them into powerful Double Source Plane Lens (DSPL) configurations. Conversely, ESO programme 0102.B-0907(A) (PI: Collett) was driven by a critical need to expand the diversity of the sample available for the characterisation of the stellar initial mass function (IMF) and dark halo structure of early-type galaxies (ETGs). For this reason, the programme selected strong lens targets – individual field ETGs – with redshifts of $z \sim 0.1$.

Given the archival nature of our data, the range of physical properties, such as redshift and mass, of our lens sample is constrained by the selection criteria of the original observing programmes. Despite this limitation, Figure 2.2 illustrates that the sample still encompasses a sufficiently broad range to facilitate a statistically robust investigation. Moreover, to extract meaningful insights into the modelling techniques commonly applied

to such objects, a homogeneous dataset, rather than a collection of data from different instruments, is advantageous.

2.1.3 Treatment of the MUSE Data

To prepare the spectroscopic data for subsequent spectral fitting (as detailed in Chapter 3), we first perform a sky-subtraction to remove any prominent skylines from the spectra. We do this using a composite spectrum taken from an annulus around the target. We then implement the two-dimensional adaptive spatial binning algorithm, VorBin Cappellari & Copin (2003).

The implementation of spatial binning methods is necessary to achieve a high enough signal-to-noise (S/N) ratio for precise kinematic measurements. This technique leverages a Voronoi tessellations approach to identify spatially proximate pixels and subsequently group them into bins. This approach ensures an approximately uniform S/N ratio across the resulting bins, providing a statistically robust foundation for spectral fitting. The number of resulting bins for each lens galaxy, alongside the distance that each lens was measured out to, was chosen to optimise both the spatial resolution and the S/N ratio of the combined bin spectra, ensuring sufficient S/N for robust analysis while maintaining the ability to discern subtle spatial variations within the lens galaxy. The chosen target S/N ration for each lens is shown in Table 2.1.

2.2 The HST Data

With the exception of J1250, complimentary HST Advanced Camera for Surveys (ACS) archival data were obtained from the HST programmes 10494 (PI: Koopmans), 10886 (PI: Bolton), 10174 (PI: Koopmans), 10587 (PI: Bolton) and 10798 (PI: Koopmans). To optimise the total exposure time whilst minimising contributions from the source emission that are stronger in the bluer bands, exposures were captured through the F814W filter using the Wide Field Camera's (WFC) designated WFC1 aperture. Due to prominent

Table 2.3
Details of the HST observations of the lens sample

Lens Name	Prog. ID	Exp. Time (s)
J0216-0813	10494	2232
J0912+0029	10494	2224
J0935-0003	10174	420
J0946+1006	10886	2096
J1020+1122	10886	2096
J1029+0420	10886	2088
J1112+0826	10587	420
J1143-0144	10798	2112
J1250-0135	10798	2560
J1451-0239	10798	2112

features in the ACS image of J1250 from the bright source structure, a Near Infrared Camera and Multi-Object Spectrometer (NICMOS) image from HST programme 10798 (PI: Koopmans) in the F160W-band was used instead. HST images of the SLACS lenses presented in Chapter 6 are shown in Figure 2.3.

The limited availability of a single HST image in the F814 band for both J0935 and J1112 resulted in sub-optimal cosmic ray rejection, which is evident in the overall image quality for these targets. Furthermore, observations of J0216 and J0935 were complicated by the presence of very bright neighboring sources and the observation of J1451 revealed a low-brightness horizontal structure in close proximity to the lens and the bright source counter-images. Pixels with significant contribution from either the source light or neighbouring bright satellites, i.e. where residuals from an initial MGE fit to the HST image (see Chapter 5) are $\gtrsim 5\%$, were masked out to mitigate the potential impact on the dynamical modelling analysis.

In the case of the Jackpot lens, the prominent Einstein arc significantly hinders the accurate determination of the lens luminosity profile, an important component of our mass modelling technique as described in Chapter 4. Consequently, we instead use an image from which the arc has been subtracted using a lens reconstruction model, as is described in Section 4 of Etherington et al. (2022). Specifically, we use an image from HST (F814W-band), with

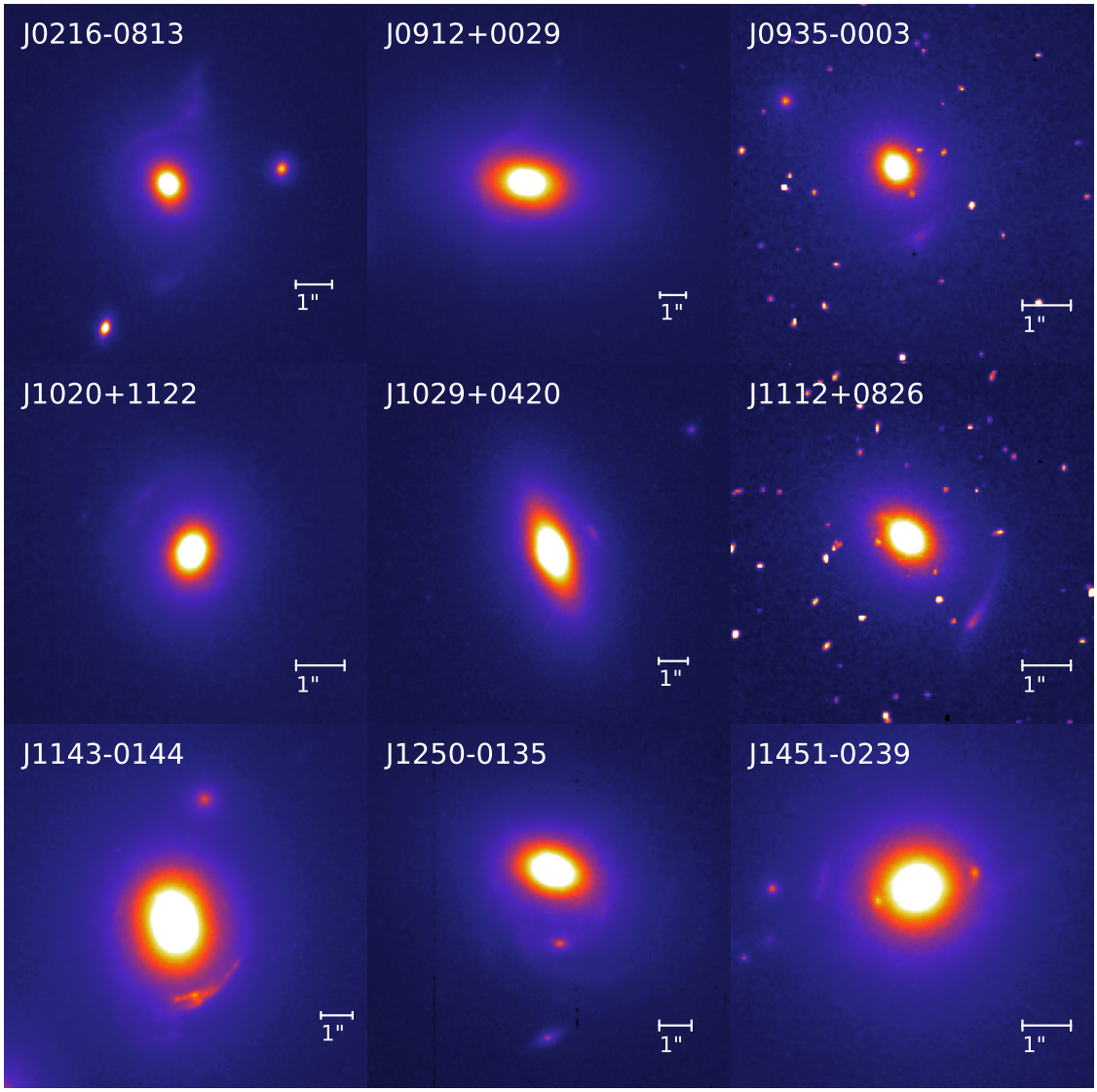

Figure 2.3
The F814W-band HST/ACS images of 8 of the SLACS lens galaxies studied in Chapter 6, and the F160W-band HST/NICMOS image of J1250 (see body text for details).

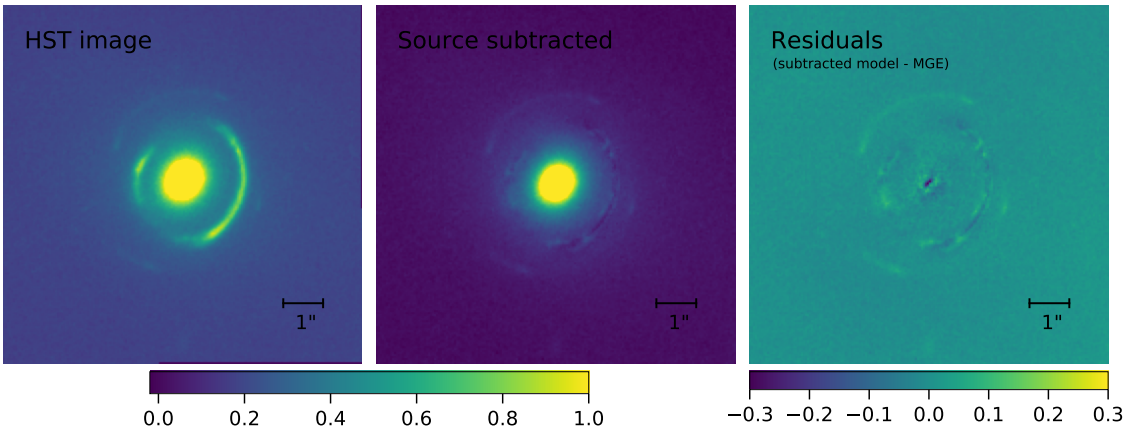

Figure 2.4
The F814W-band HST/ACS image of the Jackpot lens, the HST image with the parameterised source model subtracted and the residuals from the MGE model subtraction. Each panel corresponds to a field of view of 9 arcsec on a side.

a rest-frame wavelength of ~6700 Å, from which a PyAutoLens-fitted (Nightingale et al., 2018, 2021) parameterised source model has been subtracted. The parameterised model assumes the source galaxy to be well-described intrinsically by a smooth Sérsic-profile galaxy. Although this method yields a less precise source-subtraction than the alternative pixelised-source approach, it is preferred here to avoid over-fitting of the lens galaxy light. Figure 2.4 shows the F814W-band HST image, the HST image with the smooth Sérsic-profile source model subtracted, and the residuals obtained from subtracting the MGE luminosity profile from the source-subtracted model. We note that whilst the source-subtracted model fails to reproduce all of the observed features in the arcs that reflect real structures in the source, this treatment is sufficient to allow the natural robustness of MgeFit (as described in Chapter 4) to follow the true luminosity distribution of the lens galaxy.

CHAPTER 3

Stellar Kinematic Template Fitting

The fault, dear Brutus, is not in our stars, but in ourselves

~ William Shakespeare

Constraining the dynamical nature of the foreground lens galaxy necessitates the acquisition of robust, spatially resolved measurements of the stellar kinematics. To achieve this, stellar template fitting is employed, extracting the first and second order moments of the lens galaxy's two-dimensional stellar velocity distribution.

To account for the strong continuum contributions from the higher-redshift background source, a multiple-component fitting technique must be adopted to simultaneously model the stellar lens and source components, thus enabling the robust characterisation of the lens galaxy's kinematics. This adaptation to the common approach is necessary as, whilst the source emission lines could be simply masked out, the bright source continuum can not sufficiently be masked without a significant loss of spectra.

The analyses described in Chapters 5 and 6 share a common multiple-component fitting technique, with the work of the latter chapter representing a direct extension and generalisation of the former. As such, in this chapter, we will focus on the stellar template fitting of the Jackpot lens as a representative example.

3.1 The Standard Application of PPXF

A common approach to kinematic template fitting within foreground lensing studies involves using the stellar template fitting software PPXF (Cappellari & Emsellem, 2004; Cappellari, 2017), which implements penalised pixel-fitting to extract the moments of the line of sight velocity distribution from galaxy spectra. This technique operates by fitting a linear combination of template spectra to the observed galaxy spectrum from each spatial bin. In the context of the work described in this thesis, the templates comprise of an ensemble of simple stellar populations (SSPs) spanning a range of metallicities and ages. PPXF employs a robust statistical framework for extracting information about the galaxy's stellar population and kinematics. It utilises a penalised chi-squared minimization technique, which balances the goodness of fit with the smoothness of the solution, preventing overfitting. The fitting process assumes Gaussian errors on the input spectrum, and the quality of the fit is assessed using the reduced chi-squared value.

With this approach, we consider a restframe wavelength range of 4699 Å to 7408 Å and apply the penalised pixel-fitting method to each bin individually. The template library is taken from the E-MILES stellar population models (Vazdekis et al., 2016), chosen for their broad spectral range (1680 to 50000 Å), good resolution (FWHM = 2.5 Å from 3540 Å to 8950 Å) and age/metallicity coverage ($-1.79 < [M/H] < +0.26$ and ages above 30 Myr). Unlike other SSP models that do not extend far enough in to the blue end of the spectrum for us to recover the relatively distant $z = 0.609$ source, this broad spectral range allows us to fit to the younger spectral features of the source galaxy, as well as the older features of the lens elliptical galaxy. This basic approach works well on the very central regions of the system where there exists little contamination from the source light.

In order to place robust constraints on the mass model, it is desirable to map the kinematic measurements in a range of radii that span the Einstein radius, given our mass constraint at this distance and the high area coverage made available by our MUSE data. However, there are a number of bins in these outer regions where strong continuum contributions from both the source and lens galaxies are present. This demands more complexity in

our template fitting than the standard PPXF treatment provides and makes it necessary to fit to both lens and source simultaneously, as whilst the source emission lines can be simply masked out, the bright source continuum can not sufficiently be masked without a significant loss of spectra.

This is demonstrated in the first panel of Figure 3.1, which shows strong source emission lines and prominent Balmer absorption lines in our observed data that are not being fit by the total fit template. Whilst these lines are mostly present in the spectra of the bluer source galaxy, not accounting for them will affect our ability to recover the kinematics of the lens galaxy as PPXF otherwise compromises by using templates from an older but higher-velocity dispersion population to account for the source. This motivates the necessity for a multiple-component fitting approach, whereby this problem is alleviated through the addition of both a second set of stellar templates to model the source galaxy, and a set of gas emission templates. The improvement of the total fit to the observed spectra obtained through the inclusion of these additional components can be seen in the second and third panel of Figure 3.1 respectively, and is described in the following section.

3.2 Multiple Component Fitting

Figure 3.2 shows examples of both a central bin almost entirely dominated by lens light and a highly contaminated bin at the Einstein radius. To each bin spectrum, we mask out prominent subtraction residuals from the brightest sky lines and fit stellar kinematic components corresponding to the lens and the source galaxies and also a small number of gas components. To do this we define a total of four components to be fit:

- a combination of SSP templates at redshift $z \approx 0.222$ to represent the lens;
- a combination of SSP templates at redshift $z \approx 0.609$ to represent the bright source;
- a gas template at the source redshift, corresponding to the Balmer series emission lines from Hβ to Hη and with fixed Case-B recombination flux ratios;

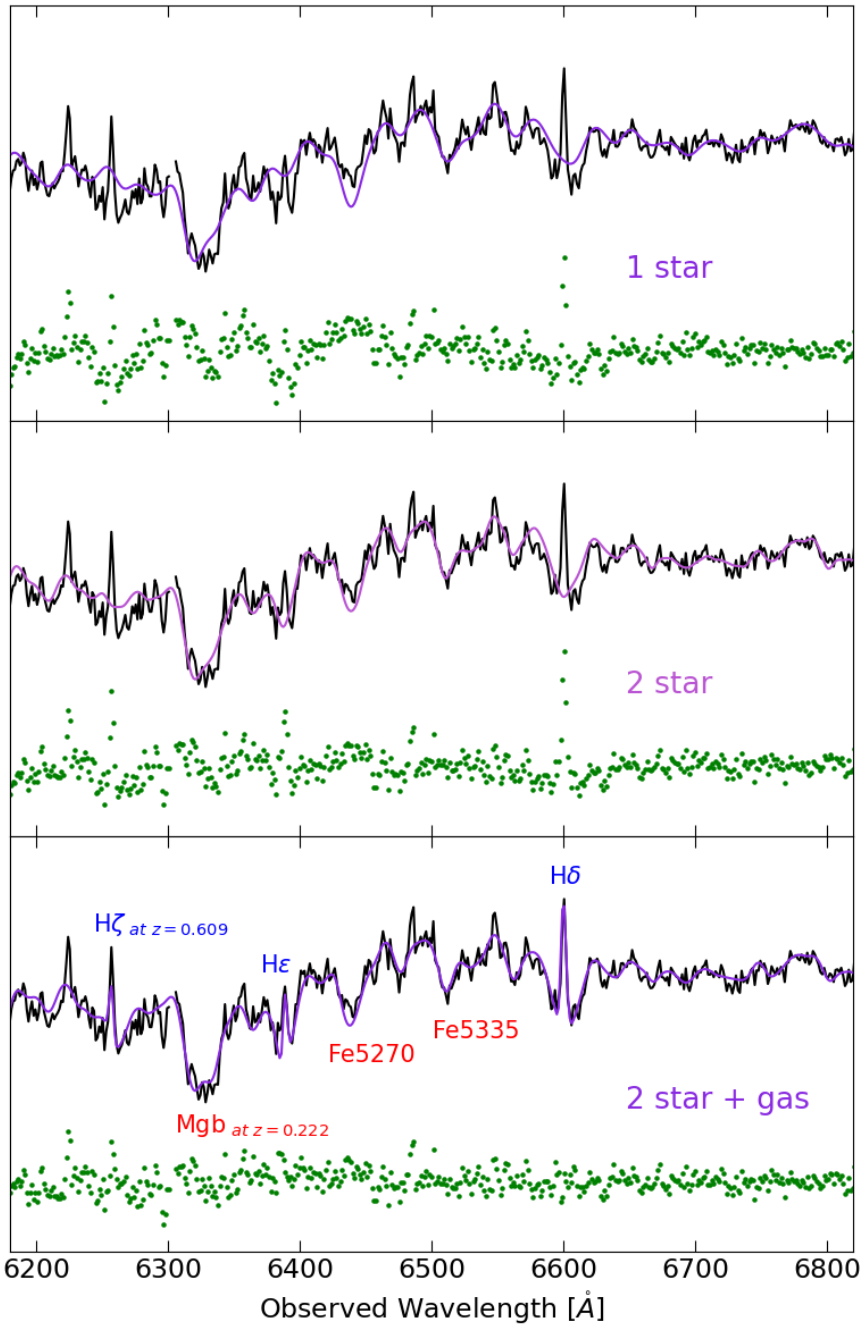

Figure 3.1

A zoomed-in view of the total fit to the galaxy spectrum for the 1 star, 2 star and 2 star + gas template fitting methods. The 1 star fit highlights how the standard usage of PPXF gives a poor fit to the composite spectra, i.e. pixels contaminated by light from the Einstein ring. We can see strong emission lines in the observed data that are not being matched by the total fit template derived from the 2 star fitting method. The 2 star + gas panel demonstrates the significantly improved fit of the total model to the observed spectrum. Also indicated are the absorption features at the lens redshift, and the emission peaks at the source redshift.

- a further gas template at redshift z = 0.609 for the [O II] doublet*.

Despite the main focus of this fitting being the extraction of the lens kinematics, each component has its own velocity and velocity dispersion in order to recover the lens component without bias^.

A combination of the best fitting SSP templates is determined and averaged to make a template model for each of the components and the fractional contribution of each model to the observed spectrum is optimised in order to construct the total fit. The top panel of Figure 3.2 shows that for bins dominated by lens light, the total fit is almost entirely constructed from SSP templates at redshift $z = 0.222$. In contrast to this, bins such as the one shown in the bottom panel are composed of a relative contribution of the lens, source and gas templates.

The addition of the two gas components to account for the Balmer emission lines and the oxygen doublet allows us to obtain a further improvement to the fit with significantly reduced residuals. This can be seen in the second and third panels of Figure 3.1 when compared with the first panel. The emission features that are not well fit by the 1 star model, such as the deep absorption wings on either side of the H-δ emission line (at ~6600 Å in the observed frame), are now present in the total fit of the 2 star + gas model.

*We note here that the velocity of [O II] is not explicitly tied to that of the Balmer lines or the stars.

^Recall that the data were binned according to the continuum S/N ratio to optimise the recovery of the lens stellar kinematics, and therefore the binning is poorly configured for spatially resolving the source kinematics.

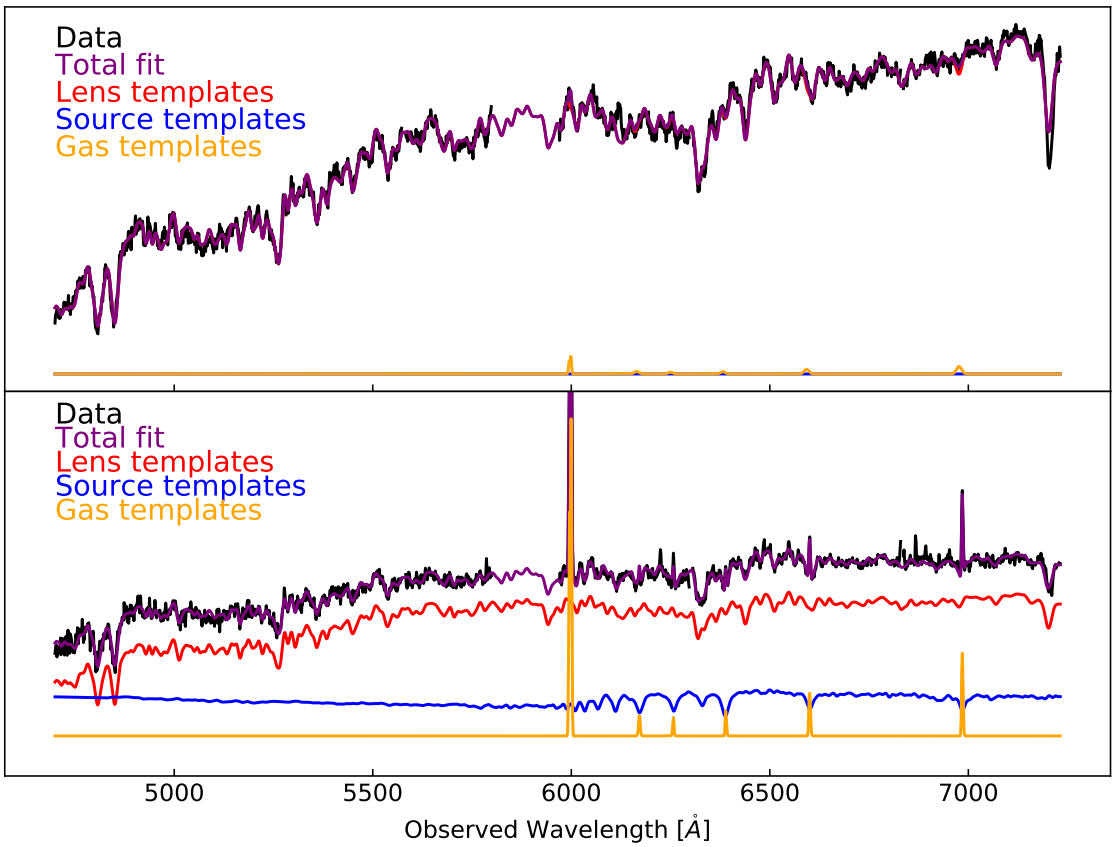

Figure 3.2

A demonstration of the multiple components used in the total fit to the galaxy spectrum, as demonstrated for both a central bin almost entirely dominated by lens light (top panel) and a bin near the Einstein radius that is highly contaminated from the lensed source (bottom panel). The stellar kinematic components correspond to the lens galaxy at $z = 0.222$ and the source galaxy at $z = 0.609$. Also present are the two gas components accounting for the [O_{II}] doublet and Balmer emission lines.

CHAPTER 4

Dynamical Mass Modelling with JAM

Remember that all models are wrong; the practical question is how wrong do they have to be to not be useful

~ George E. P. Box

We model the spatially-binned kinematic measurements from Chapter 3 using the anisotropic Jeans model approach, as implemented in JAM (Cappellari, 2008, 2012). We impose a robustly constrained aperture lensing mass to reduce the freedom in the models. By optimising the model parameters as described in this chapter, we maximise the likelihood of the observed root-mean-square velocities, $v_{\rm rms}$, obtained from the observed velocities and velocity dispersions and given as $v_{\rm rms} = \sqrt{v^2 + \sigma^2}$.

As with the kinematic template fitting detailed in Chapter 3, the analyses presented in this thesis employ a shared dynamical mass modelling technique. As such, to illustrate this technique, the Jackpot lens serves as a representative case study in this chapter.

4.1 Mass Model

Our dynamical mass models posit a total lens galaxy mass distribution composed of three primary constituents: the stellar mass deprojected from the observed light (assuming a constant $M/L_\star$ ratio), a spherical DM halo, and a centrally concentrated excess mass component. A more detailed description of these components follows. To ensure consistency with the observed lensing configurations, each model component is parameterised by its fractional contribution to the total lensing mass within the Einstein radius.

4.1.1 Stellar Mass

The treatment of the photometric data follows the common approach of deprojecting the luminosity density using the MgeFit software (Emsellem et al., 1994; Cappellari, 2002). This approach employs a multi-Gaussian expansion (MGE) to model the surface brightness distribution derived from high-resolution HST imaging data.

This image, with a rest-frame wavelength of ~6700 Å (and an average rest-frame wavelength of ~6700 Å for the lens sample presented in Chapter 6), is not expected to be sensitive to any modest variations in age and metalicity, and therefore the luminosity in this band is assumed to trace the stellar mass surface density reasonably well (in shape, but not normalisation) in the absence of any IMF gradients. The MGE projected surface brightness of the foreground deflector within the MGE framework is given as

$$\Sigma(R', \theta') = \sum_{j=1}^{N} \frac{L_j}{2\pi\sigma_j^2 q'_j} \exp\left[-\frac{1}{2\sigma_j^2}\left(x_j'^2 + \frac{y_j'^2}{q_j'^2}\right)\right], \tag{4.1.1}$$

where (R', θ') are the polar coordinates on the plane of the sky (x', y'). N is the number of Gaussian components with total luminosity given by L_j, observed axial ratio of $0 \leq q'_j \leq 1$ and width along the major axis of σ_j, as per Cappellari (2002).

Implementing the capabilities of the MgeFit code, the luminosity profile of the lens galaxy is measured. This is achieved by segmenting the HST image (or the source-subtracted

Table 4.1

MGE$_\star$ for the Jackpot galaxy. The columns represent, left to right, the projected surface mass density multiplied by the best fitting stellar fraction parameter in the free γ JAM models (see Chapter 5), the MGE width, and axis ratio.

$\Sigma_\star \times f_\star$ [$M_\odot/pc^2$]	σ [arcsec]	q
7609.12	0.075	0.984
6370.03	0.197	0.896
2715.53	0.442	0.821
751.32	0.890	1.000
268.85	2.366	1.000

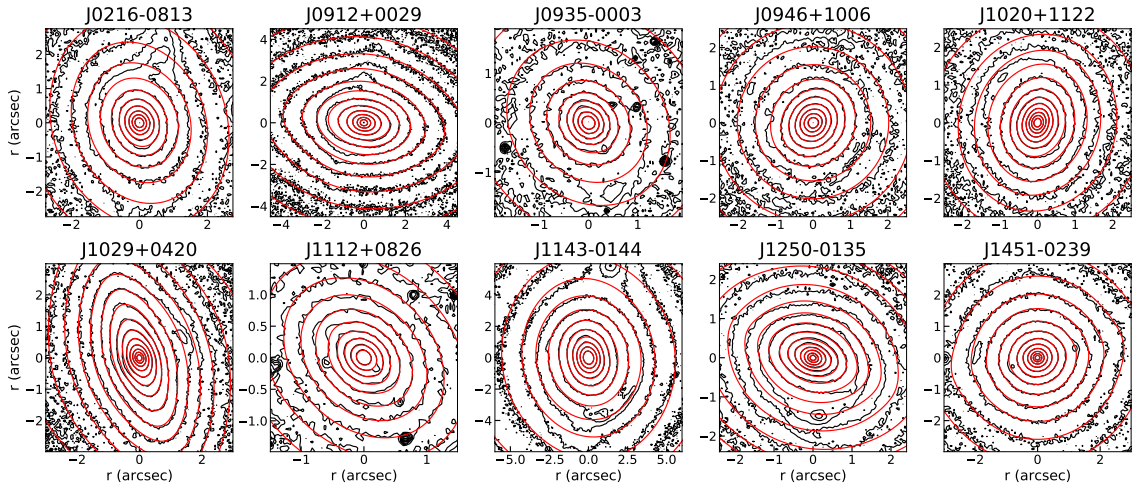

Figure 4.1

Isophote plots of the galaxy HST images (black). The contours of the MGE model surface brightness are overlaid in red. The fourth panel in this figure, labelled J0946+1006, corresponds to the Jackpot lens used as a representative case study in this chapter. Figure 4.2 provides a zoom-in of this plot.

image in the case of the Jackpot) into a series of elliptically-defined sectors. Subsequently, MGEFIT fits a series of Gaussians to the profile, describing the intensity and shape of the total surface brightness.

The point spread function (PSF) of each of the HST images was approximated with a single Gaussian of 0.1 arcsec FWHM; however, little difference was found in the recovered parameters when this value was varied within reasonable limits. The projected mass density in stars is then assumed to be proportional to the projected luminosity density, i.e. with a constant M/L$_\star$ ratio. Table 4.1 presents the stellar mass density MGE model for the best fitting model parameterisation of the Jackpot lens galaxy.

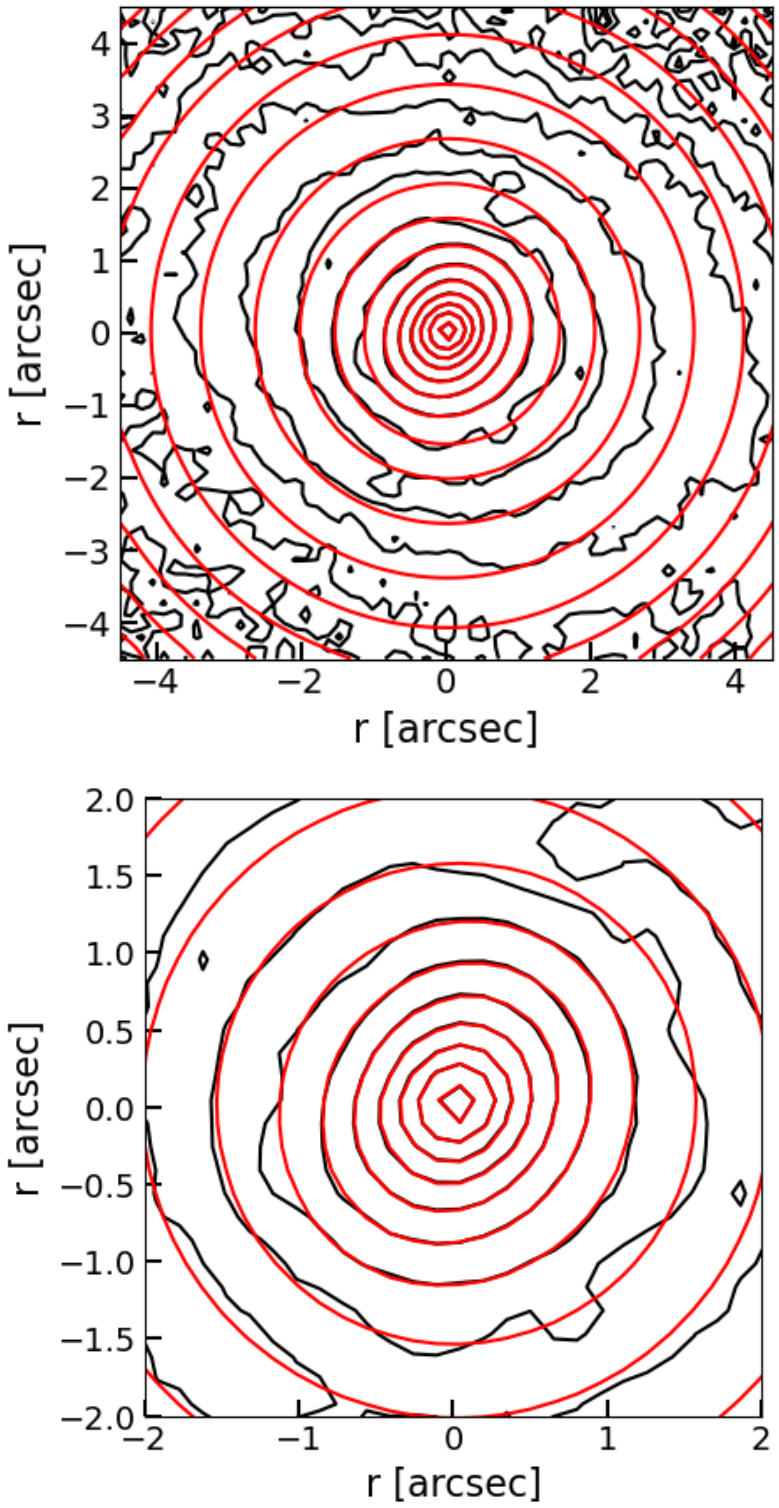

Figure 4.2
Wide-field and zoom-in isophote plots of the source-subtracted image of Jackpot (black). The contours of the MGE model surface brightness are overlaid in red. The MGE is a good fit in the central regions, but deviations are evident at large radii due to the outer stellar envelope.

This treatment is sufficient to allow the natural robustness of MgeFit to follow the true luminosity distribution of the lens galaxy. Figure 4.2 shows isophote plots of both the galaxy HST image and the MGE model for each target in our sample, and it can be seen how the MGE model surface brightness is in good agreement with that of each lens galaxy in the regions shown (i.e. where our kinematics are measured).

Foreshadowing the indication in Chapter 5 that the Jackpot is not dynamically simple at greater radii, and the possible evidence for tidal interactions, Figure 4.2 shows an isophote plot of both the source-subtracted image of Jackpot and the MGE model. The MGE model surface brightness is in good agreement with that of the galaxy in the inner ~ 2 arcsec (i.e. where our kinematics are measured), but poorly reproduces the shape of the observed isophotes beyond this, where the light from the diffuse outer envelope becomes significant, as also seen in Figure 2.1. We note the presence of this same effect in Figure 1 of Posacki et al. (2015), but find that in comparison, our treatment of the HST image works in reducing the contamination from the bright arcs and improves the model fit in the inner regions.

4.1.2 Dark Matter Halo

A process analogous to the one described in Section 4.1.1 is followed to obtain a second set of Gaussians characterising the galaxy DM surface density. Under the assumption of a spherical DM halo, the density distribution is well-described by a generalised NFW profile (gNFW; Zhao, 1996) of the form

$$\rho_{\rm DM} = \frac{1}{(r/r_{\rm s})^{\gamma}(1 + r/r_{\rm s})^{3-\gamma}}, \tag{4.1.2}$$

where r is the physical radius and with $\gamma = 1$ corresponding to the original NFW slope. Here $r_{\rm s}$ is the scale radius, fixed at 100 arcsec for the Jackpot lens based on reasonable assumptions for the virial radius of the order 600 kpc (as per Gavazzi et al., 2007), a halo concentration parameter of $c_{\rm vir} \approx 6$ (from a mass-concentration relationship from Macciò et al., 2008) and given the NFW halo density profile. It was found that varying this value

slightly (i.e. by 20%) had very little effect on the recovered kinematic estimates, as is expected since the observational constraints are well inside r_s.

In our use of the gNFW profile, we are not assuming any specific physical origin of any difference with respect to the NFW profile, but a slope of $\gamma > 1$ could represent, for example, a contraction in response to the baryonic mass (e.g Blumenthal et al., 1986; Gnedin et al., 2004; Dutton et al., 2007; Duffy et al., 2010; Grillo, 2012; Sonnenfeld et al., 2012).

As is detailed fully in Chapter 5, in our analysis of the Jackpot lens, we explore two distinct model sets; a set of models with the DM density slope as a free parameter, and a further set of models with the DM density fixed as a NFW profile (i.e. $\gamma = 1$). We identify a strong degeneracy between the DM density power law slope, γ, and the parameter describing the stellar mass as a fraction of the total lensing mass, $f_\star$, which precludes robust inference on the latter parameter. As such, in the subsequent work presented in Chapter 6, we opt to constrain the DM halo with an NFW profile. Chapter 5 investigates the consequences of treating the γ parameter as a free variable.

4.1.3 Excess Central Mass

In the construction of our dynamical models, we allow for a mass component describing any centrally concentrated mass in excess of a constant $M/L_\star$ ratio. We model this excess through the mechanism that JAM uses to model a central black hole, introducing an additional, very small Gaussian component. This gives the mass model a further degree of flexibility at smaller radii and accounts for any radial gradient in the stellar IMF (e.g. Martín-Navarro et al., 2015; La Barbera et al., 2017; van Dokkum et al., 2017), where a more pronounced $M/L_\star$ gradient is anticipated, suggesting a steep increase in mass within $\lesssim 1$ kpc.

While we expect the I-band image to serve as a reliable tracer of the stellar mass profile for systems with modest age and metallicity variations, this assumption may not hold true in the presence of radial IMF variation. Nevertheless, at the resolution of our data,

such a gradient is likely to be absorbed into our central mass component as a first-order approximation. We further discuss the simplification of a mass component of ~zero radius in Section 7.5.

4.1.4 Model Normalisation

In order to derive the total-mass surface density, the Gaussians resulting from the MGE fits to the luminous and dark components, as described in Sections 4.1.1 and 4.1.2 respectively, are combined with the excess central mass described in Section 4.1.3. A projected luminous fraction (i.e. the stellar mass as a fraction of the Einstein mass from lensing) is explored in the range $0 \leq f \leq 1$. We reduce the freedom in the dynamical models by rigidly enforcing a robustly-constrained lensing mass $m_{\rm E}$ at the Einstein radius, normalising the MGE such that

$$\frac{m_\star(<\theta_{\rm E})}{m_{\rm E}} + \frac{m_{\rm DM}(<\theta_{\rm E})}{m_{\rm E}} + \frac{m_{\rm cen}}{m_{\rm E}} = 1 \ , \tag{4.1.3}$$

where $m_\star(<\theta_{\rm E})$, $m_{DM}(<\theta_{\rm E})$ and $m_{\rm cen}$ are the projected mass contributions from stars, DM and the central excess, to the total Einstein-aperture lensing mass.

Furthermore, in the work described in Chapter 6, we investigate models in which the imposed lensing mass is permitted to vary as a free parameter, scaled by a factor ζ. A detailed discussion of the ensuing results can be found in Section 6.4, with the broader implications explored in Section 7.3.

4.2 Anisotropic Modelling and Parameter Search

Normalised MGE descriptions of the surface brightness and total-mass surface density profiles, in conjunction with the variable parameters outlined in this chapter, are used to calculate a prediction of the projected $v_{\rm rms}$ field for an anisotropic, axisymmetric galaxy model. The prediction incorporates a convolution with the MUSE PSF, approximated as a

Gaussian function with a FWHM of 0.5 arcseconds[†]. The predicted second-order moments are subsequently computed at the luminosity-weighted Voronoi bin centres to facilitate comparison with the observed data.

Using a Markov chain Monte Carlo (MCMC) Ensemble sampler (Foreman-Mackey et al., 2013), we systematically sample the parameter space for a model ensemble characterised by velocity dispersion ellipsoids aligned with the cylindrical (R, z) coordinate system (the cylindrical JAM method; Cappellari, 2008, 2012). Within the cylindrically-aligned paradigm, the orbital anisotropy parameter is defined as $\beta_z = 1 - \overline{v_z^2}/\overline{v_R^2}$ (Cappellari, 2008), such that $\beta > 0$ corresponds to flattening of the velocity dispersion ellipsoid in the vertical direction. We define the prior probability density function (PDF) for all parameters using flat priors subject to physically motivated constraints. The free parameters of our models are summarised as follows:

- γ, the DM density power law slope. Values in the range $0.5 \leq \gamma \leq 3$ are explored, with $\gamma = 1$ describing the standard NFW slope;
- β, the orbital anisotropy parameter which, in the cylindrically-aligned case, describes the ratio of the radial velocity dispersion to the vertical component. Here we consider values of $-0.6 \leq \beta \leq 0.6$, where a negative value of beta indicates a relatively larger vertical velocity dispersion.
- $f_\star$, the stellar mass as a fraction of the total lensing mass, explored from $0 \leq f_\star \leq 1$;
- $m_{\rm cen}$, the excess central mass. Here, the mass range $0 \leq m_{\rm cen} \leq 7 \times 10^{10}$ $M_\odot$ is explored.
- i; the galaxy inclination, with a lower limit imposed by the minimum observed axial ratio of the MGE Gaussians describing the distribution of the kinematic-tracer population. This parameter is defined such that an inclination of 90° corresponds to the edge-on case.

[†]The smoothing imposed by the Voronoi binning in the case of the Jackpot does not exceed the PSF until a mean radius of ~ 1.42 arcsec, beyond which point the $v_{\rm rms}$ field is slowly varying on the relevant scales.

CHAPTER 5

Two-dimensional kinematics and dynamical modelling of the 'Jackpot' gravitational lens from deep MUSE observations

You can't expect to hit the jackpot if you don't put a few nickels in the machine

~ Flip Wilson

5.1 Introduction

Double-source-plane lenses (DSPLs), or compound lenses, are a rare and valuable type of gravitational lens system, occurring when a single foreground lens galaxy simultaneously multiply-images two background source galaxies at different redshifts. The best studied example of a DSPL to date is the 'Jackpot' $z = 0.222$ lens (SDSSJ0946+1006), discovered serendipitously by Gavazzi et al. (2008) as part of the Sloan Lens ACS survey (Bolton et al., 2006). The Jackpot system consists of a bright ring at $z = 0.609$ and a further ring at a greater radius, indicating a more distant second source ($z_{\rm spec} = 2.035$) from which

constraints on the cosmological parameters can be obtained (Collett & Auger, 2014; Smith & Collett, 2021). A further multiply-imaged source at $z \approx 6$ has been reported by Collett & Smith (2020), making Jackpot a triple-source-plane lens system.

The Jackpot system hosts one of only a few cases of a dark substructure detected through lensing perturbations (see Vegetti et al., 2010). The substructure is cited as having a mass high enough that one would expect it to host a luminous galaxy, as well as having a surprisingly high central density. The primary lens has also been reported to have a steep density slope by Minor et al. (2021), a claim that sits in contention with that of earlier findings in Collett & Auger (2014). The authors note that the peculiar inferred properties of the subhalo could be due to a deviation from the CDM paradigm with respect to the particle physics of DM, such as dark matter self-interactions (see Colín et al., 2002; Vogelsberger et al., 2012; Zavala et al., 2019; Turner et al., 2021), in which case one would expect to detect many more highly concentrated substructures in future surveys. They also note, however, that the substructure properties could be affected by the lack of generality in their model, stating that a more flexible host galaxy combined with spatially resolved kinematics could provide stronger constraints for the subhalo concentration.

As a result of its astrophysical significance and applications in addressing open cosmological questions, the lensing properties of the Jackpot have been intensively studied. In contrast to this, and despite the additional advantages that kinematic data can bring to breaking degeneracies, only relatively limited kinematic measurements exist for the lens system (e.g. Auger et al., 2009; Sonnenfeld et al., 2012; Spiniello et al., 2015). These studies used single-slit observations, such as the 1 arcsec-wide slit used in Sonnenfeld et al. (2012), yielding measurements to $\sim$ 1 arcsec from the centre of the lens, and the 2×1.5 arcsec slit of Spiniello et al. (2015), and thus cover only a moderately small radial distance. As a result, this limits the area from which measurements can be obtained to within the bright Einstein ring, effectively excluding the radial ranges at which DM contributions become more significant and resulting in restricted spatial information.

In the work presented in this chapter, we present a combined kinematic and dynamical analysis of the Jackpot lens galaxy. We apply template fitting methods, as described in

Chapter 3, to deep integral field unit (IFU) spectroscopic data from the MUSE instrument, and employ anisotropic dynamical Jeans models, as described in Chapter 4, that are robustly constrained by the lensing mass at the Einstein radius, to measure the total 2D-projected density profile slope of the lens galaxy. We explore parameter space for two distinct model sets with velocity dispersion ellipsoids aligned with the cylindrical (R, z) polar coordinate system; a set of models with the DM density slope as a free parameter, and a further set of models with the DM density fixed as a NFW profile.

5.2 Kinematic Template Fitting Results

Figure 5.1 shows the derived velocity map for an $\sim 8{\times}10\,\mathrm{arcsec}^2$ area and clearly displays the axis of rotation of the lens galaxy, giving maximum velocities of $\sim \pm 100\,\mathrm{km\,s^{-1}}$ about a kinematic axis with a misalignment with the photometric axis of the order 10°, dependent on the radius at which they are measured[‡].

This rotation has been hinted at in previous works, with Sonnenfeld et al. (2012) noting evidence for some rotation in their analysis; however, the paper states that the stellar kinematics of the lens galaxy are dominated by pressure support, rather than rotation. Our data confirms that the kinematics are indeed dispersion dominated, with $v_{\mathrm{rot}}^2 \ll \sigma^2$. Figure 5.1 demonstrates the way in which our high-area-coverage MUSE data and multiple-component fitting allow us to fully map the 2D-kinematic properties of the Jackpot lens galaxy, out to a much greater radius than previous single-slit studies, allowing us to now fully characterise the rotation proposed by Sonnenfeld et al. (2012).

Figure 5.1 also shows the velocity dispersion map of the lens galaxy and illustrates the way in which σ falls from $\sim 280\,\mathrm{km\,s^{-1}}$ at the centre of the lens to $\sim 230\,\mathrm{km\,s^{-1}}$ at a radius of ~ 2 arcsec, and highlights a discernible velocity dispersion gradient in the inner region.

Figure 5.2 shows the radial velocity dispersion profile derived from this study, as compared with that of Spiniello et al. (2015), Sonnenfeld et al. (2012) and Auger et al. (2009). Our

[‡]The photometric position angle was measured using the MgeFit package (Cappellari, 2002). The outer edge of the Voronoi binning is defined by a low-surface brightness envelope that is almost orthogonal to the true major axis of the galaxy.

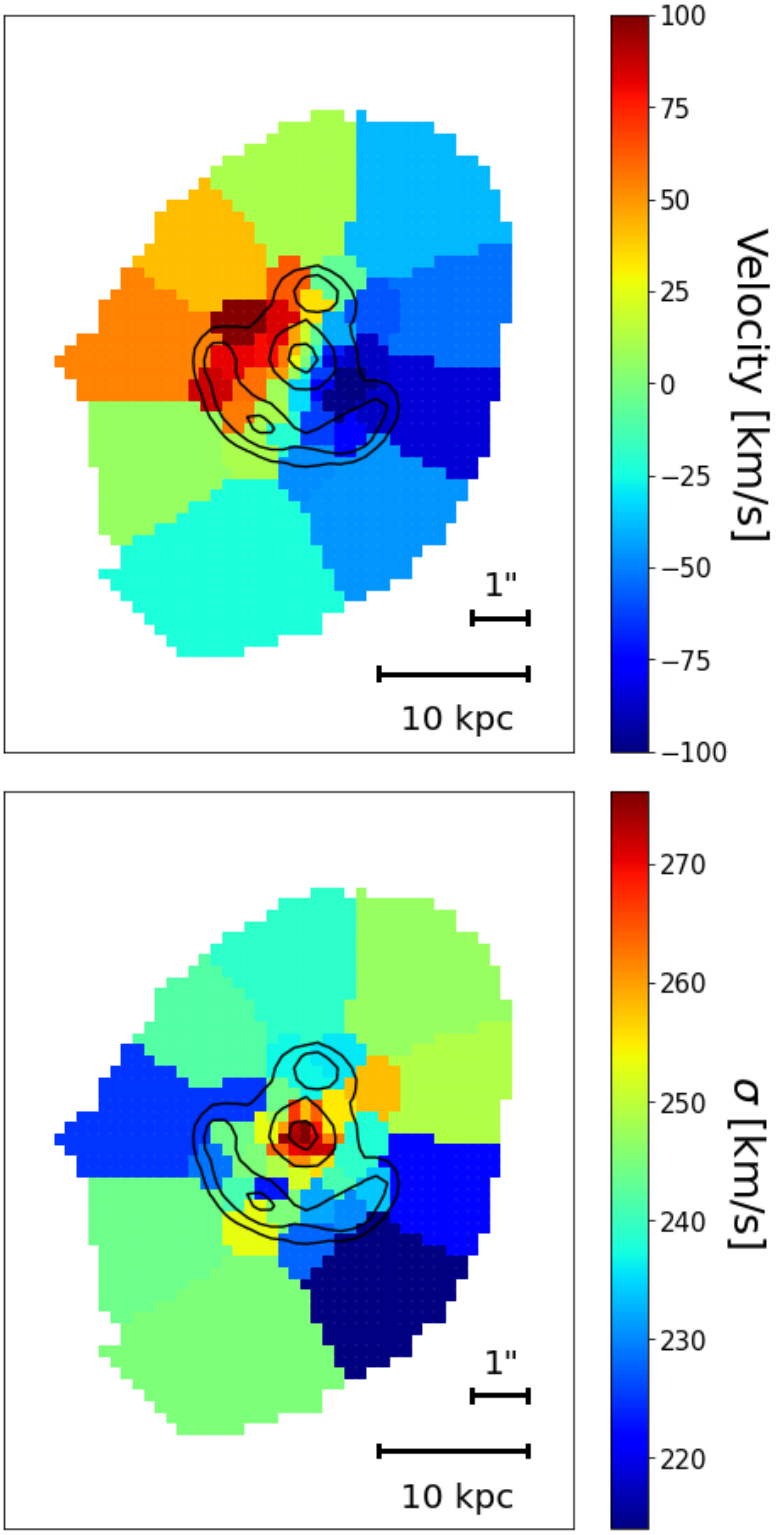

Figure 5.1
Velocity and velocity dispersion maps for an $\sim 8{\times}10\,\mathrm{arcsec}^2$ region of the Jackpot, overlaid on contours of the galaxy flux. The upper panel shows a clear signature of rotation along the major axis and the lower panel shows a falling velocity dispersion gradient.

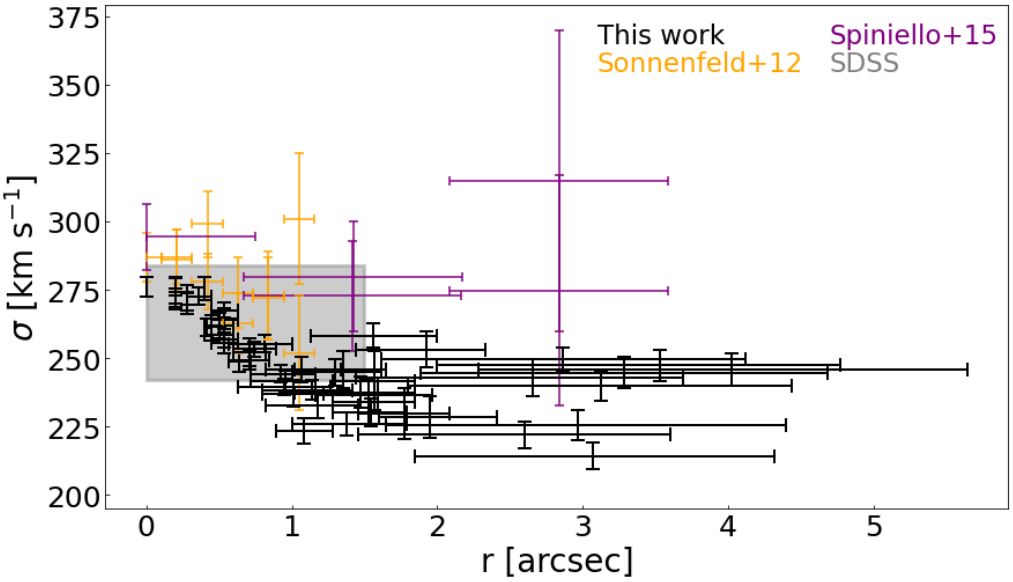

Figure 5.2
The velocity dispersion of each Voronoi bin as a function of radius. For comparison, we show measurements from Spiniello et al. (2015), Sonnenfeld et al. (2012), and SDSS (Auger et al., 2009). Our data are broadly consistent with previous measurements in the inner regions, but show a clear decline in velocity dispersion towards a larger radius, where the precision of earlier datasets is lower.

measurements agree with those of previous studies in the regions with overlapping coverage (i.e. the inner ~2 arcsec). In the regions at larger radii than this, our measured profile exhibits the "quadrupole" structure seen in the velocity dispersion map in Figure 5.1, with velocity dispersions that are lower on the kinematic major axis (the region where rotation is greatest) and higher on the kinematic minor axis. This behaviour is still found if we adopt very large bins in the outer regions; we further discuss the implications of this result in Section 7.4.

5.3 Dynamical Mass Modelling Results

As seen by the extended envelope in Figure 2.1, and further reflected in Figure 5.1, we measure our stellar kinematics out to ~ 10 kpc (~ 2.7 arcsec) from the centre of the lens. However, preliminary tests of our dynamical models showed indications that the Jackpot is not dynamically simple at greater radii, and we note here the possible evidence for tidal interactions found in Sonnenfeld et al. (2012). This presents a fundamental limitation of

Table 5.1
The median and 68% confidence bounds for the model parameters from both of our model sets.

Model	γ	β	$f_\star$	$m_{\rm cen}[10^9 {\rm M}_\odot]$	$i[^\circ]$
Free γ	$1.73^{+0.17}_{-0.26}$	$-0.03^{+0.03}_{-0.03}$	$0.38^{+0.19}_{-0.23}$	$8.23^{+2.56}_{-3.67}$	64^{+17}_{-16}
NFW	(= 1)	$-0.01^{+0.04}_{-0.04}$	$0.71^{+0.04}_{-0.03}$	$7.31^{+1.82}_{-1.82}$	51^{+21}_{-10}

how well we can model the lens kinematics in the outer region, as this component cannot be accommodated by our simple dynamical models, which are limited to oblate axisymmetric mass and luminosity distributions. If indeed just tidal debris, we do not expect this to be very dominant in mass, but including the tracers in this region in the modelling could bias the recovery of the mass components of interest.

As a result, we determine that our Jeans models are not appropriate to model the lens kinematics at greater radii, and as such, all dynamical models described herein are fit to the exclusion of our nine outermost bins. We thus opt to restrict the radius for dynamical model predictions to 1.95 arcsec, which is still sufficient to allow projected mass slope measurements at the Einstein radius. We further discuss this choice and its implications in Section 7.4. The measured kinematics for this restricted region are shown in Figure 5.3, the final panel of which shows the fractional increase of the second velocity moment by ordered rotation, which further demonstrates that the galaxy is dispersion dominated within the fitted radius.

Using the likelihood derived from the predicted and observed $v_{\rm rms}$, and given the priors above, we sample the posterior PDF for the five model parameters. Figure 5.4 shows the marginalised parameter constraints, which are given in Table 5.1. The results of our modelling can be summarised as follows:

5.3.1 Dark Matter Density Power Law Slope, γ

Our inferred DM density slope, taken from the model set with γ as a free parameter, is $1.73^{+0.17}_{-0.26}$, significantly steeper than an unmodified NFW profile (i.e. $\gamma = 1$). Such a slope

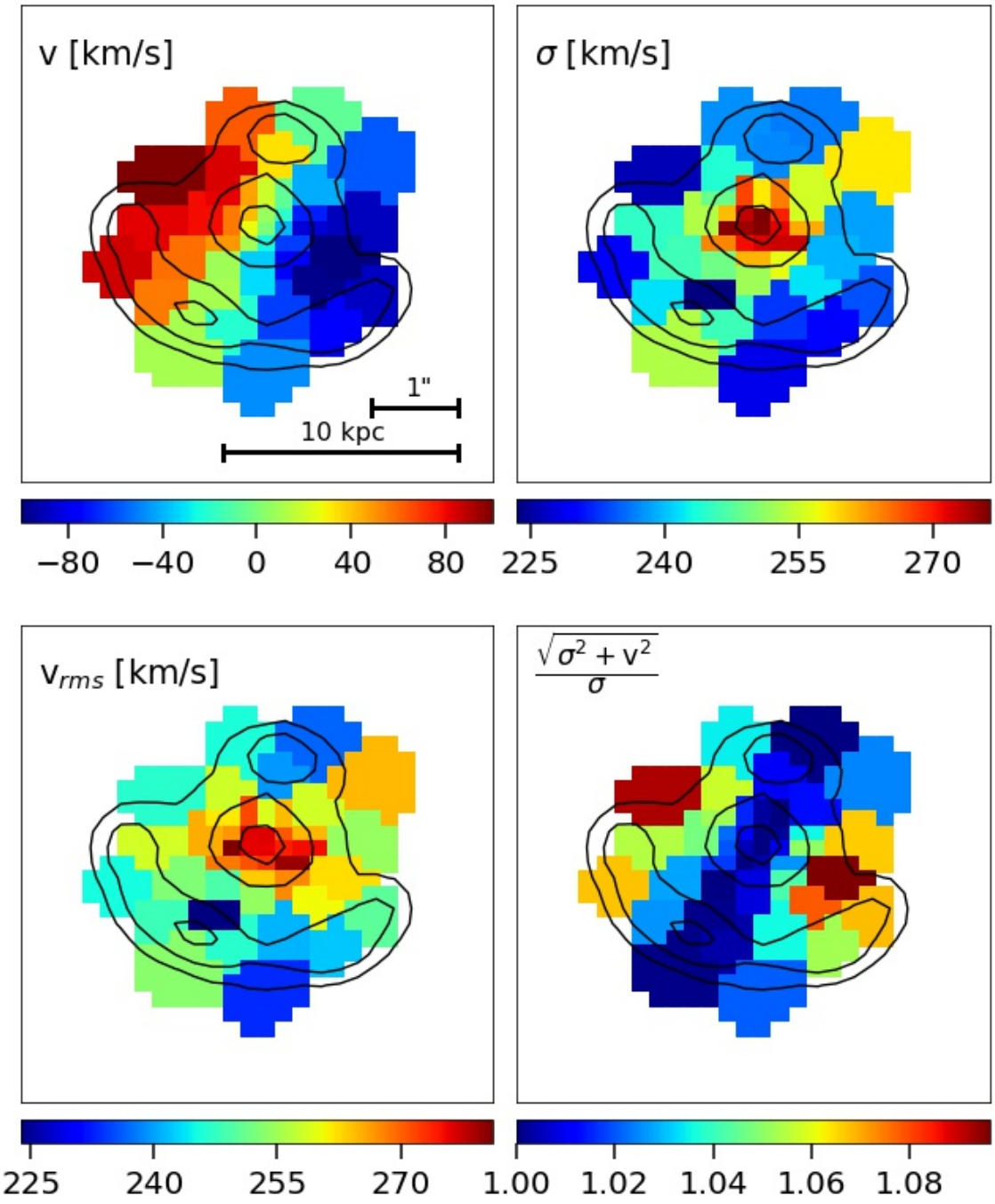

Figure 5.3

The measured kinematics from the restricted data, corresponding to the region used for dynamical modelling. The final panel shows the fractional increase of the second velocity moment caused by ordered rotation.

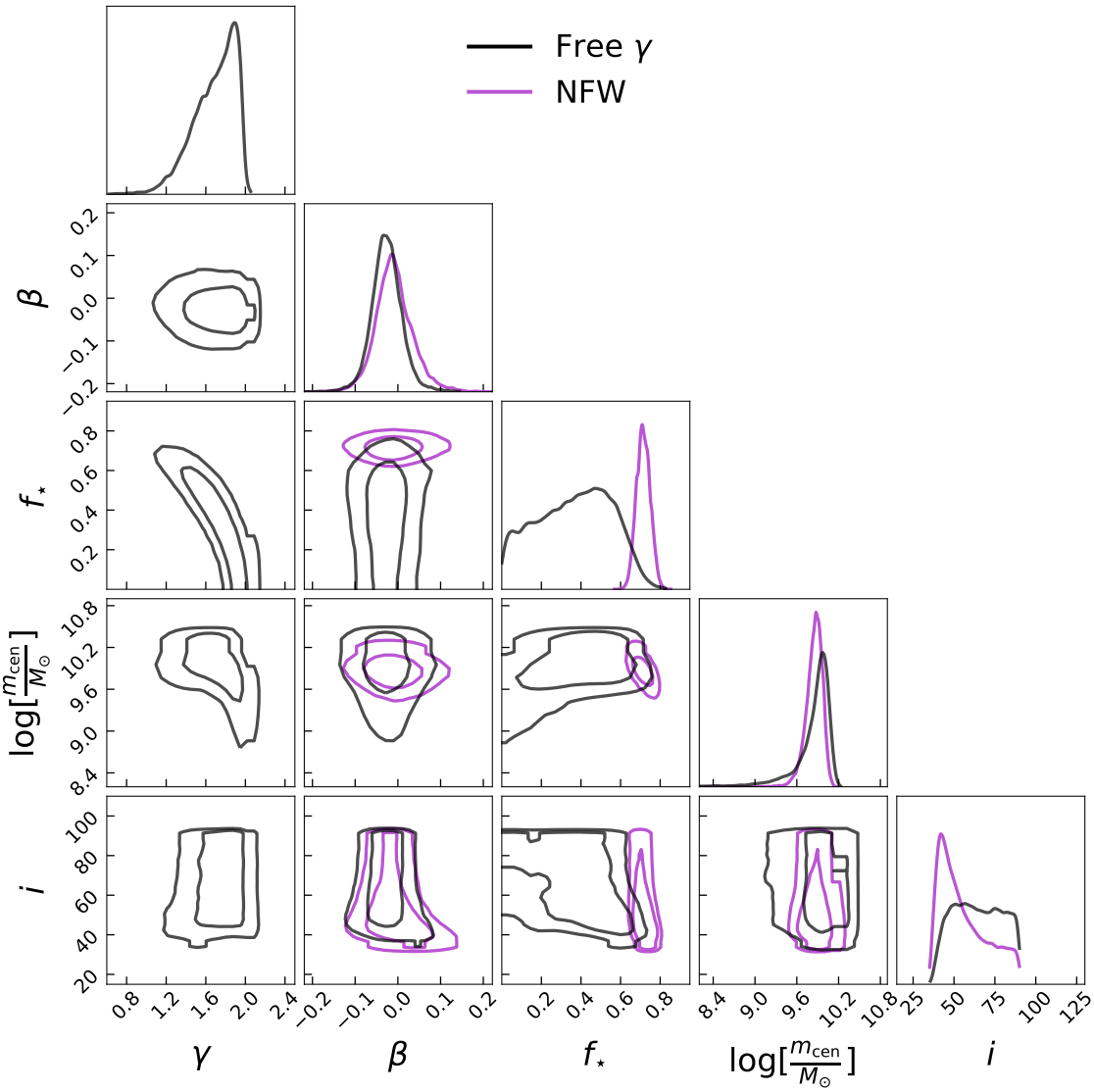

Figure 5.4

The posterior PDF for the free γ and NFW model parameters. The contours show the 68 and 95% confidence regions. The parameters explored are: the inner slope of the DM density profile, γ; the orbital anisotropy parameter, β; the stellar mass as a fraction of the total lensing mass, $f_\star$; any central mass in excess of a constant stellar mass-to-light ratio, $m_{\rm cen}$; the galaxy inclination, i. The diagonal plots show the marginalised posterior densities for each parameter.

could represent a baryon-contracted halo appropriate to a massive galaxy (Sonnenfeld & Cautun, 2021). We find that models with a slope flatter than NFW are strongly disfavoured, but not disallowed.

5.3.2 Orbital Anisotropy Parameter, β

The velocity ellipsoid is strongly constrained to be nearly isotropic in both model sets, with orbital anisotropy parameters of $\beta = -0.03 \pm 0.03$ and $\beta = -0.01 \pm 0.04$ for the free γ and NFW cases respectively, which is consistent with the low values typically found, e.g. for $\sigma > 200\,\mathrm{km\,s^{-1}}$ galaxies in the ATLAS^{3D} survey (Cappellari et al., 2011). The model likelihood is rather insensitive to the orbital anisotropy, although this is perhaps to be expected given the context of the assumed cylindrically-aligned coordinate system.

5.3.3 Stellar Mass Fraction, $f_\star$

In the free γ models, there is a strong degeneracy between $f_\star$ and γ, which prevents us from obtaining closed inference on the stellar fraction. Instead, a range of $0.15 < f_\star < 0.57$ is somewhat weakly favoured. Thus, the inferred mass budget inside the Einstein radius for the models with a free DM density slope is $m_\star : m_{\rm DM} : m_{\rm cen} = 0.38 : 0.59 : 0.03$, albeit with substantial uncertainty. For the models with a fixed NFW-like DM density, this parameter is much more tightly constrained and the mass budget is $0.71 : 0.27 : 0.02$. The expected stellar mass fraction under the assumption of a Chabrier IMF is $f_\star^{\rm Chab} = 0.26 \pm 0.07$, whilst with a Salpeter IMF we expect $f_\star^{\rm Salp} = 0.46 \pm 0.13$ (Auger et al., 2009). Our preferred stellar mass fraction for the free γ models is broadly consistent with that of a Salpeter IMF. For the NFW models, we find a stellar mass fraction heavier than the predictions of a Salpeter IMF and that is inconsistent with a Chabrier IMF.

In the free γ case, a DM mass fraction of $f_{\rm DM} = 0.59^{+0.24}_{-0.19}$ was inferred. This sits in good agreement with that of Gavazzi et al. (2008), who found a surprisingly high DM mass fraction inside the effective radius (2.0 arcsec for the Jackpot) of $f_{\rm DM}(< R_{\rm eff}) = 0.73 \pm 0.09$.

Here, the DM mass fraction is defined simply as the difference between the total lensing mass and the combination of the stellar and excess central masses.

The stellar mass as a fraction of the total lensing mass is highly degenerate with the free DM density power law slope; this is to be expected as, to first order, either reducing the stellar fraction at the expense of the DM fraction, or flattening the DM profile, act to effectively predict larger root-mean-square velocities at larger radius. Despite γ being free to explore values up to a slope of 3, we see that our models do not exceed a slope of ~ 2 due to the hard prior imposed on the lower limit of the stellar fraction, and the strong anti-correlation between these two parameters. This behaviour is further demonstrated in Figure 5.5, which shows that the models with the steepest DM profile are also the models with the lowest stellar mass and smallest excess central mass. The apparent cut-off at $\gamma \sim 2$ corresponds to the case where the DM component accounts for the totality of the dynamical mass; there is simply no further flexibility in the mass budget for a steeper γ to be explored.

In the model set with a fixed NFW-like DM density slope, the stellar fraction is anti-correlated with $m_{\rm cen}$. We see that the models with a high stellar fraction prefer smaller excess central masses as, in the absence of flexibility from a free DM slope parameter, both components act to account for any compact additional central mass, so are free to compensate one another. The model set with a free γ does not demonstrate this behaviour, as there is instead the freedom for interplay between the three mass components in the models, constrained by the total lensing mass. In these cases, the greater concentration of DM in the central regions reduces the necessity for such a large excess central mass component, and suppresses the stellar contribution.

5.3.4 Excess Central Mass, $m_{\rm cen}$

The preferred excess central mass is well-constrained to be $\sim 8 \times 10^9\,{\rm M}_\odot$ for the free γ models, and $\sim 7 \times 10^9\,{\rm M}_\odot$ for the NFW models. If this component indeed represents only a central black hole, this would make it somewhat over-massive given the galaxy properties.

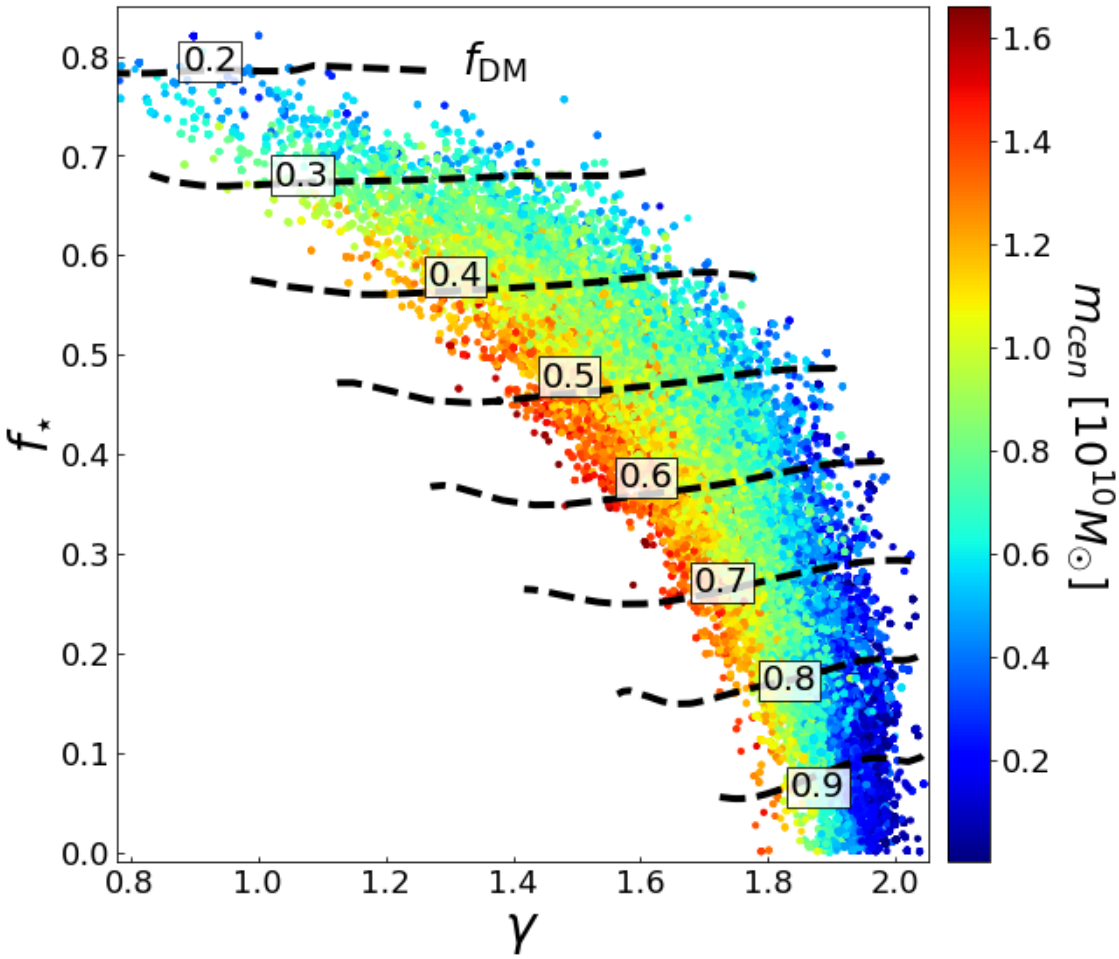

Figure 5.5

The stellar mass as a fraction of the total lensing mass for all free γ models, as a function of the DM density slope. Coloured points represent the preferred excess central mass and the black dashed line denotes contours for the corresponding DM mass fraction. This demonstrates the interplay between the mass model components and additionally highlights the way in which models with the steepest DM profile are also the models with the lowest stellar mass and smallest excess central mass. The apparent cut-off at $\gamma \sim 2$ corresponds to the case where the DM component accounts for the totality of the dynamical mass.

For a galaxy such as the Jackpot lens with a central velocity dispersion of $\sim 280\,\mathrm{km\,s^{-1}}$, from the standard black hole mass vs. sigma relation (van den Bosch, 2016), one would expect a central black hole with mass $\sim 1.6 \times 10^9\,\mathrm{M_\odot}$ (with a scatter of 0.49 ± 0.03). Given this discrepancy, it seems unlikely that all excess central mass is contributed by a black hole. We also note the potential for a systematic overestimation of the central mass component, as described in Appendix A and further discuss the implications of this in Section 7.5.

5.3.5 Galaxy Inclination, i

We found the galaxy inclination to be completely unconstrained in the free γ models, and only somewhat constrained in the NFW-like models, with an inferred inclination value of 51^{+21}_{-10}. More 'edge-on' inclinations up to 90° were not strongly excluded, but were instead disfavoured. In both cases, the inclination shows no significant covariance with the parameters of interest.

5.4 Total Mass and Logarithmic Density Profile Slopes

Figure 5.6 shows the 2D-projected mass profiles for each of the individual mass components described in Section 5.3, for both the free γ and NFW cases.

The large range of profiles and relative contributions in each model demonstrate the way in which the free γ models have a large degree of flexibility to effectively 'trade off' mass components at different characteristic radii. These models prefer a steep ($\gamma > 1$) DM density slope, and hence their range of DM projected mass profiles here are shallower than seen in the NFW models. The median contribution of the DM mass component is significantly greater for $r \lesssim 3$ arcsec than in the NFW models, as this model set has the freedom to allow for a greater concentration of DM mass in the central regions whilst still being constrained by the total lensing mass, thus dominating the total mass in the centre of the galaxy.

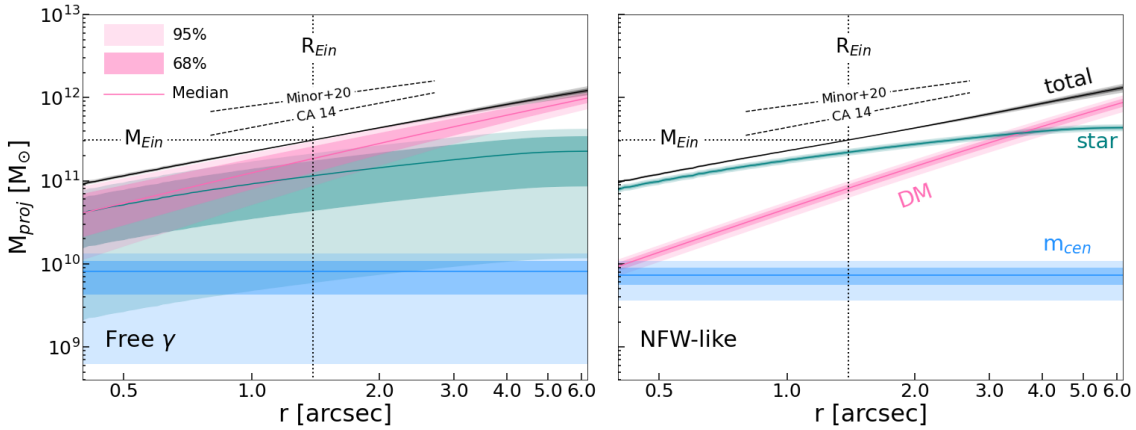

Figure 5.6

The 2D-projected mass profiles for each individual mass component: the stellar (green), DM (pink) and excess central mass (blue) components, as well as the total projected mass profile (black), for both the model with a free DM slope parameter (left) and the model with NFW-like DM (right). To enable comparisons, the slopes derived by Collett & Auger (2014) and Minor et al. (2021) have also been plotted. The vertical and horizontal dotted lines denote the Einstein radius and mass, respectively.

Conversely, the models with a DM density slope fixed at NFW-like show DM mass contributions that do not dominate the total projected mass until well outside the Einstein radius ($r \gtrsim 4$ arcsec), and instead prefer a more substantial stellar mass fraction. Indeed, Figure 5.6 shows that, in the absence of a steep enough DM halo, the NFW-like models are almost solely dominated by the stellar contribution in the central regions. Notwithstanding uncertainty in the relative component contributions, the projected mass profile at the Einstein radius is tightly constrained by the data, and the flexibility afforded to the model parameters results in almost indistinguishable recovered total mass slopes.

Figs. 5.7 and 5.8 show the $v_{\rm rms}$ predictions from our best model, which reproduces the data well over the full range of measurements, compared to predictions of a model without a DM halo, that attributes the gravitational potential solely to luminous matter and any additional central mass, and of a further model with no excess central mass component. As we only constrain our total mass around the Einstein radius, our three contributing mass parameters (stellar, DM and central) are free to compensate one another, e.g. in the absence of the excess central mass required to reproduce the observed higher velocities in the innermost regions (where the $m_{\rm cen}$ component would dominate), consequent adjustment between the

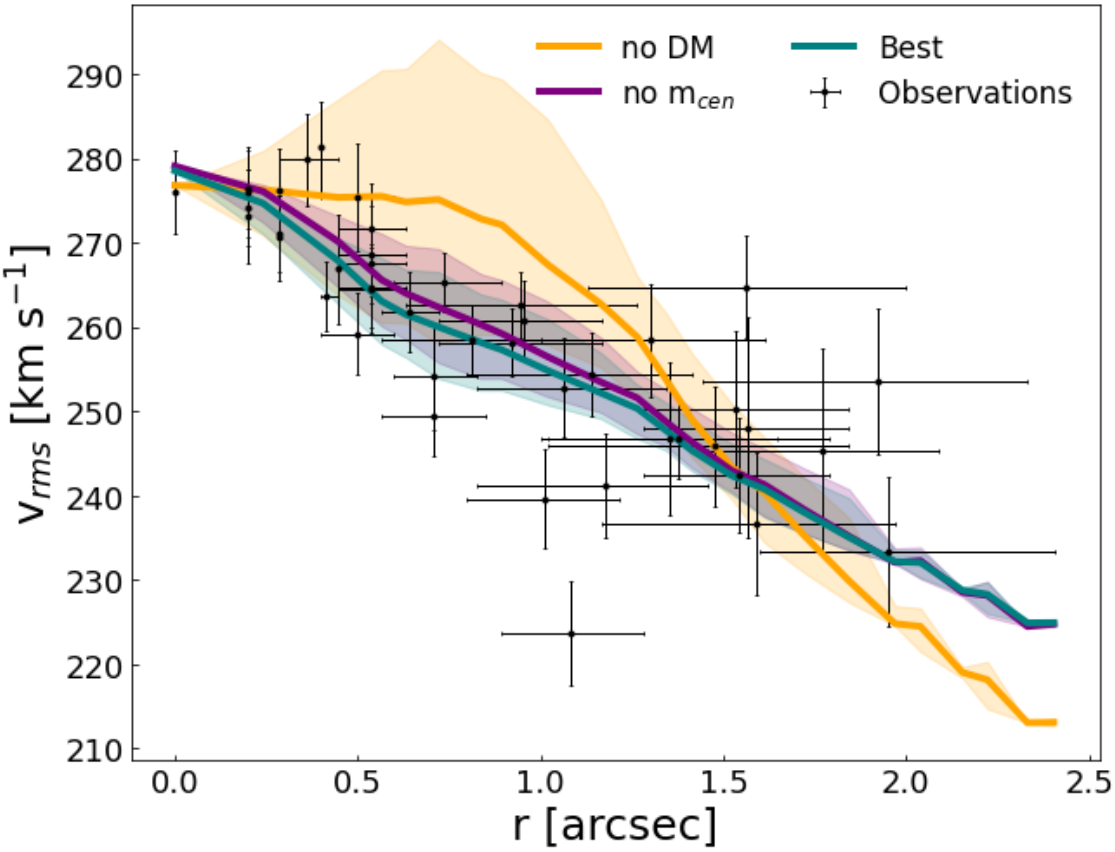

Figure 5.7

The mean and azimuthal range of the root-mean-square velocity predictions from our best model (green) compared to the best possible model without an excess central mass (purple), and the best model predictions without accounting for the mass in DM (orange). Also shown are the measured $v_{\rm rms}$ from each Voronoi bin as a function of radius (black). The horizontal error bars of the observed data represent the width of the Voronoi bins. The model set without a DM halo fails to predict the observed kinematics, while the model set without an excess central mass can successfully reproduce the kinematics, although in this case the recovered stellar mass and DM halo profile are unreasonable (see text).

DM and stellar components are necessary to produce the steep inner $v_{\rm rms}$ profile. The kinematic predictions from the best fitting dynamical model exhibit a clear gradient in $v_{\rm rms}$, with values ranging from $\sim 280\,{\rm km\,s^{-1}}$ at the centre of the lens to $\sim 230\,{\rm km\,s^{-1}}$ in the outer regions, in close agreement with the observed kinematics, with relatively small residuals. The models that do not include all three mass components, however, unsurprisingly fail to predict the observed kinematics whilst simultaneously constraining model parameters that are realistic, as the models are not sufficiently flexible. Figure 5.8 shows that the angular structure of the model without an excess central mass component is similar to that of the best model, while the no-DM model demonstrates prominent high $v_{\rm rms}$ lobes along the major axis. The model without a DM halo substantially overestimates the $v_{\rm rms}$ in a range $0.2\,{\rm arcsec} \lesssim r \lesssim 1.2\,{\rm arcsec}$. This is a result of the total mass distribution of the lens being solely constrained by the centrally-concentrated luminous MGE in this case, and lacking an extended mass component. The model without an excess central mass component successfully reproduces the observed kinematics at all radii, but does so at the expense of requiring an unrealistic stellar mass fraction ($f_\star = 0.09$) and a very steep DM density profile ($\gamma = 1.97$). This is consistent with the γ-$f_\star$ panel in Figure 5.4 and the dark blue data points in Figure 5.5. While formally consistent with the lensing and dynamics, relative to the tabulated values of Auger et al. (2009), a model with such a low stellar mass fraction would imply a stellar IMF that is a factor of 2-3 lighter even than the Chabrier IMF.

5.4.1 Total Mass Profile Slope

To compare our result to previous (non-dynamical) lensing studies of the Jackpot, we must relate our composite profile results to the power-law total density profile used in the lensing literature, (e.g. Collett & Auger, 2014; Minor et al., 2021; Etherington et al., 2022)[§]. The sum of a stellar component and a dark matter halo does not yield a power-law total density profile, yet making this approximation has historically been acceptable, due to the so-called

[§] In practice, our composite profile is close enough to a power law that the two slopes are expected to be very similar.

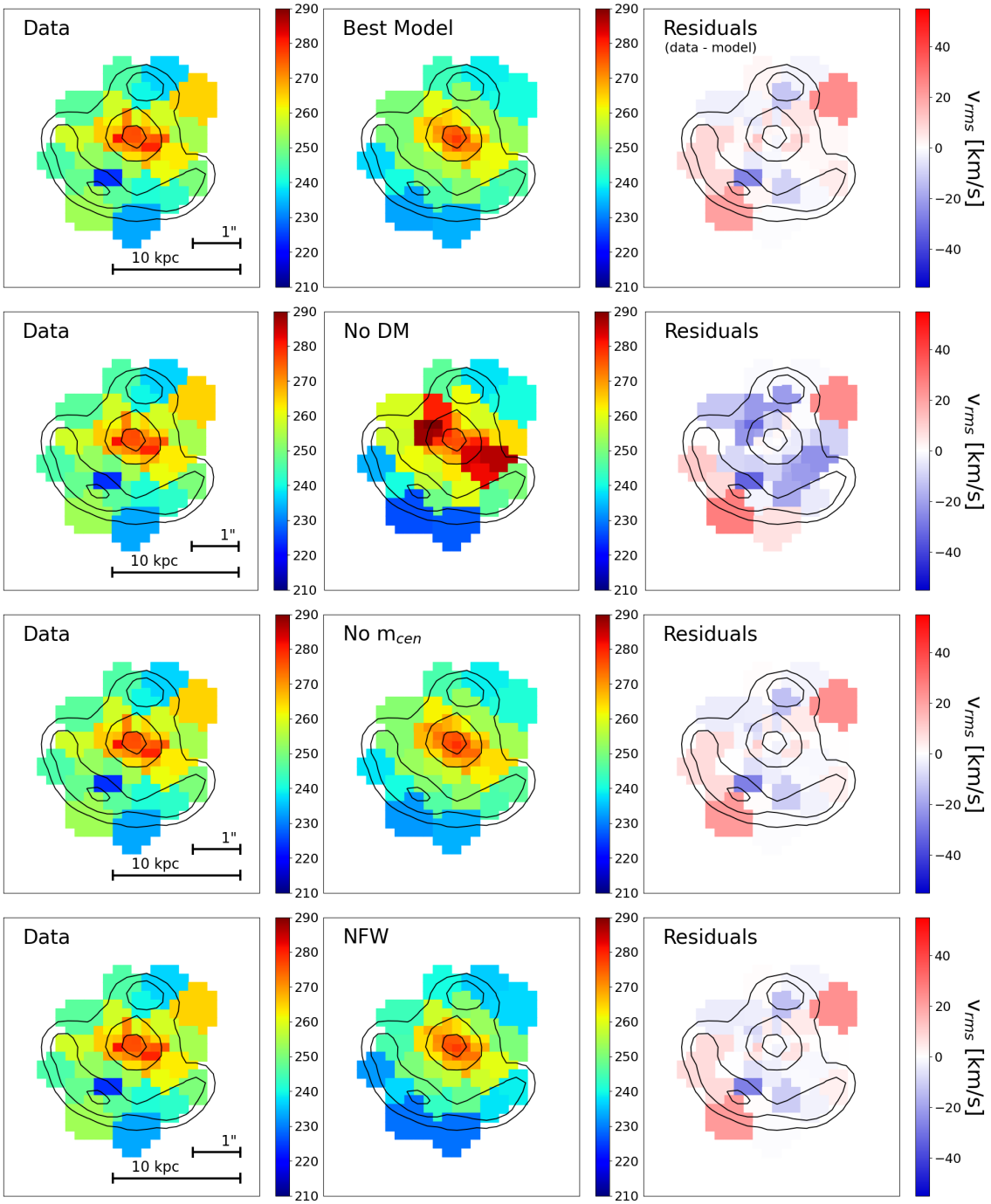

Figure 5.8

Kinematic maps for the root-mean-square velocities, $v_{\rm rms}$, obtained from the data, alongside the best fitting models for each scenario described in Figure 5.7 and the model with an NFW-like, fixed $\gamma = 1$ DM slope. Also shown are the model residuals. The best fitting model exhibits a clear $v_{\rm rms}$ gradient and the residuals are $\sim \pm 40\,{\rm km\,s^{-1}}$. The no-DM model exhibits higher residuals than the best fitting model and completely fails to predict the observed root-mean-square velocities obtained from the observed data.

bulge-halo conspiracy (Dutton & Treu, 2014): for lensing ellipticals, the sum of stellar and dark matter components is approximately isothermal over the length-scales probed by strong-lensing constraints.

To define an equivalent power law index from our composite model, we use all of the Gaussian components for the profile (constructed as described in Section 4.1) to compute the 2D-projected mass profile. For our free γ and NFW model sets, the *local* slope of this profile, at the Einstein radius, is 1.03 ± 0.03 and 1.07 ± 0.04 respectively. As this is a profile of integrated mass, a value larger than unity corresponds to a shallower-than-isothermal density profile.

5.4.2 Projected Logarithmic Density Slope

The local slope of the 2D-projected mass profile is not directly comparable to the lensing literature, as lensing does not strictly measure the local density slope at the Einstein ring. We instead calculate the power-law profile with the equivalent lensing effect as our inferred composite model[¶]. Collett (2014) and Kochanek (2020) showed that the slope inferred from lens modelling is sensitive to the radial derivative of the deflection angles at the location of the lensed images. The parameter we need to calculate is the dimensionless quantity ξ, which, after the Einstein radius, R_E, denotes the second property of the radial mass distribution that can be well-constrained by lensing data. Under the assumption of a power law mass distribution, ξ acts as a proxy to estimate the slope from lensing observations only, and is given as

$$\xi = \frac{R_E \alpha''}{1 - \kappa_E}, \tag{5.4.1}$$

where κ_E is the mean convergence at the Einstein radius and α'' is the second derivative of the deflection profile at R_E. As the uncertainties in R_E are typically small, the uncertainties in ξ will be dominated by the uncertainties in α''. For models that use a power law relation with surface mass density $\propto r^{-\eta}$, this quantity is given by

$$\xi = 2(\eta - 1). \tag{5.4.2}$$

[¶]This made use of code provided by a co-author of the paper.

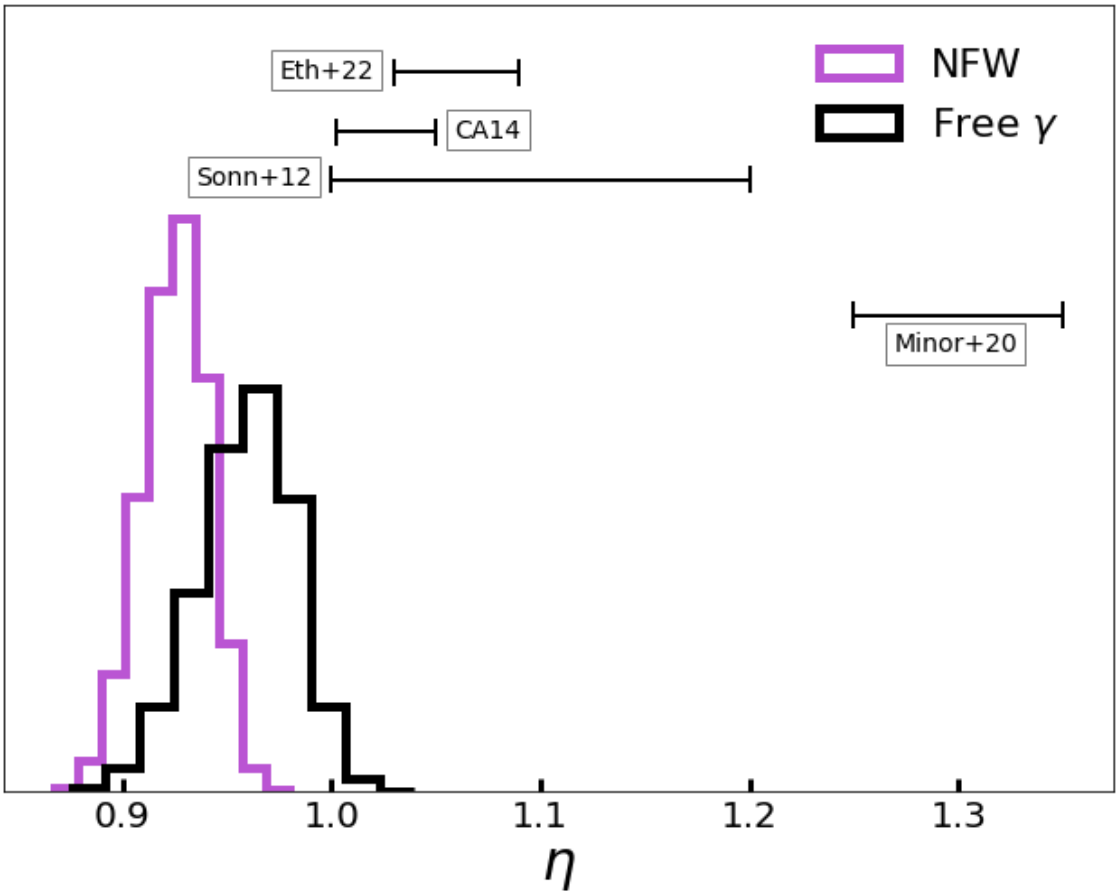

Figure 5.9
The 2D-projected total logarithmic density slope obtained from each of our two model sets; the free γ model and the NFW-like model. The slopes derived by Sonnenfeld et al. (2012), Collett & Auger (2014), Minor et al. (2021) and Etherington et al. (2022) and their respective errors have been included for comparison.

We therefore use our composite mass model to calculate ξ from Equations 5.4.1, and convert this to a lensing-equivalent power-law slope η using Equation 5.4.2. This gives us the value of η that should be measured from a lensing-only study for a mass profile with our best-fitting parameters. As shown in Figure 5.9, sampling from the posterior distribution, we find a projected logarithmic density slope of $\eta = 0.96 \pm 0.02$ for our free γ models and $\eta = 0.93 \pm 0.02$ for our NFW models. This indicates a density profile that is marginally shallower than the isothermal case, where $\eta = 1$.

CHAPTER 6

Two-dimensional kinematics and dynamical modelling of the SLACS gravitational lens sample from deep MUSE observations

For my part I know nothing with any certainty, but the sight of the stars makes me dream

~ Vincent Van Gogh

6.1 Introduction

Early-type galaxies (ETGs) hold a wealth of information regarding galaxy evolution and the processes shaping the large-scale structure of the Universe. Within the ΛCDM cosmological framework, their observed properties serve as crucial tests for the hierarchical merging paradigm (White & Rees, 1978; Davis et al., 1985; Cole et al., 1994). As the end products of this process, ETGs are sculpted by successive mergers of increasingly massive objects, offering a window into the entirety of galaxy formation and evolution. While lacking the grand, ordered disk and spiral arms characteristic of their more prominent

counterparts, ETGs offer unique opportunities to study stellar populations, probe the nature of DM, and constrain models of galaxy formation and interaction through their distinct morphologies and stellar kinematics.

The standard approach to dynamically modelling ETGs centres on solving the axisymmetric isotropic Jeans equations (e.g. Cappellari, 2008; van de Ven et al., 2010; Spiniello et al., 2011; Barnabè et al., 2012; Tortora et al., 2014, etc.). Here, the underlying mass distribution of the ETG is inferred by fitting a mass profile to the observed stellar v_{rms}. Typically, a two-component model is employed, encompassing both stellar and DM contributions. The stellar mass profile is often characterised by an MGE, offering flexible descriptions of the surface brightness distribution within the galaxy.

Given the prevalence of random stellar motions in elliptical galaxies, this approach is especially crucial for accurately modelling their dynamics, which are significantly more complex than the near-circular orbits of spiral galaxies. Nevertheless, the application of this method is subject to certain limitations and assumptions. For example, in the absence of detailed observations from high resolution data, analyses at any significant redshift are limited to simple dynamical Jeans type models (e.g. Cappellari, 2008), as opposed to more general triaxial orbit based models (e.g. Schwarzschild, 1979; van den Bosch et al., 2008).

For ETGs that act as gravitational lenses, the independent determination of their mass distribution becomes possible. At its simplest, strong gravitational lensing offers a powerful technique to directly infer the projected mass enclosed within the Einstein radius, providing a robust single-parameter estimate (Treu, 2010). With a more sophisticated pixel-based analysis (e.g. following Dye & Warren, 2005), however, lensing can probe the slope and shape of the mass density profile in the vicinity of the lensed images, particularly at large radii where dynamical studies hold limited sensitivity (e.g. Ritondale et al., 2019; Shajib et al., 2021; Etherington et al., 2022). Notwithstanding this, lensing-only studies can be susceptible to degeneracies arising during lens model construction, and intrinsically lack the sensitivity to probe the distribution of matter beyond the immediate vicinity of the lensed arcs. Further, as highlighted in Section 1.5.5, mass modelling of galaxy-scale lenses often relies on simplified single power law (SPL) or singular isothermal elliptical

(SIE) profiles. These models belie the true complexity of real galaxies, where higher-order multipole moments such as "diskiness" or "boxiness" (e.g. Bender et al., 1988; Hao et al., 2006; Cappellari, 2016; Amvrosiadis et al., 2024; Cohen et al., 2024; Stacey et al., 2024) and radial variations in the form of gradients and twists (e.g. Cappellari, 2002; Oldham & Auger, 2018; Sonnenfeld et al., 2018) demand more nuanced approaches to capture the full richness of a galaxy's mass distribution.

Chapter 5 presents results from a comprehensive kinematic and dynamical analysis of the 'Jackpot' (SDSS J0946+1006) $z = 0.222$ lens galaxy. This work marks the first 2D spatially resolved kinematic study of the system, leveraging new, deep MUSE integral field spectroscopic data obtained through a dedicated 5-hour integration. In this chapter, we present a direct extension of that work in a combined kinematic and dynamical analysis of a sample comprising 9 early-type SLACS lens galaxies. Applying the techniques of Chapter 5 to a wider sample, we leverage the exquisite spectral resolution of the MUSE instrument, employing stellar template fitting methods to analyse deep IFU data. Subsequently, we employ anisotropic dynamical Jeans models, robustly constrained by the lensing mass at the Einstein radius.

As discussed in Section 1.5.4, our sub-sample of SLACS lenses should be representative of the massive SDSS ETGs (e.g. Treu et al., 2006; Grillo et al., 2009; Auger et al., 2009). Consequently, conclusions derived from our analysis of them should be applicable to a wider range of lensing systems, including time-delay lenses and those with known substructures. The lens sample offers a rich dataset for our investigation, and by refining the lens macro model, we can establish robust priors for subsequent, higher-level lensing studies involving targets with limited observational data, such as faint quasar lenses.

6.2 Kinematic Template Fitting Results

Figure 6.1 shows the derived velocity and velocity dispersion maps of the lens galaxies within our sample. A notable fraction of the sample exhibits significant rotation, with five of the nine lens galaxies demonstrating maximum velocities of $\gtrapprox 60\,\mathrm{km\,s^{-1}}$ about the

kinematic axis, which might be indicative of the presence of disks or other higher order structure in the mass distribution. Furthermore, as is more clearly demonstrated in the radial dispersion profiles in Figure 6.2, there is a clear diversity in the individual profiles of the lens sample. Seven of the nine galaxies demonstrate a decreasing velocity dispersion gradient, characterised by varying degrees of steepness. In contrast, J0935 exhibits an increasing profile, while J0216 presents a flat velocity dispersion gradient. This is broadly consistent with the findings of Veale et al. (2018), who characterise the radial σ profiles of 90 ETGs in the MASSIVE survey[*] and also report diversity in the profiles and an increased fraction of rising dispersion profiles in the most massive galaxies and those with a dense environment. The kinematic properties of our sample are strongly dominated by pressure support, rather than rotation, with $v_{\rm rot}^2 \ll \sigma^2$ in all cases.

Resolved kinematics such as these provide a critical avenue for probing the intricate structures of real galaxy-scale lenses. By enabling the detection of kinematically distinct components within galaxies, these data offer invaluable insights into merger events and accreted stellar populations. A prime example of such a detection is shown in the velocity map of J1250, where a clear signature of a kinematically-decoupled core, characterised by two counter-rotating components, can be seen at the lens redshift of $z = 0.087$.

The pronounced rotational characteristics evident in a substantial fraction of our lens galaxy sample, coupled with the observed complex kinematics of J1250, suggest a potential departure from the conventionally employed SPL and SIE profiles in lens modelling analyses. We discuss this further in Sec 7.2.

6.3 Dynamical Mass Modelling Results

As described in detail in Chapter 4, we employ the anisotropic Jeans modelling framework, as instantiated in the JAM code (Cappellari, 2008, 2012), and construct self-consistent NFW + stars dynamical models to characterise the spatially binned kinematic data for each of the

[*] With a stellar mass selection criteria of $M_* \gtrsim 4 \times 10^{11} M_\odot$ for the MASSIVE survey, the galaxies in our sample have masses that much more closely resemble those of the MASSIVE survey than, for example, the ATLAS^{3D} survey.

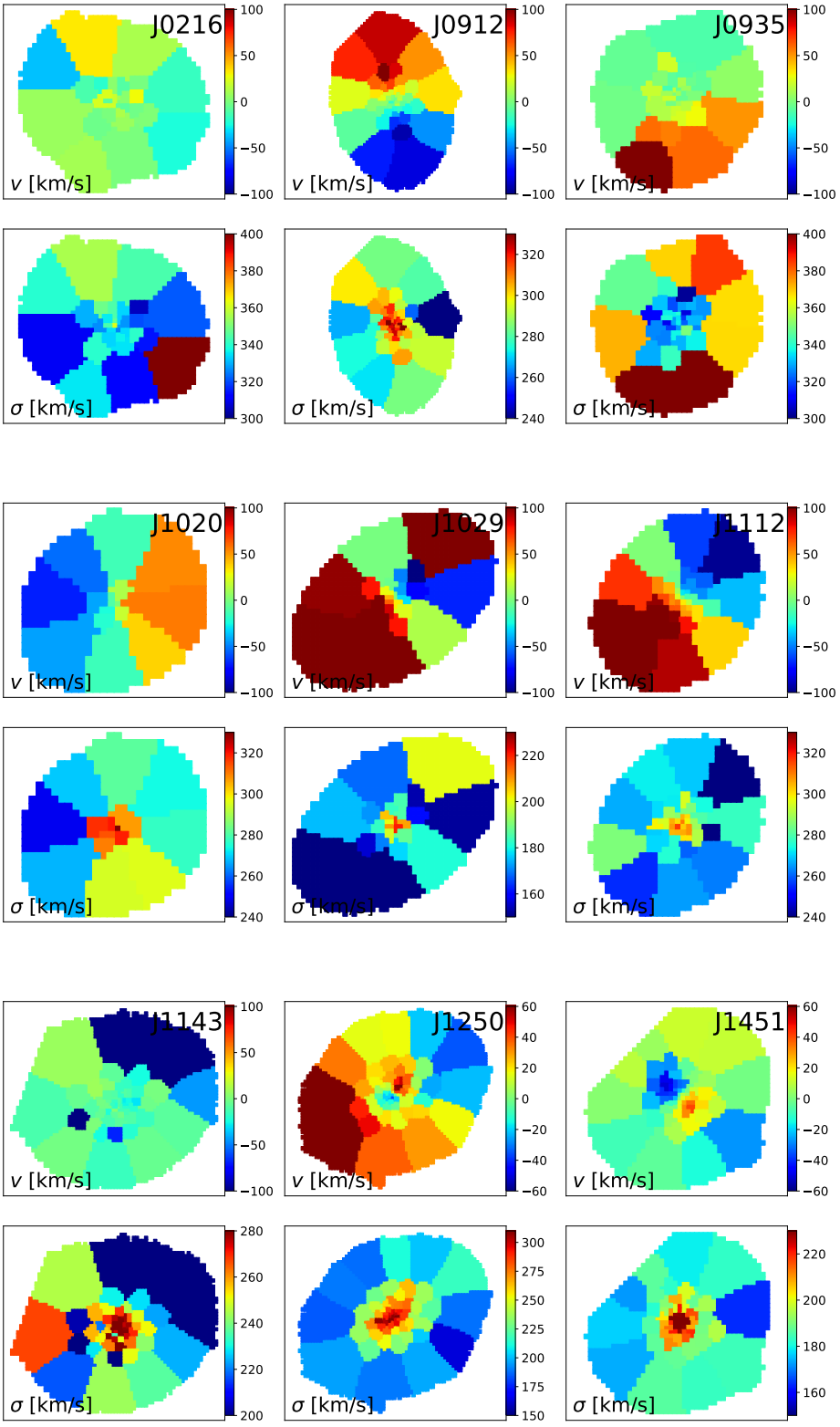

Figure 6.1

Velocity and velocity dispersion maps for the lens galaxy sample. Of the nine lenses, five exhibit significant rotation about the kinematic axis, and six display a strongly decreasing velocity dispersion gradient. Note that the same colour scale is used for all but the last two lenses (J1250 and J1451), due to low level but significant rotation being present in these two galaxies.

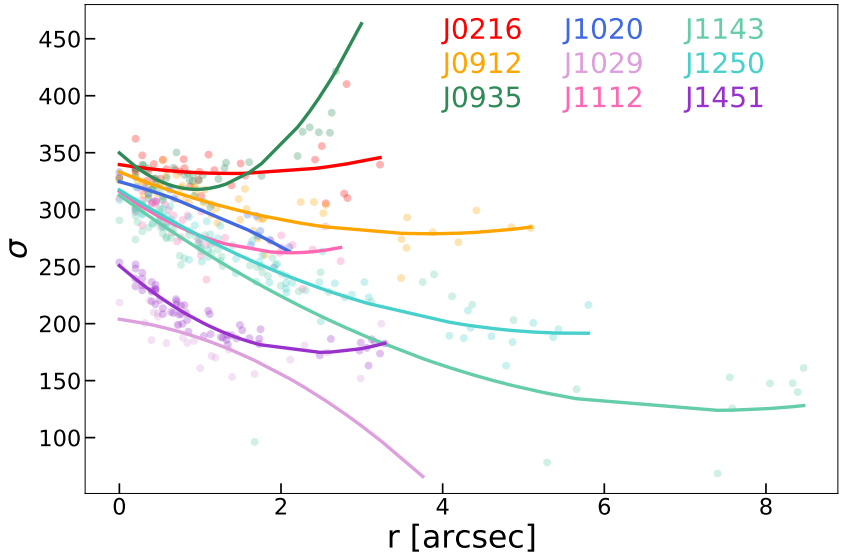

Figure 6.2
Velocity dispersion profiles for the nine SLACS lenses in our sample, with individual data points and profile fits.

lenses in our sample. Note that in this chapter, unlike the analysis presented in Chapter 5, we fix the DM density slope at $\gamma = 1$ for all dynamical models.

Through optimisation of the parameters as outlined herein, we maximise the likelihood associated with the observed root-mean-square velocities, $v_{\rm rms}$, and sample the posterior PDF for the model parameters under the assumptions of an NFW-like DM halo and a rigidly enforced lensing mass at the Einstein radius. The analysis of lens galaxies J1029 and J1143 was hindered by currently not-understood systematic errors unrelated to intrinsic peculiarities in the data. Consequently, we were unable to construct satisfactory models for these cases, and they have been excluded from our subsequent dynamical modelling results.

Figure 6.3 shows the marginalised parameter constraints, which are given in Table 6.1. The results of our modelling can be summarised as follows:

- Although the fitted orbital anisotropy, β, exhibits considerable scatter among individual galaxies, the velocity ellipsoids demonstrate a robust constraint towards near-isotropy, with a typical error of the order ± 0.01. The ensemble average across the galaxies converges at $\langle \beta \rangle = 0.12$, with a bounded range of 0.02 to $0.02 \leq \langle \beta \rangle \leq 0.28$. Whilst the original SLACS analysis assumed isotropic orbits,

the anisotropy range that we find is consistent with that of the ATLAS^{3D} survey (Cappellari et al., 2013)[^].

- The inferred stellar mass fraction, $f_\star$, spans a wide range of $0.14 \leq \langle f_\star \rangle \leq 0.97$, with evidence of intrinsic scatter from the individual galaxies typically below the 10% level. A mean value for the sample of $\langle f_\star \rangle = 0.59$ was found.

- The preferred excess central mass for the sample of lenses is well-constrained to be of mean $\langle m_{\rm cen} \rangle \approx 17 \times 10^9\,{\rm M}_\odot$, within a range of $2 \lesssim \langle m_{\rm cen}[\times 10^9 {\rm M}_\odot] \rangle \lesssim 46$. Given the $M_{\rm BH} - \sigma$ relation derived by van den Bosch (2016), these masses cannot be solely attributed to BH presence. Instead, for a mean velocity dispersion for the sample of $\sim 290\,{\rm km\,s^{-1}}$, it is expected that the true BH contribution to the central mass component will be less than $\sim 10^9 {\rm M}_\odot$.

- The stellar mass as a fraction of the total lensing mass is highly degenerate with the excess central mass parameter. This is to be expected as, to first order, increasing either parameter acts to effectively predict larger root-mean-square velocities at the very inner radii.

Figure 6.4 shows the 2D-projected mass profiles for each of the individual mass components described in Section 4.1, for each of the lens galaxies in our sample. By construction, the total mass profile of each galaxy passes through the Einstein mass and radius characteristic of that specific lens. A discernible dispersion exists among these profiles, with some systems exhibiting a greater dominance of DM and others displaying a more pronounced stellar component. For example, we see that J0935 is heavily dominated by DM at the Einstein radius, whereas the stellar contribution is markedly more significant in the case of J1020.

The central mass, $m_{\rm cen}$, is consistently subdominant across the sample. While the lens galaxies depicted in the top row of Figure 6.4 (and J1250) exhibit appreciable contributions from this component, with masses of the order $10^{10}\,M_\odot$, it remains a tertiary contributor

[^]Note, however, that the ATLAS^{3D} galaxies overall have lower masses than the galaxies within our sample.

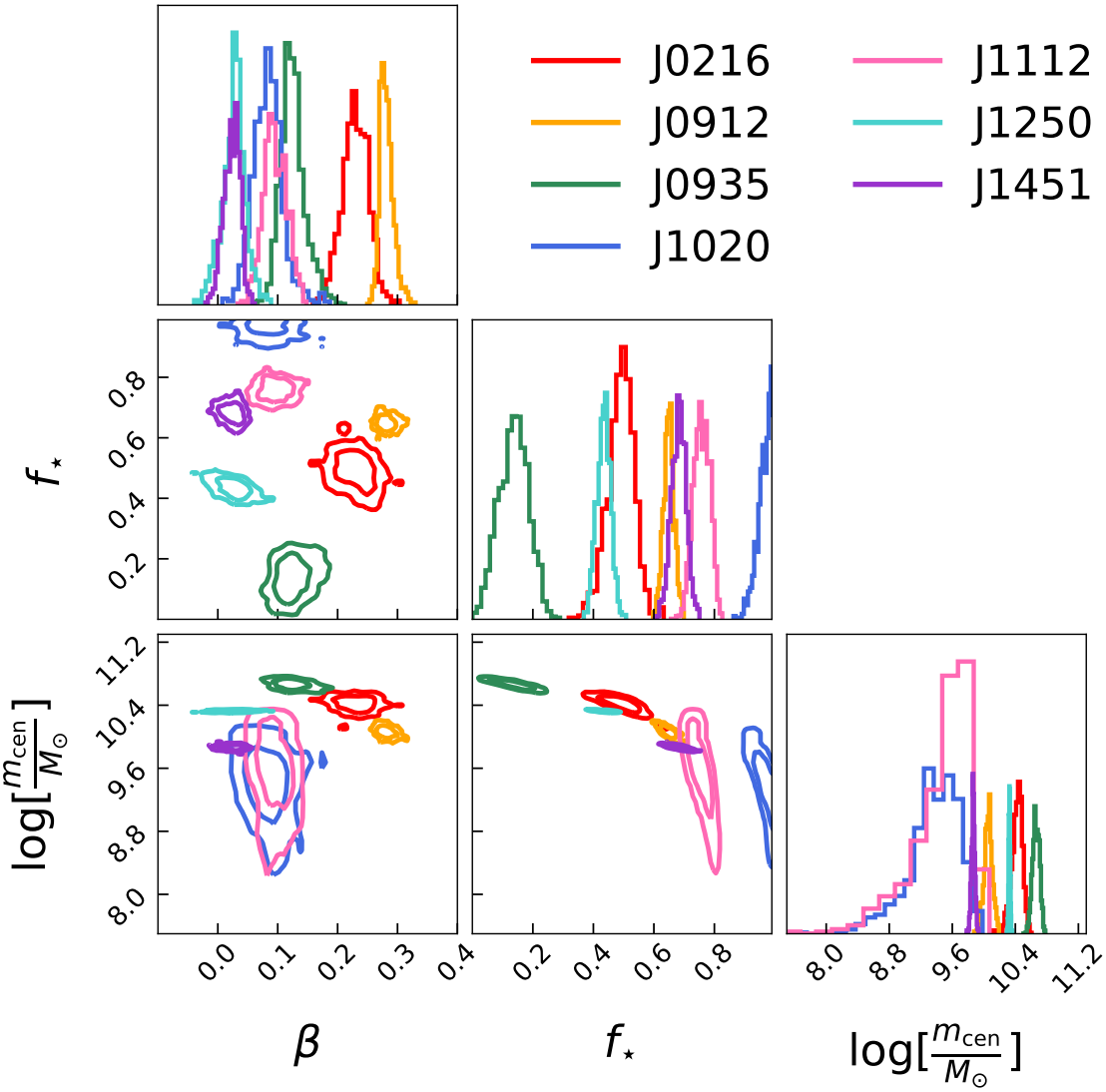

Figure 6.3

The posterior PDF for the model parameters under the assumptions of an NFW-like DM halo and a rigidly enforced lensing mass. The contours show the 68 and 95% confidence regions. The parameters explored are: the orbital anisotropy parameter, β; the stellar mass as a fraction of the total lensing mass, $f_\star$; any central mass in excess of a constant stellar mass-to-light ratio, $m_{\rm cen}$. As the galaxy inclination, i, showed no correlation with any other parameter, it has been omitted from this plot. The diagonal plots show the marginalised posterior densities for each parameter.

to the total mass distribution, functioning as a corrective term to the total mass profile. Given their anomalous positions within the black hole scaling relations (e.g. Gebhardt et al., 2000b; Tremaine et al., 2002; Thomas et al., 2016; van den Bosch, 2016), these masses cannot be solely attributed to BH presence. Instead, we interpret this as being indicative of model flexibility, accommodating excess mass beyond that accounted for by the MGE model. Conversely, lenses J1020, J1112 and J1451 exhibit central masses plausibly indicative of genuine BHs. Given the mass values of less than $10^{10}\,M_{\odot}$, this component exerts a comparatively minor influence within the mass models of these lenses.

Figure 6.4 reveals a near-equal contribution to the total mass profile of J0216 at the Einstein radius from the stellar and dark components. This underscores the well-established characteristic of such elliptical lens systems: the Einstein radius resides within a region where both components exert comparable gravitational influence. This highlights the significant challenges often associated with traditional modelling techniques, as isolating the stellar and dark matter contributions proves to be a complex task.

The interesting cases of J1250 and J1451 exhibit anomalous $m_{\rm cen}$ contributions. As seen in Figure 6.4, the central mass component of both lens galaxies exceeds not only the DM mass in the inner regions but, in the specific instance of J1250, surpasses the stellar mass component as well. This could be attributed either to a systematic limitation within the MGE model, such that the central mass component is forced to compensate for unaccounted-for structural features, or to a more intrinsic property of the stellar population. Specifically, it could be indicative of a modest $\mathrm{M/L}_{\star}$ gradient arising from radial variations in the metallicity distribution. Moreover, the comparatively smaller central mass contribution from the DM component may indicate a cored DM density profile, in a deviation from the standard CDM paradigm (e.g. Davé et al., 2001; Colín et al., 2002; Vogelsberger et al., 2012; Zavala et al., 2013; Kaplinghat et al., 2019; Vogelsberger et al., 2019; Zavala et al., 2019; Nishikawa et al., 2020; Turner et al., 2021, etc.).

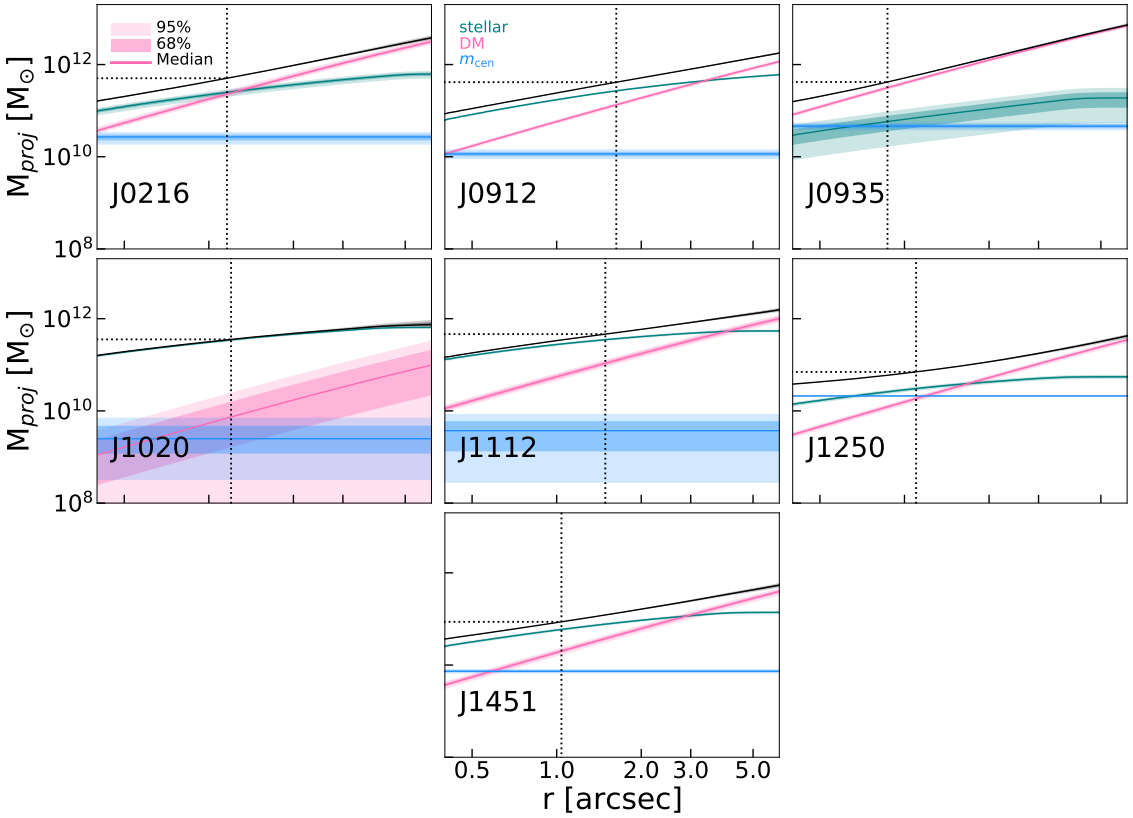

Figure 6.4

The 2D-projected mass profiles for each individual mass component: the stellar (green), DM (pink) and excess central mass (blue) components, as well as the total projected mass profile (black), for each of the lens galaxies in our sample. The vertical and horizontal dotted lines denote the Einstein radius and mass, respectively.

Table 6.1

The median and 68% confidence bounds for the model parameters.

Lens Name	β	$f_\star$	$m_{\rm cen}$ ($10^9 M_\odot$)	i (°)
J0216-0813	$0.23^{+0.02}_{-0.02}$	$0.49^{+0.04}_{-0.05}$	$26.9^{+3.7}_{-4.3}$	85^{+4}_{-4}
J0912+0029	$0.28^{+0.01}_{-0.01}$	$0.65^{+0.02}_{-0.02}$	$11.5^{+1.4}_{-1.3}$	85^{+4}_{-5}
J0935-0003	$0.12^{+0.02}_{-0.02}$	$0.14^{+0.05}_{-0.05}$	$46.0^{+5.1}_{-4.7}$	84^{+5}_{-8}
J1020+1122	$0.08^{+0.02}_{-0.02}$	$0.97^{+0.02}_{-0.03}$	$2.5^{+2.3}_{-1.3}$	82^{+5}_{-7}
J1112+0826	$0.09^{+0.02}_{-0.02}$	$0.76^{+0.03}_{-0.03}$	$3.7^{+2.3}_{-2.4}$	84^{+4}_{-7}
J1250-0135	$0.03^{+0.02}_{-0.02}$	$0.44^{+0.02}_{-0.03}$	$21.1^{+0.5}_{-0.5}$	89^{+1}_{-1}
J1451-0239	$0.02^{+0.01}_{-0.01}$	$0.68^{+0.02}_{-0.03}$	$7.3^{+0.4}_{-0.4}$	84^{+4}_{-5}

6.4 The Lensing Mass as a Free Parameter

We additionally explore models in which the imposed lensing mass is no longer rigidly enforced at the Einstein radius. Instead, it is permitted to vary, scaled by a free parameter, ζ. A significant deviation of ζ from unity might indicate systematic uncertainties in the lens model that the lensing mass derived from, deficiencies in the dynamical model, or, in some cases, limitations imposed by the quality of the available data. This enables us to assess the extent to which our parameter measurements are dependent on the lensing mass, even in the presence of kinematic data, and to verify their consistency.

We repeat our dynamical modelling analysis, now with the freely scaled lensing mass, again maximising the likelihood associated with the observed $v_{\rm rms}$ and sampling the posterior PDF for the model parameters. Figure 6.5 shows the marginalised parameter constraints, which are given in Table 6.2.

Figure 6.5 demonstrates the same ensemble relationship between the stellar mass fraction and the excess central mass parameter seen in Figure 6.3, with $f_\star$ demonstrating an increase with increasing $m_{\rm cen}$. The lens sample in general exhibits a narrower distribution in β values. Furthermore, there is an overall weak trend of the stellar mass fraction of individual lenses increasing with the lensing mass scale parameter. In terms of the individual lens galaxies, three of the seven lenses show no correlation between ζ and $f_\star$, but two show stellar mass fractions that increase with a decreasing lensing mass scale factor.

Most interestingly, the inferred ζ for a significant fraction of lenses is greater than unity at about the 10% level, with an ensemble average across the galaxies of $\zeta = 1.22$ ranging between 1.00 and 1.88[†].

Figure 6.6 presents the 2D-projected mass profiles of the individual mass components for a representative subset of the lens sample. The profiles with a strictly enforced lensing mass, as described in Figure 6.4, are plotted alongside the models with the lensing mass allowed to vary as a free parameter. In the models where the lensing mass is allowed to

[†]The ensemble has an average mass scale parameter of $\zeta = 1.11$ if we exclude the somewhat anomalous value of J1250.

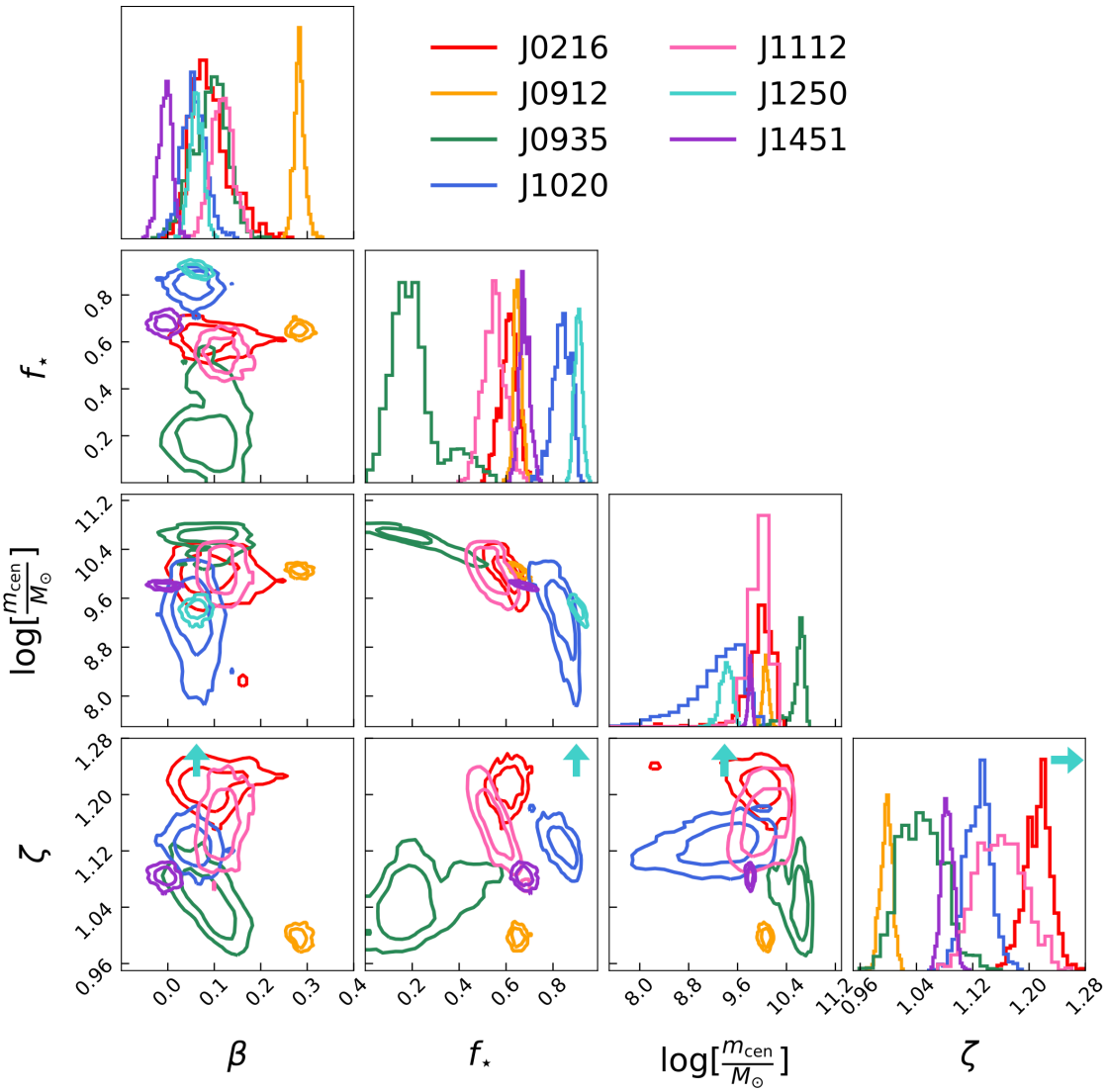

Figure 6.5

The posterior PDF for the model parameters, as described in Figure 6.3, now with the lensing mass as a free parameter. The contours show the 68 and 95% confidence regions. The diagonal plots show the marginalised posterior densities for each parameter. Note that the lensing mass scale, ζ, for J1250 exceeds the axis limits, and as such is denoted by the cyan arrows.

Table 6.2
The median and 68% confidence bounds for the model parameters where the lensing mass is allowed to vary as a free parameter scaled by ζ.

Lens Name	β	$f_\star$	$m_{\rm cen}$ ($10^9 M_\odot$)	i (°)	ζ
J0216-0813	$0.09^{+0.05}_{-0.03}$	$0.61^{+0.03}_{-0.04}$	$9.9^{+4.4}_{-3.7}$	75^{+11}_{-15}	$1.21^{+0.02}_{-0.02}$
J0912+0029	$0.28^{+0.01}_{-0.01}$	$0.65^{+0.02}_{-0.01}$	$11.5^{+1.3}_{-1.2}$	86^{+3}_{-5}	$1.00^{+0.01}_{-0.01}$
J0935-0003	$0.09^{+0.03}_{-0.04}$	$0.19^{+0.10}_{-0.07}$	$41.8^{+6.1}_{-11.2}$	81^{+6}_{-10}	$1.05^{+0.03}_{-0.03}$
J1020+1122	$0.05^{+0.03}_{-0.02}$	$0.84^{+0.04}_{-0.04}$	$2.2^{+2.2}_{-1.5}$	79^{+7}_{-8}	$1.13^{+0.02}_{-0.02}$
J1112+0826	$0.12^{+0.02}_{-0.02}$	$0.55^{+0.05}_{-0.05}$	$9.3^{+3.4}_{-3.0}$	77^{+8}_{-5}	$1.16^{+0.03}_{-0.03}$
J1250-0135	$0.06^{+0.01}_{-0.01}$	$0.91^{+0.02}_{-0.02}$	$2.6^{+0.6}_{-0.6}$	88^{+2}_{-3}	$1.88^{+0.01}_{-0.01}$
J1451-0239	$0.00^{+0.01}_{-0.02}$	$0.68^{+0.02}_{-0.02}$	$6.4^{+0.4}_{-0.5}$	86^{+3}_{-5}	$1.08^{+0.01}_{-0.01}$

vary freely, the models are no longer constrained to intersect the convergence point defined by the Einstein mass and radius characteristic of that specific lens.

In the case of J0912, the lens scaling factor is constrained at unity, i.e. the lensing mass enforced in the analysis described in Section 6.3 is still favoured. Consequently, Figure 6.6 reveals negligible discrepancies between the two scenarios. In contrast, J1020 demonstrates a more intriguing behavior. While the relative contributions of the individual mass components show no radical changes – unlike the effect seen in the case of J1112 – allowing the lensing mass scaling factor to vary freely leads to a substantial tightening of constraints on the DM slope. A similar, albeit less pronounced, effect is observed with the range of $m_{\rm cen}$ values for J1112. This observation is somewhat unexpected, and perhaps counterintuitive, as one might anticipate that rigidly enforcing the total mass profile at the Einstein radius would restrict model flexibility by effectively eliminating certain possibilities in terms of the allowed balance between components. We explore the implications of this unexpected result in Section 7.3.

Figure 6.6 additionally illustrates that for the lens J1112, relaxing the constraint on the lensing mass results in a significant redistribution of the total mass among its constituent components. By allowing the lensing mass to scale freely, the relative contribution of the stellar mass at the Einstein radius decreases from ~ 75 to ~ 50%. This discrepancy

is accounted for by increased contributions from the central excess mass and the DM components.

With J1250, we observe the most pronounced divergence from the lensing mass across the entire sample, characterised by a ζ value of 1.88. Under the freely varying lensing mass, we observe very different relative contributions from all individual mass components when compared to the fixed mass scenario, with the total mass now being dominated by stars. Furthermore, the previously observed parity between DM and excess central mass contributions undergoes a significant shift, resulting in a considerably diminished excess central mass value.

Figure 6.7 shows the posterior PDF of the excess central mass and stellar mass fraction for an illustrative subset of the lens galaxy sample [‡]. As depicted in Figure 6.6, the influence of incorporating a freely scaling lensing mass exhibits considerable variation among different lens systems. While in certain instances (e.g., J0935), the relaxed constraint on the lensing mass results in less stringent bounds on the recovered parameters, in others (e.g., J1112), it can paradoxically yield tighter constraints. Moreover, the flexibility of a free scaling mass can facilitate the recovery of closed inferences in some instances (e.g., J1020), while in others (e.g., J1451), it has a negligible effect on the inferred parameters or their uncertainties.

[‡] Note that this is not the same subset as shown in Figure 6.6.

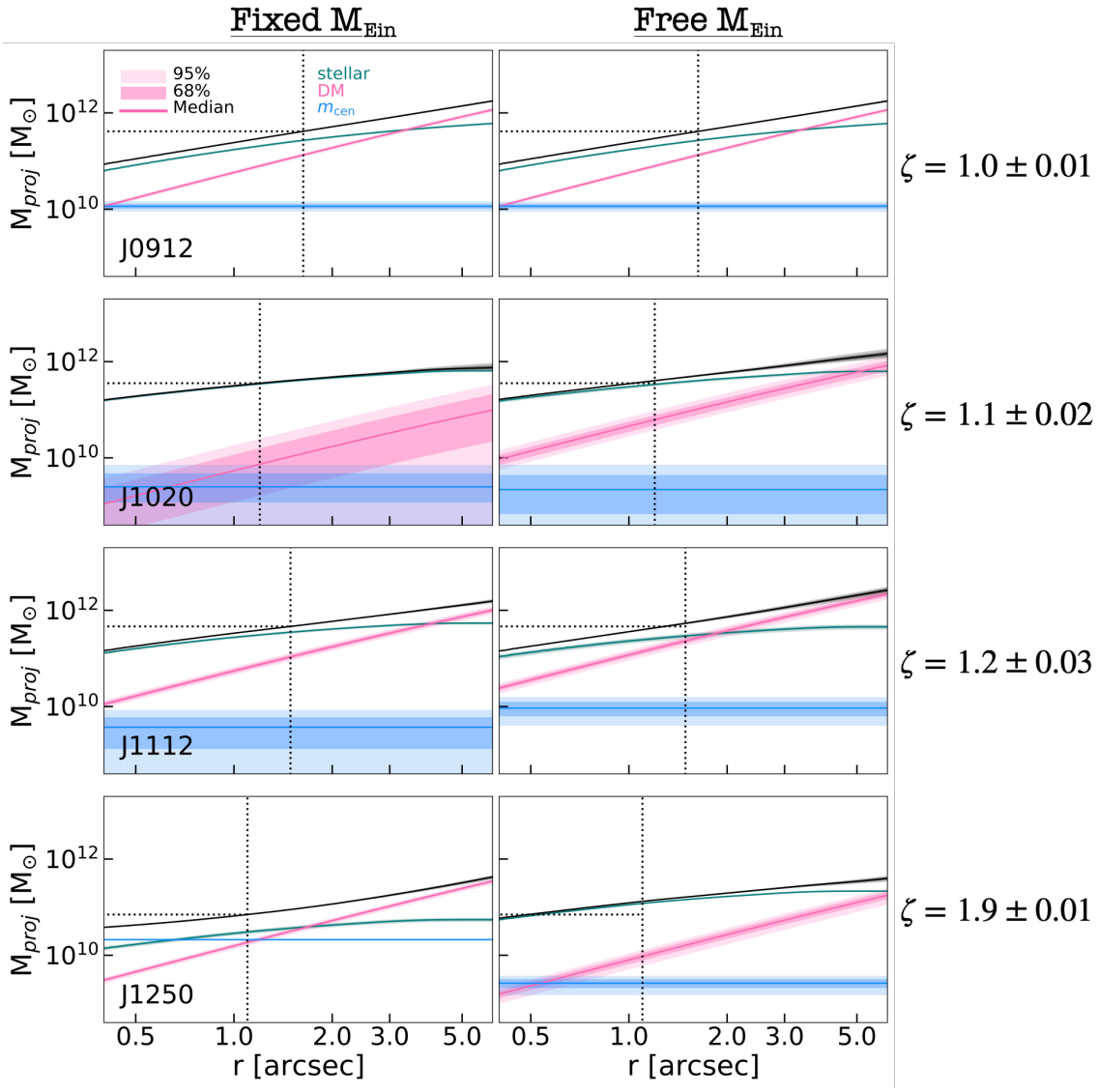

Figure 6.6

The 2D-projected mass profiles of each individual mass component for an illustrative subset of the lens sample. The profiles with a strictly enforced lensing mass, as described in Figure 6.4, are now plotted alongside the models with the lensing mass allowed to vary as a free parameter. The vertical and horizontal dotted lines denote the Einstein radius and mass, respectively.

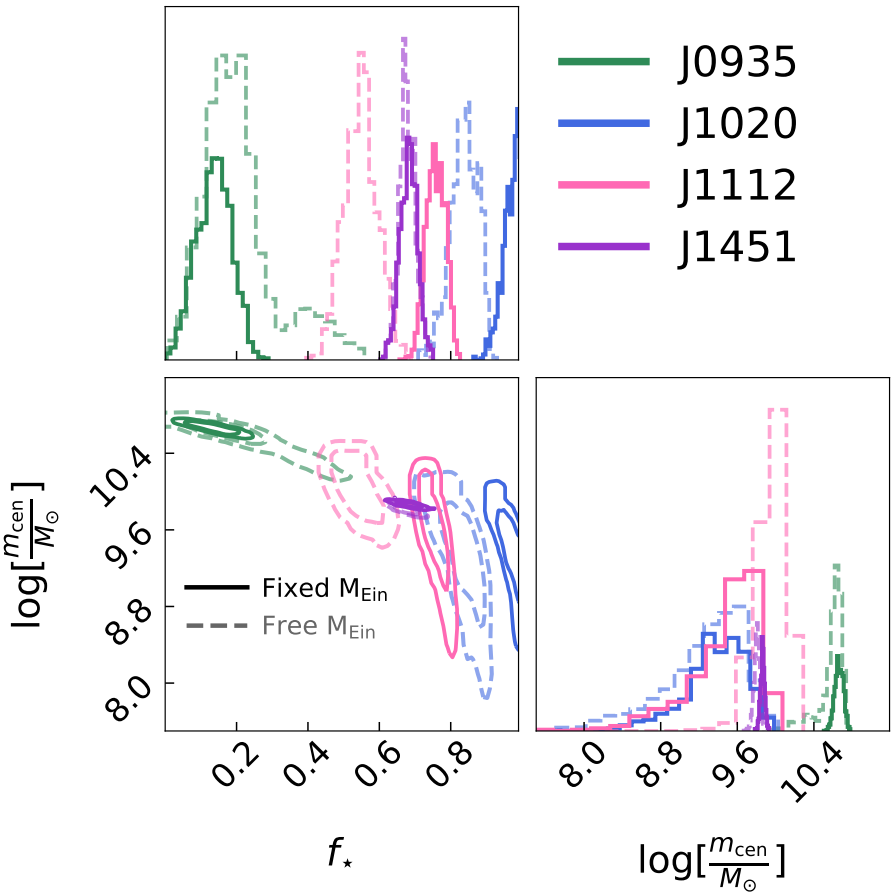

Figure 6.7

The posterior PDF of the excess central mass and stellar mass fraction for an illustrative subset of the lens galaxy sample. The solid line contours denote the models in which the lensing mass is rigidly enforced at the Einstein radius. The dashed contours represent the case in which the lensing mass is scaled by the free parameter ζ.

CHAPTER 7

Discussion

We live in this world in order always to learn industriously and to enlighten each other by means of discussion and to strive vigorously to promote the progress of science and the fine arts

~ **Wolfgang Amadeus Mozart**

7.1 A Near-Isothermal Density Slope for Jackpot

The near isothermal density slope that we have measured for the Jackpot lens is reasonable given previous studies of populations of massive elliptical galaxies. Koopmans et al. (2006); Grillo et al. (2008); Duffy et al. (2010) all found that for the ensemble of lens galaxies, the average total density slope is approximately isothermal.

For the Jackpot specifically, our lensing-equivalent total density-profile slope of $\eta = 0.96 \pm 0.02$ (for the free γ model) is in good agreement with previous measurements of 1.00 ± 0.03, 1.1 ± 0.1, 1.03 ± 0.02, 1.06 ± 0.03 and 1.01 ± 0.18 from Gavazzi et al. (2008), Sonnenfeld et al. (2012), Collett & Auger (2014), Etherington et al. (2022) (lensing only) and Ether-

ington et al. (2023) (lensing + dynamics), respectively [§]. Our model also does an excellent job of predicting the lensing deflection at the location of the second ring, with a deflection angle of 1.89 ± 0.03 arcseconds. This is ~0.2 arcseconds less than the Einstein radius of the second ring, but a slight underestimate is to be expected since our model neglects the presence of mass in the first source. Collett & Auger (2014) inferred an SIS Einstein radius of 0.16 ± 0.02 arcsec for the first source. Adding this to our deflection angle yields a second Einstein radius of 2.05 ± 0.04 arcsec, entirely consistent with the 2.07 ± 0.02 arcsec measured by Gavazzi et al. (2008).

Conversely, our derived total density slope is inconsistent with that from the Minor et al. (2021) study, who find a surprisingly steep density slope of $\eta = 1.32 \pm 0.04$ from lensing alone. The paper reports a correlation between the derived density slope and the inferred subhalo mass; thus, a shallower lens slope would have implications for the claim of an unusually dense and massive halo. Their footnote 2 cites, however, a fairly modest decrease of 25% in subhalo mass if the slope was confirmed to be approximately isothermal.

Additionally, we infer a DM density slope of $1.73^{+0.17}_{-0.26}$ which is significantly steeper than an unmodified NFW profile (i.e. $\gamma = 1$), but sits in good agreement with the lensing + dynamics DM profile slope of 1.7 ± 0.2 found for this galaxy by Sonnenfeld et al. (2012).

7.2 Is the Standard Approach to Lens Modelling Too Simple?

When drawing comparisons between dynamical and pure lensing studies, it is important to note the contrast in (and limitations of) the methods used. In dynamical analyses, restrictive assumptions are often made on the lens galaxy axisymmetry and orbital structure; pure lensing studies typically assume simple power laws and a simplified linear external shear.

[§] We do, however, note here that the Gavazzi et al. (2008) and Sonnenfeld et al. (2012) slopes are derived from a measure of the average slope between the two Einstein rings, not at the location of the first ring as is done in our analysis, and the Collett & Auger (2014) constraint also includes the power-law slope's effect on the light profile of the second ring. Additionally, the lensing + dynamics approach in Etherington et al. (2023) differs from that described in Chapter 5 as the dynamical measurements are derived from fibre-based optical spectroscopy from the SDSS.

As shown in our study of the Jackpot lens, and also found in Etherington et al. (2023), lensing-only studies appear to predict marginally steeper projected density slopes than combined lensing + dynamics studies do. If the observed discrepancies stem from a lack of complexity in the dynamical modelling, one would expect that as you relax the simplifications and introduce spatially resolved structure, the recovered slopes from the two methods should be in closer agreement. As we have shown, this is not the case, with our reported projected density slope showing less consistency with pure lensing slopes than that of the lensing + dynamics measurement from Etherington et al. (2023)'s one-aperture kinematics. Instead, we consider the possibility that the disparity arises from either deficiencies in the lens modelling, or more subtle limitations in the kinematics that can only be solved through more sophisticated dynamical modelling techniques such as Schwarzschild models (Schwarzschild, 1979).

The analysis presented in Chapter 6 further underscores the limitations and oversimplifications inherent in the assumptions underpinning simple parameterised lens modelling analyses. Despite the kinematic properties of our sample being strongly dominated by pressure support, with $v_{\rm rot}^2 \ll \sigma^2$ in all cases, we find pronounced rotational characteristics in a substantial fraction of our lens galaxy sample.

It has formed the basis of numerous studies based on SLACS lensing data that massive ETGS are well-approximated by elliptical mass distributions, e.g. the singular isothermal ellipsoid (SIE) profile commonly used in lens modelling (e.g. Bolton et al., 2006; Koopmans et al., 2006; Treu et al., 2006). This conclusion was based on the agreement between the velocity dispersion profile predicted by the SIE fit and the observed profile. However, this equivalence only holds under the assumption of isotropy.

If our results are representative of the broader population of massive ETG lenses, it could have profound implications for their evolutionary pathways and stellar populations. The SIE profiles used in the simplest lensing models will not reproduce the "diskiness" in the lenses that our rotation implies might be present.

Moreover, our analysis of the lens sample hints at the presence of even more complex structures in certain cases. For example, the detection of a kinematically distinct core

in J1250, characterised by two counter-rotating components, provides support for the likely presence of angular substructures within the foreground deflector. The analysis of J1250 could be indicative of underlying triaxiality, a complexity precluded by the inherent constraints of the axisymmetric modelling framework adopted in this thesis. In a generalised triaxial configuration, the absence of conserved angular momentum leads to a profound alteration of orbital characteristics, permitting orbits with initial non-zero angular momentum to exhibit non-uniform rotational behaviour. The inherent limitations of our simplified dynamical models could, in principle, be addressed through the application of more generalised frameworks, such as orbit-based models (e.g. Schwarzschild, 1979), by permitting orbits with greater radial and angular momentum freedom. This would allow, for example, orbits that oscillate between clockwise and counter-clockwise rotation, or that approach the centre of the system, effectively negating the angular momentum barrier that restricts orbits within axisymmetric potentials. However, such an approach would necessitate a substantial augmentation of data quality. Specifically, the requisite signal-to-noise ratio, currently unattainable with our observational constraints, would be paramount.

7.3 The Lensing Mass Scaling Parameter

In Chapter 6, we explored models where the lensing mass is allowed to vary, scaled by a free parameter, ζ. Interestingly, the inferred ζ for a significant fraction of lenses is greater than unity at about the 10% level, with a range across the sample of between 1.00 and 1.88.

Such a deviation from the lensing might indicate systematic uncertainties in the lens model that the lensing mass derived from, deficiencies in the dynamical model, or, in some cases, limitations imposed by the quality of the available data. With the exception of J1250, with its complex spiral source, it is unlikely that the lens modelling would be sensitive to more uncertainty than the few % lensing mass errors that are expected, thereby biasing the inferred lensing mass. In the case of J1250, the presence of spiral arms has historically hindered any accurate lensing analysis, owing to the necessity of disentangling the intricate

light contributions from these arms and the superimposed Einstein ring. Such a task has remained intractable within the confines of imaging-only analyses.

In instances where data quality is compromised, for example with a lower S/N ratio or reduced exposure time, the validity of the dynamical model should be subject to scrutiny. Discrepancies between the lensing mass and the dynamical model predictions may indicate either deficiencies in the dynamical model itself or fundamental limitations imposed by insufficient data.

This additional degree of freedom in the total mass profile introduces a diverse range of behaviors among the lens sample. Some lenses respond to the freely varying lensing mass by demonstrating tighter parameter constraints, some by demonstrating weaker constraints, and some remain largely impervious to the introduced variability. This observation is somewhat unexpected, and perhaps counterintuitive, as one might anticipate that rigidly enforcing the total mass profile at the Einstein radius would restrict model flexibility by effectively eliminating certain possibilities in terms of the allowed balance between components. It is anticipated that by supplementing the kinematic data with additional mass information at the Einstein radius, the uncertainty associated with the model parameters should decrease. Instead, if our comprehension of the lens galaxy requires some refinement – for example if our assumption of an axisymmetric galaxy model is incorrect, or we do not have a good understanding of the lensing – then the addition of more data can lead to an inconsistency. In such a scenario, while lensing might have provided us with some new insight, the precise interpretation of that insight remains ambiguous.

Furthermore, the observed range of behaviors, and the limited success of strictly enforcing a lensing mass in refining parameter constraints, suggests that kinematic measurements alone are sufficiently robust to overshadow the incremental benefits provided by a lensing aperture mass. This is not to diminish the value of lensing entirely – by identifying the discrepant cases as above, lensing does provide value at least as a validity check – but rather to underscore the exceptional power of kinematic measurements and dynamical modelling in an analysis such as this one.

7.4 Robustness of Assumptions

As noted in Section 5.3, there exists a possible degeneracy between the models that maximise the likelihood in the inner and outer regions of the galaxy. For the Jackpot galaxy, there seems present an orthogonal angular dependence at large radii, such that we see a relatively high velocity dispersion along the major axis (the kinematic minor axis), but conversely a significantly lower velocity dispersion along the minor axis, corresponding to the regions with the largest measured rotation. This is particularly evident in the velocity dispersion panel of Figure 5.1, where we suspect that this behaviour may be related to a greater influence from DM at this radii.

Given the apparent non-axisymmetry implied by the low surface-brightness envelope at large radii, and the possible signatures for past interactions (as speculated by Sonnenfeld et al., 2012), we excluded measurements from the nine Voronoi bins at $r \gtrsim 2$ arcsec from our preferred modelling. If we instead fit to the full, unrestricted range of data, we recover a resulting projected density slope of $\eta = 1.042 \pm 0.02$, which sits in slightly closer agreement with the lensing only studies, but the model now provides a poorer fit to the kinematics, especially in the outer regions.

The kinematics in non-axisymmetric mass distributions can, in principle, be tackled using more general dynamical models, such as the orbit-based approach of Schwarzschild (1979) (e.g. see Poci & Smith, 2022). This approach would perhaps mitigate the limitations imposed by our simple model, but would in turn demand much more stringent requirements on the data with a necessity for a very high signal-to-noise ratio that is unfeasible with the present observations. This is especially true when dealing with the pervasive contamination of source light at the first Einstein radius.

7.5 Central Mass in Excess of a Constant Mass-to-Light Ratio

In the construction of all of our dynamical models, we allow for an additional compact mass, that is not described by the luminosity distribution or the NFW profile, and use this to describe any excess central mass. We find that the preferred excess central mass of our full sample (the lens galaxies described in Chapter 6 and the Jackpot lens) under the assumption of a fixed NFW profile has a mean value of $\langle\, m_{\rm cen}\,\rangle \approx 15.8 \times 10^9\,{\rm M}_\odot$, within a range of $2 \lesssim \langle\, m_{\rm cen}[\times 10^9 {\rm M}_\odot]\,\rangle \lesssim 46$. In addition, our free γ model of the Jackpot lens is well constrained to be $\sim 8.23 \times 10^9\,{\rm M}_\odot$. If attributed to a central black hole only, these findings would posit outliers relative to black hole scaling relations (e.g. Gebhardt et al., 2000b; Tremaine et al., 2002; Thomas et al., 2016; van den Bosch, 2016). Given the $M_{\rm BH} - \sigma$ relation derived by van den Bosch (2016), for a mean central velocity dispersion for the sample of $\sim 290\,{\rm km\,s^{-1}}$, it is expected that the true BH contribution to the central mass component will be less than $\sim 10^9 {\rm M}_\odot$. Although the form of the scaling relations at the highest masses is still uncertain (e.g. Thomas et al., 2016), it is unlikely that any lens in our sample truly harbours a $\sim 10^{10}\,M_\odot$ black hole.

A more plausible explanation is that in our analyses we assume a constant $M/L_\star$ but, whilst we do not expect variations in age in galaxies of this type, there may be a metallicity gradient present, leading to a modest M/L$_\star$ gradient such as described by Tortora et al. (2010). Moreover, if there is a radial gradient in the stellar initial mass function as reported by Martín-Navarro et al. (2015); La Barbera et al. (2017); van Dokkum et al. (2017) (but see Alton et al., 2017; Vaughan et al., 2018), then a much more substantial $M/L_\star$ gradient may be present, and indeed Collett et al. (2018) saw exactly this for a nearby lens. These works would suggest a steep increase in mass within $\lesssim$1 kpc. Whilst we expect that our I-band images would provide faithful tracers of the stellar mass profile for a modest age and metalicity variation, this might not be true in the case of radial IMF variation; however, such a gradient should be absorbed into our central mass component, to first order, at the

resolution of the present data.

The exquisite spatial resolution achievable with the MUSE Narrow Field Mode (NFM), with its PSF (with ~0.06 arcsec FWHM core) and fine pixel scale (0.025 arcsec), could provide the fine spatial sampling required to obtain more meaningful constraints on the excess central mass component. If indeed a more substantial $M/L_\star$ gradient is present than our current models account for, then MUSE NFM data would certainly be more sensitive to the characteristic increase in mass within $\lesssim$1 kpc ($\sim$ 0.27 arcsec at $z = 0.222$ for the Jackpot) than our present WFM data is. However, for a fraction of the galaxies in our sample, with the NFM FoV of 7.42×7.43 arcsec, this would come at the expense of full area coverage. In addition to this, the incorporation of stellar population modelling to fix, or at least constrain, $M/L_\star$ represents a valuable direction for future inquiry.

In Appendix A we show that tests with synthetic MUSE data suggest a potential for overestimation of the central mass. In the absence of a central mass in the input data, a mass comparable to that predicted by the standard $M_{\rm BH} - \sigma$ relation for a Jackpot-like galaxy was recovered. However, this is an order of magnitude smaller than the excess central mass recovered from the real data.

CHAPTER 8

Conclusions & Future Work

"I conclude that all is well," says Oedipus

~ Albert Camus

We have presented results from a comprehensive kinematic and dynamical analysis of the 'Jackpot' (SDSS J0946+1006) $z = 0.222$ lens galaxy. This work marks the first 2D spatially resolved kinematic study of the system, leveraging new, deep MUSE integral field spectroscopic data obtained through a dedicated 5-hour integration, in order to constrain the 2D-projected total mass profile slope. The Jackpot stands as the most extensively studied example (see Vegetti et al., 2010; Sonnenfeld et al., 2012; Collett & Auger, 2014; Smith & Collett, 2021; Etherington et al., 2022, etc.) of a multiple-source-plane lens (MSPL), or compound lens, a rare and valuable type of gravitational lens system occurring when a single foreground lens galaxy simultaneously multiply-images two or more background source galaxies at different redshifts.

To account for contamination from the source galaxy light, we implemented a multiple component fitting technique, adapted from the PPXF code (Cappellari & Emsellem, 2004; Cappellari, 2017), to extract the lens galaxy kinematics to first and second order. Simple gNFW + stars dynamical models were constructed with parameterised orbital anisotropies,

DM density power-law slopes, stellar mass fractions and excess central mass components, and a robustly constrained aperture lensing mass was imposed. The posterior PDF for the model parameters was sampled, and a chi-squared likelihood maximised to derive the projected total density slope.

We measure rotation about the minor axis of $v \approx \pm 100\,\mathrm{km\,s^{-1}}$ and a steep decrease in velocity dispersion from a central value of $\sigma \approx 290\,\mathrm{km\,s^{-1}}$ to $\sigma \approx 200\,\mathrm{km\,s^{-1}}$ in the outer regions. Notwithstanding the strong presence of rotation, the galaxy is dispersion-dominated at all radii. The kinematic measurements are consistent with those of previous single-slit studies of the Jackpot lens (i.e. central velocity dispersions of $\sigma_{\mathrm{sonn12}} = 287 \pm 11\,\mathrm{km\,s^{-1}}$ and $\sigma_{\mathrm{spin15}} = 300 \pm 22\,\mathrm{km\,s^{-1}}$), but are now fully mapped out in two-dimensions.

From the JAM dynamical modelling, we infer a mass budget inside the Einstein radius that is dominated by stars (∼70 %) if the halo slope is fixed to the NFW shape. For modified halos, we infer a larger DM fraction, and a DM density slope of $\gamma = 1.73^{+0.17}_{-0.26}$, which deviates significantly from the canonical NFW profile (i.e. $\gamma = 1$). This steeper slope is in agreement with previous results for both the Jackpot itself (Sonnenfeld et al., 2012) and some ensemble studies of lens galaxies (e.g. Grillo, 2012). These results ostensibly support the scenario in which DM haloes contract in response to the presence of a significant baryonic component. However, contrasting studies suggest that unmodified NFW profiles may be statistically favored instead (e.g. Shajib et al., 2021).

Our fitted models yield a 2D-projected total mass profile slope for the Jackpot lens of 1.03 ± 0.03, and a lensing-equivalent projected logarithmic density profile slope of $\eta = 0.96 \pm 0.02$. Thus we confirm most-pure lensing results in finding a near isothermal profile (e.g. Collett & Auger, 2014; Etherington et al., 2022). Our profile is inconsistent with the surprisingly steep slope measurement of Minor et al. (2021).

The main goal of this work, and of ongoing extensions relating to the Jackpot, is to suppress the remaining systematic errors and degeneracies, so as to fully exploit the cosmological potential offered by this unique lens system. An improved analysis of the lensing properties, exploiting multi-band imaging for all three sources, is presented by Ballard et al. (2024).

Future extensions to our work will incorporate the measured kinematics simultaneously with the lensing information, to create an even more detailed picture of the Jackpot system.

Additionally, having obtained spatially-resolved, high sensitivity, high resolution MUSE data for a larger sample of lens galaxies, we have generalised the analytical techniques developed in the study of the Jackpot lens and applied them to a broader sample of 9 additional SLACS early-type lens galaxies. The gravitational lens systems within our sample span a lens and source redshift range of $0.087 \leq z_{\rm lens} \leq 0.347$ and $0.324 \leq z_{\rm source} \leq 0.630$ respectively. This broader analysis yields a robust determination of the first and second moments of the two-dimensional stellar kinematics for the entire sample, which we map out in 2-dimensions, and we constrain a mean velocity dispersion for the sample of $\sim 290\,{\rm km\,s^{-1}}$.

Among the galaxies in this sample, J1250-0135 is a particularly noteworthy case. Previously excluded from sample studies due to the presence of bright spiral arms, which significantly hinder any accurate lensing analysis, this complex lens system now benefits from the wealth of information provided by MUSE IFU data. The intricate structured light is definitively confirmed to be at the redshift of the background source, allowing the 2D stellar kinematics of the foreground elliptical lens galaxy to be measured for the first time.

We again employ the anisotropic Jeans modelling framework and sample the posterior PDF for the model parameters under the assumptions of an NFW-like DM halo and a rigidly enforced lensing mass at the Einstein radius. We find that, although the fitted orbital anisotropy, β, exhibits considerable scatter among individual galaxies, the ensemble average across the galaxies converges at $\langle\,\beta\,\rangle = 0.12$, with a bounded range of 0.02 to $0.02 \leq \langle\,\beta\,\rangle \leq 0.28$. Whilst the original SLACS analysis assumed isotropic orbits, the anisotropy range that we find is consistent with that of the ATLAS$^{\rm 3D}$ survey (Cappellari et al., 2013). The inferred stellar mass fraction, $f_\star$, spans a wide range of $0.14 \leq \langle\,f_\star\,\rangle \leq 0.97$, with evidence of intrinsic scatter from the individual galaxies typically below the 10% level. A mean value for the sample of $\langle\,f_\star\,\rangle = 0.59$ was found.

We additionally explore models in which the imposed lensing mass is no longer rigidly enforced at the Einstein radius. Instead, it is permitted to vary, scaled by a free parameter,

ζ. The inferred ζ for a significant fraction of lenses in our sample is greater than unity at about the 10% level, with an ensemble average across the galaxies of $\zeta = 1.22$ ranging between 1.00 and 1.88. A significant deviation of ζ from unity might indicate systematic uncertainties in the lensing or dynamical model, or limitations imposed by the quality of the available data. Thus, we discuss the implications of this finding and comment on possible deficiencies in the modelling techniques commonly used for analysing early-type lens galaxies.

8.1 Future Work

The analytical techniques presented in this thesis, when applied to a large sample of lens galaxies, offer the potential to provide key insights into the fundamental properties of ETGs. This is owing to the fact that our sub-sample of SLACS lenses is anticipated to be representative of the broader population of massive ETGs within the Sloan Digital Sky Survey. Moreover, the conclusions drawn from our analysis are expected to be applicable to a wider range of lensing systems with more high-level lensing and cosmology science objectives, including time-delay lenses and those with identified substructures. By refining the lens macro model, we can establish reliable priors for subsequent, more advanced lensing investigations involving targets with limited observational data, such as faint quasar lenses.

The discussions presented here underscore the limitations of current lens modelling techniques, particularly in their reliance on oversimplified assumptions regarding lens galaxy axisymmetry and orbital structure. Our findings suggest that the SIE profile, a common assumption in simple lens models of SLACS lenses, may not accurately represent the properties of real early-type lens galaxies. We also identify potential systematic limitations in the simple anisotropic dynamical Jeans models employed in our work and numerous other similar studies. These insights may hint at a need to reevaluate our approach to modelling early-type lens galaxies in favour of more sophisticated models that can better capture the complex dynamics and morphologies of lensing objects. The

kinematics in non-axisymmetric mass distributions can, in principle, be tackled using more general dynamical models, such as orbit-based models. This approach would perhaps mitigate the limitations imposed by the simple Jeans models, but would in turn demand much more stringent requirements on the data with a necessity for a very high S/N ratio that is unfeasible with the present observations.

In the work presented in this thesis, we show that one of the most promising and robust methods of determining the mass density distribution of ETGs, and further gaining key inferences on the internal structure and dynamics of them, is the powerful combination of gravitational lensing and stellar dynamics. The sensitivity of each individual probe to different mass scales allows for tremendous constraining power and the ability to disentangle the stellar and the DM mass contributions of lens galaxies at their characteristic radii, thus breaking the degeneracies between these two components. However, in order to fully exploit the additional advantages that kinematic data can bring to breaking degeneracies, it is critical that IFU data with good spatial and angular resolution are obtained. In spite of this, the current sample of lens galaxies with deep, spatially resolved IFU data is relatively small. As a result, the existing sample is biased by the research objectives of individual proposals and is not well-suited for statistical analysis. The current lack of a large, compelling sample hinders our ability to conduct comprehensive studies and draw definitive conclusions about these objects.

As such, future work will expand the current sample of spatially resolved, deep IFU spectroscopic data of lens galaxies, for example using the MUSE instrument on the VLT. The scientific exploitation of such a sample would be significant and wide-ranging, but fundamentally would enable a self-consistent combination of the constraints from both gravitational lensing and stellar kinematics in order to perform a detailed investigation of – and place robust, statistical constraints on – the intrinsic properties of galaxies and the nature of DM.

In addition, this project would provide an excellent test of alternative DM candidates. The Jackpot system, as studied in detail in this thesis, hosts one of only a few cases of a dark substructure detected through lensing perturbations. The substructure is cited as having a

mass high enough that one would expect it to host a luminous galaxy, as well as having a surprisingly high central density. The peculiar inferred properties of the subhalo may be a signature of a deviation from the CDM paradigm with respect to the particle physics of DM, such as dark matter self-interactions. In this case, one would expect to detect more highly concentrated substructures in a sample such as this.

A project such as this would be both timely and relevant. It offers a wealth of scientific outputs, both in terms of ensemble measurements of intrinsic galaxy properties and individual studies of compelling lenses, but also addresses the clear need for a larger sample of spatially resolved, deep IFU spectroscopic data for lens galaxies. Furthermore, the results of such an analysis would be aptly timed to inform a future ESO ELT Large Program proposal to further extend the observations and obtain a cosmologically powerful sample of lenses alongside the recovery of measurements of the ensemble properties of a large catalogue of lens galaxies.

The work described in this thesis has so far explored the two extremes in terms of constraining the lensing mass – it is either rigidly enforced or allowed to vary freely. While the former provides a simplified baseline, it is inherently not valid as the measurements of the lensing mass are subject to some systematic uncertainties, albeit relatively small ones. Future work will readdress the interesting behaviour observed when relaxing the constraints on the lensing mass, and the resulting redistribution of the total mass among its constituent components demonstrated by some lenses in the sample, by modelling the lensing mass with a Gaussian prior. Given the somewhat modest effect that this seems to have had on our small lens sample, incorporating an error at about the 10% level would likely not yield significant changes. However, such a modification would enable us to explore the boundaries of reasonable assumptions regarding the lensing mass.

Bibliography

Alatalo K., et al., 2011, , 735, 88

Alton P. D., Smith R. J., Lucey J. R., 2017, , 468, 1594

Amvrosiadis A., et al., 2024, arXiv e-prints, p. arXiv:2407.12983

Anderson L., et al., 2014, , 441, 24

Arimoto N., Yoshii Y., 1987, , 173, 23

Arsenault R., et al., 2008, in Hubin N., Max C. E., Wizinowich P. L., eds, Society of Photo-Optical Instrumentation Engineers (SPIE) Conference Series Vol. 7015, Adaptive Optics Systems. p. 701524, doi:10.1117/12.790359

Auger M. W., Treu T., Bolton A. S., Gavazzi R., Koopmans L. V. E., Marshall P. J., Bundy K., Moustakas L. A., 2009, , 705, 1099

Auger M. W., Treu T., Gavazzi R., Bolton A. S., Koopmans L. V. E., Marshall P. J., 2010a, , 721, L163

Auger M. W., Treu T., Bolton A. S., Gavazzi R., Koopmans L. V. E., Marshall P. J., Moustakas L. A., Burles S., 2010b, , 724, 511

Babcock H. W., 1953, , 65, 229

Bacon R., et al., 1995, , 113, 347

Bacon R., et al., 2001, , 326, 23

Bacon R., et al., 2010, in McLean I. S., Ramsay S. K., Takami H., eds, Society of Photo-Optical Instrumentation Engineers (SPIE) Conference Series Vol. 7735, Ground-based and Airborne Instrumentation for Astronomy III. p. 773508 (arXiv:2211.16795), doi:10.1117/12.856027

Balcells M., 1991, , 249, L9

Baldry I. K., 2008, Astronomy and Geophysics, 49, 5.25

Ballard D. J., Enzi W. J. R., Collett T. E., Turner H. C., Smith R. J., 2024, , 528, 7564

Barnabè M., Koopmans L. V. E., 2007, , 666, 726

Barnabè M., Czoske O., Koopmans L. V. E., Treu T., Bolton A. S., Gavazzi R., 2009, , 399, 21

Barnabè M., Czoske O., Koopmans L. V. E., Treu T., Bolton A. S., 2011, , 415, 2215

Barnabè M., et al., 2012, , 423, 1073

Bender R., 1990, , 229, 441

Bender R., Moellenhoff C., 1987, , 177, 71

Bender R., Surma P., 1992, , 258, 250

Bender R., Doebereiner S., Moellenhoff C., 1988, , 74, 385

Bender R., Saglia R. P., Gerhard O. E., 1994, , 269, 785

Benson A. J., et al., 2013, , 428, 1774

Bernardi M., Shankar F., Hyde J. B., Mei S., Marulli F., Sheth R. K., 2010, , 404, 2087

Bertin G., et al., 1994, , 292, 381

Bertola F., Capaccioli M., 1975, , 200, 439

Binney J., Mamon G. A., 1982, , 200, 361

Binney J., Tremaine S., 1988, Galactic Dynamics

Birrer S., Treu T., 2021, , 649, A61

Birrer S., et al., 2019, , 484, 4726

Birrer S., et al., 2020, , 643, A165

Blumenthal G. R., Faber S. M., Flores R., Primack J. R., 1986, , 301, 27

Bolton A. S., Burles S., Koopmans L. V. E., Treu T., Moustakas L. A., 2006, , 638, 703

Bolton A. S., Burles S., Koopmans L. V. E., Treu T., Gavazzi R., Moustakas L. A., Wayth R., Schlegel D. J., 2008a, , 682, 964

Bolton A. S., Treu T., Koopmans L. V. E., Gavazzi R., Moustakas L. A., Burles S., Schlegel D. J., Wayth R., 2008b, , 684, 248

Bolton A. S., et al., 2012, , 757, 82

Bullock J. S., Boylan-Kolchin M., 2017, , 55, 343

Bundy K., et al., 2015, , 798, 7

Burkert A., Naab T., Johansson P. H., Jesseit R., 2008, , 685, 897

Caon N., Capaccioli M., D'Onofrio M., 1993, , 265, 1013

Cappellari M., 2002, , 333, 400

Cappellari M., 2008, , 390, 71

Cappellari M., 2012, arXiv e-prints, p. arXiv:1211.7009

Cappellari M., 2016, , 54, 597

Cappellari M., 2017, , 466, 798

Cappellari M., Copin Y., 2003, , 342, 345

Cappellari M., Emsellem E., 2004, , 116, 138

Cappellari M., et al., 2006, , 366, 1126

Cappellari M., et al., 2007, , 379, 418

Cappellari M., et al., 2011, , 413, 813

Cappellari M., et al., 2013, , 432, 1709

Carollo C. M., de Zeeuw P. T., van der Marel R. P., Danziger I. J., Qian E. E., 1995, , 441, L25

Carr B. J., Rees M. J., 1984, , 206, 801

Chang L. J., Necib L., 2021, , 507, 4715

Cohen J. S., Fassnacht C. D., O'Riordan C. M., Vegetti S., 2024, , 531, 3431

Cole S., Aragon-Salamanca A., Frenk C. S., Navarro J. F., Zepf S. E., 1994, , 271, 781

Colín P., Avila-Reese V., Valenzuela O., Firmani C., 2002, , 581, 777

Collett T. E., 2014, PhD thesis, University of Cambridge, UK

Collett T. E., Auger M. W., 2014, , 443, 969

Collett T. E., Smith R. J., 2020, , 497, 1654

Collett T. E., et al., 2018, Science, 360, 1342

Courteau S., et al., 2014, Reviews of Modern Physics, 86, 47

Courtes G., 1982, in Humphries C. M., ed., Astrophysics and Space Science Library Vol. 92, IAU Colloq. 67: Instrumentation for Astronomy with Large Optical Telescopes. p. 123, doi:10.1007/978-94-009-7787-7_16

Cox T. J., Dutta S. N., Di Matteo T., Hernquist L., Hopkins P. F., Robertson B., Springel V., 2006, , 650, 791

Cretton N., van den Bosch F. C., 1999, , 514, 704

Daddi E., et al., 2005, , 626, 680

Davé R., Spergel D. N., Steinhardt P. J., Wandelt B. D., 2001, , 547, 574

Davies R., Kasper M., 2012, , 50, 305

Davies R. L., Efstathiou G., Fall S. M., Illingworth G., Schechter P. L., 1983, , 266, 41

Davies R. L., Sadler E. M., Peletier R. F., 1993, , 262, 650

Davis M., Efstathiou G., Frenk C. S., White S. D. M., 1985, , 292, 371

Djorgovski S., Davis M., 1987, , 313, 59

Doppler C., 1842, Über das farbige Licht der Doppelsterne und einiger anderer Gestirne des Himmels

Dressler A., 1980, , 236, 351

Duffy A. R., Schaye J., Kay S. T., Dalla Vecchia C., Battye R. A., Booth C. M., 2010, , 405, 2161

Dutton A. A., Treu T., 2014, , 438, 3594

Dutton A. A., van den Bosch F. C., Dekel A., Courteau S., 2007, , 654, 27

Dye S., Warren S. J., 2005, , 623, 31

Dyson F. W., Eddington A. S., Davidson C., 1920, Philosophical Transactions of the Royal Society of London Series A, 220, 291

Efstathiou G., 2024, arXiv e-prints, p. arXiv:2406.12106

Einasto J., Kaasik A., Saar E., 1974, , 250, 309

Einstein A., 1915, Sitzungsberichte der Königlich Preussischen Akademie der Wis-

senschaften, pp 844–847

Emsellem E., Monnet G., Bacon R., 1994, , 285, 723

Esposito S., et al., 2010, in Ellerbroek B. L., Hart M., Hubin N., Wizinowich P. L., eds, Society of Photo-Optical Instrumentation Engineers (SPIE) Conference Series Vol. 7736, Adaptive Optics Systems II. p. 773609, doi:10.1117/12.858194

Etherington A., et al., 2022, , 517, 3275

Etherington A., et al., 2023, , 521, 6005

Faber S. M., Jackson R. E., 1976, , 204, 668

Falco E. E., Gorenstein M. V., Shapiro I. I., 1985, , 289, L1

Farouki R. T., Shapiro S. L., 1982, , 259, 103

Ferreras I., Saha P., Leier D., Courbin F., Falco E. E., 2010, , 409, L30

Foreman-Mackey D., Hogg D. W., Lang D., Goodman J., 2013, , 125, 306

Fukugita M., et al., 2007, , 134, 579

Fusco T., Conan J.-M., Rousset G., Mugnier L. M., Michau V., 2001, Journal of the Optical Society of America A, 18, 2527

Garrett M. A., Calder R. J., Porcas R. W., King L. J., Walsh D., Wilkinson P. N., 1994, , 270, 457

Gavazzi R., Treu T., Rhodes J. D., Koopmans L. V. E., Bolton A. S., Burles S., Massey R. J., Moustakas L. A., 2007, , 667, 176

Gavazzi R., Treu T., Koopmans L. V. E., Bolton A. S., Moustakas L. A., Burles S., Marshall P. J., 2008, , 677, 1046

Gebhardt K., et al., 2000a, , 119, 1157

Gebhardt K., et al., 2000b, , 539, L13

Gebhardt K., et al., 2003, , 583, 92

Gerhard O. E., 1993, , 265, 213

Gerhard O. E., Binney J. J., 1996, , 279, 993

Gerhard O., Kronawitter A., Saglia R. P., Bender R., 2001, , 121, 1936

Gershtein S. S., Zel'dovich Y. B., 1966, Soviet Journal of Experimental and Theoretical Physics Letters, 4, 120

Gilman D., Birrer S., Treu T., 2020, , 642, A194

Gnedin O. Y., Kravtsov A. V., Klypin A. A., Nagai D., 2004, , 616, 16

Gorenstein M. V., Cohen N. L., Shapiro I. I., Rogers A. E. E., Bonometti R. J., Falco E. E., Bartel N., Marcaide J. M., 1988, , 334, 42

Goullaud C. F., Jensen J. B., Blakeslee J. P., Ma C.-P., Greene J. E., Thomas J., 2018, , 856, 11

Greene J. E., Janish R., Ma C.-P., McConnell N. J., Blakeslee J. P., Thomas J., Murphy J. D., 2015, , 807, 11

Grillo C., 2012, , 747, L15

Grillo C., Lombardi M., Bertin G., 2008, , 477, 397

Grillo C., Gobat R., Lombardi M., Rosati P., 2009, , 501, 461

Hao C. N., Mao S., Deng Z. G., Xia X. Y., Wu H., 2006, , 370, 1339

Herriot G., Morris S., Roberts S., Fletcher J. M., Saddlemyer L. K., Singh G., Veran J.-P., Richardson E. H., 1998, in Bonaccini D., Tyson R. K., eds, Society of Photo-Optical Instrumentation Engineers (SPIE) Conference Series Vol. 3353, Adaptive Optical System Technologies. pp 488–499, doi:10.1117/12.321684

Hildebrandt H., et al., 2017, , 465, 1454

Hubble E. P., 1926, , 64, 321

Hubble E., 1929, Proceedings of the National Academy of Science, 15, 168

Hubble E., Humason M. L., 1931, , 74, 43

Humphrey P. J., Buote D. A., 2010, , 403, 2143

Illingworth G., 1977, , 218, L43

Jeans J. H., 1915, , 76, 70

Jeans J. H., 1922, , 82, 122

Jedrzejewski R. I., 1987, , 226, 747

Józsa G. I. G., Oosterloo T. A., Morganti R., Klein U., Erben T., 2009, , 494, 489

Kaplinghat M., Valli M., Yu H.-B., 2019, , 490, 231

Keeton C. R., Kochanek C. S., 1997, , 487, 42

Kelvin L., 1904, Baltimore Lectures on Molecular Dynamics and the Wave Theory of Light. C.J. Clay and Sons

Kennicutt Robert C. J., 1992, , 79, 255

King I. R., 1978, , 222, 1

Kochanek C. S., 2003, , 583, 49

Kochanek C. S., 2020, , 493, 1725

Komatsu E., et al., 2011, , 192, 18

Koopmans L. V. E., Treu T., Fassnacht C. D., Blandford R. D., Surpi G., 2003, , 599, 70

Koopmans L. V. E., Treu T., Bolton A. S., Burles S., Moustakas L. A., 2006, , 649, 599

Koopmans L. V. E., et al., 2009, , 703, L51

Kormendy J., Djorgovski S., 1989, , 27, 235

Kormendy J., Fisher D. B., Cornell M. E., Bender R., 2009, , 182, 216

Krajnović D., et al., 2011, , 414, 2923

Kuntschner H., et al., 2006, , 369, 497

La Barbera F., Vazdekis A., Ferreras I., Pasquali A., Allende Prieto C., Röck B., Aguado D. S., Peletier R. F., 2017, , 464, 3597

Lagattuta D. J., et al., 2010, , 716, 1579

Larson R. B., 1969, , 145, 405

Larson R. B., 1975, , 173, 671

Law D. R., et al., 2016, , 152, 83

Li R., Shu Y., Wang J., 2018, , 480, 431

Lovell M. R., Frenk C. S., Eke V. R., Jenkins A., Gao L., Theuns T., 2014, , 439, 300

Lovell M. R., Cautun M., Frenk C. S., Hellwing W. A., Newton O., 2021, arXiv e-prints, p. arXiv:2104.03322

Lynden-Bell D., 1967, , 136, 101

Macciò A. V., Dutton A. A., van den Bosch F. C., 2008, , 391, 1940

Martín-Navarro I., La Barbera F., Vazdekis A., Falcón-Barroso J., Ferreras I., 2015, , 447, 1033

McDermid R. M., et al., 2006, , 373, 906

Merritt D., 1987, , 313, 121

Millon M., et al., 2020, , 639, A101

Minor Q., Gad-Nasr S., Kaplinghat M., Vegetti S., 2021, , 507, 1662

Morganti R., et al., 2006, , 371, 157

Mukherjee S., Koopmans L. V. E., Metcalf R. B., Tortora C., Schaller M., Schaye J., Vernardos G., Bellagamba F., 2021, , 504, 3455

Navarro J. F., Frenk C. S., White S. D. M., 1997, , 490, 493

Negroponte J., White S. D. M., 1983, , 205, 1009

Nieto J. L., Bender R., Poulain P., Surma P., 1992, , 257, 97

Nightingale J. W., Hayes R., Dye S., Massey R. J., Frenk C. S., 2018, PyAutoLens: Strong lens modeling, Astrophysics Source Code Library, record ascl:1807.003 (ascl:1807.003)

Nightingale J., et al., 2021, The Journal of Open Source Software, 6, 2825

Nightingale J. W., et al., 2024, , 527, 10480

Nishikawa H., Boddy K. K., Kaplinghat M., 2020, , 101, 063009

Oguri M., 2007, , 660, 1

Oguri M., et al., 2006, , 132, 999

Oldham L. J., Auger M. W., 2016, , 457, 421

Oldham L. J., Auger M. W., 2018, , 476, 133

Oosterloo T., et al., 2010, , 409, 500

Oser L., Ostriker J. P., Naab T., Johansson P. H., Burkert A., 2010, , 725, 2312

Ostriker J. P., Peebles P. J. E., Yahil A., 1974, , 193, L1

Partridge R. B., Peebles P. J. E., 1967, , 147, 868

Pasquini L., et al., 2002, The Messenger, 110, 1

Peng C. Y., Ho L. C., Impey C. D., Rix H.-W., 2010, , 139, 2097

Pilawa J. D., Liepold E. R., Delgado Andrade S. C., Walsh J. L., Ma C.-P., Quenneville M. E., Greene J. E., Blakeslee J. P., 2022, , 928, 178

Poci A., Smith R. J., 2022, , 512, 5298

Poincare H., 1906, Popular Astronomy, 14, 475

Posacki S., Cappellari M., Treu T., Pellegrini S., Ciotti L., 2015, , 446, 493

Powell D. M., Vegetti S., McKean J. P., Spingola C., Stacey H. R., Fassnacht C. D., 2022, , 516, 1808

Quenneville M. E., Liepold E. R., Ma C.-P., 2022, , 926, 30

Read J. I., Steger P., 2017, , 471, 4541

Refsdal S., 1964, , 128, 307

Richstone D. O., Tremaine S., 1984, , 286, 27

Ritondale E., Vegetti S., Despali G., Auger M. W., Koopmans L. V. E., McKean J. P., 2019, , 485, 2179

Rix H.-W., White S. D. M., 1992, , 254, 389

Rix H.-W., de Zeeuw P. T., Cretton N., van der Marel R. P., Carollo C. M., 1997, , 488, 702

Roberts M. S., Rots A. H., 1973, , 26, 483

Romanowsky A. J., Kochanek C. S., 1997, , 287, 35

Romanowsky A. J., Kochanek C. S., 1999, , 516, 18

Rousset G., Fontanella J. C., Kern P., Gigan P., Rigaut F., 1990, , 230, L29

Rubin V. C., Ford W. K. J., Thonnard N., 1978, , 225, L107

Rubin V. C., Ford W. K. J., Thonnard N., 1980, , 238, 471

Rybicki G. B., 1987, in de Zeeuw P. T., ed., IAU Symposium Vol. 127, Structure and Dynamics of Elliptical Galaxies. p. 397, doi:10.1007/978-94-009-3971-4_41

Sandage A., 1961, The Hubble Atlas of Galaxies

Sandage A., Binggeli B., 1984, , 89, 919

Schneider J., Amaro-Seoane P., Spurzem R., 2011, , 410, 432

Schwarzschild M., 1979, , 232, 236

Serra P., et al., 2012, , 422, 1835

Sérsic J. L., 1963, Boletin de la Asociacion Argentina de Astronomia La Plata Argentina, 6, 41

Shajib A. J., Treu T., Agnello A., 2018, , 473, 210

Shajib A. J., et al., 2020, , 494, 6072

Shajib A. J., Treu T., Birrer S., Sonnenfeld A., 2021, , 503, 2380

Sharples R., et al., 2013, The Messenger, 151, 21

Shu Y., et al., 2015, , 803, 71

Slipher V. M., 1913, Lowell Observatory Bulletin, 2, 56

Slipher V. M., 1914, Lowell Observatory Bulletin, 2, 66

Slipher V. M., 1915, Popular Astronomy, 23, 21

Smith R. J., 2020, , 58, 577

Smith R. J., Collett T. E., 2021, , 505, 2136

Smith R. J., Lucey J. R., Conroy C., 2015, , 449, 3441

Sonnenfeld A., Cautun M., 2021, , 651, A18

Sonnenfeld A., Treu T., Gavazzi R., Marshall P. J., Auger M. W., Suyu S. H., Koopmans L. V. E., Bolton A. S., 2012, , 752, 163

Sonnenfeld A., Gavazzi R., Suyu S. H., Treu T., Marshall P. J., 2013, , 777, 97

Sonnenfeld A., Leauthaud A., Auger M. W., Gavazzi R., Treu T., More S., Komiyama Y., 2018, , 481, 164

Sonnenfeld A., Jaelani A. T., Chan J., More A., Suyu S. H., Wong K. C., Oguri M., Lee C.-H., 2019, , 630, A71

Spergel D. N., et al., 2003, , 148, 175

Spergel D. N., et al., 2007, , 170, 377

Spiniello C., Koopmans L. V. E., Trager S. C., Czoske O., Treu T., 2011, , 417, 3000

Spiniello C., Barnabè M., Koopmans L. V. E., Trager S. C., 2015, , 452, L21

Stacey H. R., Powell D. M., Vegetti S., McKean J. P., Fassnacht C. D., Wen D., O'Riordan C. M., 2024, , 688, A110

Statler T. S., 1991, , 102, 882

Ströbele S., et al., 2012, in Ellerbroek B. L., Marchetti E., Véran J.-P., eds, Society of Photo-Optical Instrumentation Engineers (SPIE) Conference Series Vol. 8447, Adaptive Optics Systems III. p. 844737, doi:10.1117/12.926110

Suyu S. H., Marshall P. J., Hobson M. P., Blandford R. D., 2006, , 371, 983

Suyu S. H., Marshall P. J., Auger M. W., Hilbert S., Blandford R. D., Koopmans L. V. E., Fassnacht C. D., Treu T., 2010, , 711, 201

Suyu S. H., et al., 2013, , 766, 70

Thatte N., et al., 2021, The Messenger, 182, 7

Thatte N. A., et al., 2022, in Evans C. J., Bryant J. J., Motohara K., eds, Society of Photo-Optical Instrumentation Engineers (SPIE) Conference Series Vol. 12184, Ground-based and Airborne Instrumentation for Astronomy IX. p. 1218420, doi:10.1117/12.2628834

Thomas J., Saglia R. P., Bender R., Thomas D., Gebhardt K., Magorrian J., Corsini E. M., Wegner G., 2007, , 382, 657

Thomas J., et al., 2011, , 415, 545

Thomas J., Ma C.-P., McConnell N. J., Greene J. E., Blakeslee J. P., Janish R., 2016, , 532, 340

Toloba E., et al., 2014, , 783, 120

Tolstoy E., Hill V., Tosi M., 2009, , 47, 371

Toomre A., Toomre J., 1972, , 178, 623

Tortora C., Napolitano N. R., Cardone V. F., Capaccioli M., Jetzer P., Molinaro R., 2010, , 407, 144

Tortora C., La Barbera F., Napolitano N. R., Romanowsky A. J., Ferreras I., de Carvalho R. R.,

2014, , 445, 115

Trager S. C., Faber S. M., Worthey G., González J. J., 2000, , 119, 1645

Tremaine S., et al., 2002, , 574, 740

Treu T., 2010, , 48, 87

Treu T., Koopmans L. V. E., 2002a, , 337, L6

Treu T., Koopmans L. V. E., 2002b, , 575, 87

Treu T., Koopmans L. V. E., 2004, , 611, 739

Treu T., Koopmans L. V., Bolton A. S., Burles S., Moustakas L. A., 2006, , 640, 662

Treu T., Auger M. W., Koopmans L. V. E., Gavazzi R., Marshall P. J., Bolton A. S., 2010, , 709, 1195

Treu T. L., et al., 2023, The Hubble constant at 1.9% from spatially resolved kinematics of gravitational lens, JWST Proposal. Cycle 2, ID. #2974

Trujillo I., et al., 2006, , 373, L36

Turner H. C., Lovell M. R., Zavala J., Vogelsberger M., 2021, , 505, 5327

Turner H. C., Smith R. J., Collett T. E., 2024, , 528, 3559

Valluri M., Merritt D., Emsellem E., 2004, , 602, 66

Valluri M., Ferrarese L., Merritt D., Joseph C. L., 2005, , 628, 137

Van de Vyvere L., Gomer M. R., Sluse D., Xu D., Birrer S., Galan A., Vernardos G., 2022, , 659, A127

Vanderriest C., Schneider J., Herpe G., Chevreton M., Moles M., Wlerick G., 1989, , 215, 1

Vaughan S. P., Davies R. L., Zieleniewski S., Houghton R. C. W., 2018, , 475, 1073

Vazdekis A., Koleva M., Ricciardelli E., Röck B., Falcón-Barroso J., 2016, , 463, 3409

Veale M., Ma C.-P., Greene J. E., Thomas J., Blakeslee J. P., Walsh J. L., Ito J., 2018, , 473, 5446

Vegetti S., Koopmans L. V. E., 2009, , 392, 945

Vegetti S., Koopmans L. V. E., Bolton A., Treu T., Gavazzi R., 2010, , 408, 1969

Verde L., Treu T., Riess A. G., 2019, Nature Astronomy, 3, 891

Visvanathan N., Sandage A., 1977, , 216, 214

Vogelsberger M., Zavala J., Loeb A., 2012, , 423, 3740

Vogelsberger M., Zavala J., Schutz K., Slatyer T. R., 2019, , p. 346

Walsh D., Carswell R. F., Weymann R. J., 1979, , 279, 381

Warren S. J., Dye S., 2003, , 590, 673

Weijmans A.-M., et al., 2009, , 398, 561

Weymann R. J., Latham D., Angel J. R. P., Green R. F., Liebert J. W., Turnshek D. A., Turnshek D. E., Tyson J. A., 1980, , 285, 641

White S. D. M., Rees M. J., 1978, , 183, 341

York D. G., et al., 2000, , 120, 1579

Young C. K., Currie M. J., 1994, , 268, L11

Young L. M., et al., 2011, , 414, 940

Zavala J., Vogelsberger M., Walker M. G., 2013, , 431, L20

Zavala J., Lovell M. R., Vogelsberger M., Burger J. D., 2019, , 100, 063007

Zhao H., 1996, , 278, 488

Zwicky F., 1933, Helvetica Physica Acta, 6, 110

Zwicky F., 1937, Physical Review, 51, 290

de Lorenzi F., Debattista V. P., Gerhard O., Sambhus N., 2007, , 376, 71

de Vaucouleurs G., 1948, Annales d'Astrophysique, 11, 247

de Vaucouleurs G., 1959, Handbuch der Physik, 53, 275

de Zeeuw P. T., et al., 2002, , 329, 513

van Dokkum P., Conroy C., Villaume A., Brodie J., Romanowsky A. J., 2017, , 841, 68

van de Ven G., Falcón-Barroso J., McDermid R. M., Cappellari M., Miller B. W., de Zeeuw P. T., 2010, , 719, 1481

van den Bosch F. C., 1997, , 287, 543

van den Bosch R. C. E., 2016, , 831, 134

van den Bosch R. C. E., van de Ven G., Verolme E. K., Cappellari M., de Zeeuw P. T., 2008, , 385, 647

van den Bosch R. C. E., Gebhardt K., Gültekin K., van de Ven G., van der Wel A., Walsh J. L., 2012, , 491, 729

van der Marel R. P., Cretton N., de Zeeuw P. T., Rix H.-W., 1998, , 493, 613

APPENDIX A

Resolution and binning effects

The dynamical analysis presented in Chapter 5 is performed using the standard JAM treatment commonly employed for $z \sim 0$ galaxies, which typically have higher-resolution data than the data presented in this thesis. We therefore use mock MUSE observations to assess the degree to which the resolution and binning of our observations affect the recovered parameters.

We generate two synthetic data sets; the first set has properties similar to our best-fitting free γ model from Chapter 5, and the second set represents an alternative case to test the recovery of parameters in a 'vanilla' scenario with no excess central mass and an NFW-like DM halo. To generate these data sets, shown in Figure A.1, we bin our best-fitting and vanilla models following the same Voronoi binning scheme described in Section 2.1.3. The binned $v_{\rm rms}$ field of each model is convolved with the $v_{\rm rms}$ error from our multiple component fitting from Section 5.2. The posterior PDF for the model parameters is sampled via a MCMC Ensemble sampler, following the techniques described in Chapter 5, and the likelihood of our mock data $v_{\rm rms}$ is maximised. The marginalized parameter constraints and input 'truth' parameters are shown in Figure A.2 and summarised in Table A.1.

We find that the input parameters used to generate both models, with the exception of $m_{\rm cen}$ for the 'vanilla' mock data, are indeed recovered without bias from any smoothing effects, albeit with errors that are unavoidably larger than they would be for a more nearby

Table A.1
The median and 68% confidence bounds for the recovered model parameters from our mock data.

Model		γ	β	$f_\star$	$m_{\rm cen}[10^9 {\rm M}_\odot]$	$i[^\circ]$
Best	Input	1.73	−0.03	0.38	8.23	64
	Recovered	$1.63^{+0.24}_{-0.31}$	$-0.02^{+0.03}_{-0.03}$	$0.42^{+0.17}_{-0.26}$	$10.16^{+2.38}_{-3.37}$	64^{+16}_{-14}
Vanilla	Input	1	0	0.71	0	64
	Recovered	$0.94^{+0.27}_{-0.22}$	$0.02^{+0.04}_{-0.03}$	$0.72^{+0.04}_{-0.06}$	$1.31^{+1.46}_{-0.92}$	62^{+17}_{-14}

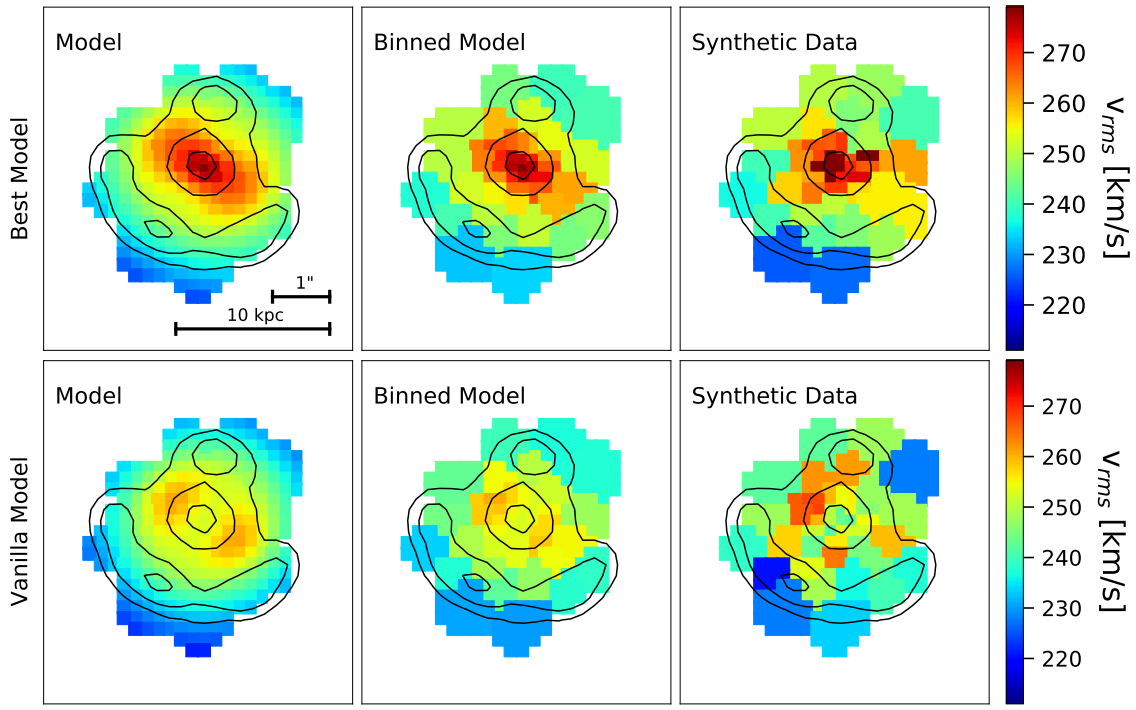

Figure A.1

Kinematic maps showing the $v_{\rm rms}$ fields of the synthetic data. We show two models, one created from the best-fitting free γ model and one representing a 'vanilla' scenario with no excess central mass and an NFW-like halo. The left hand panel shows the high resolution model, the middle panel is the noise-free spatially binned model and the third is the synthetic model after adding observational noise.

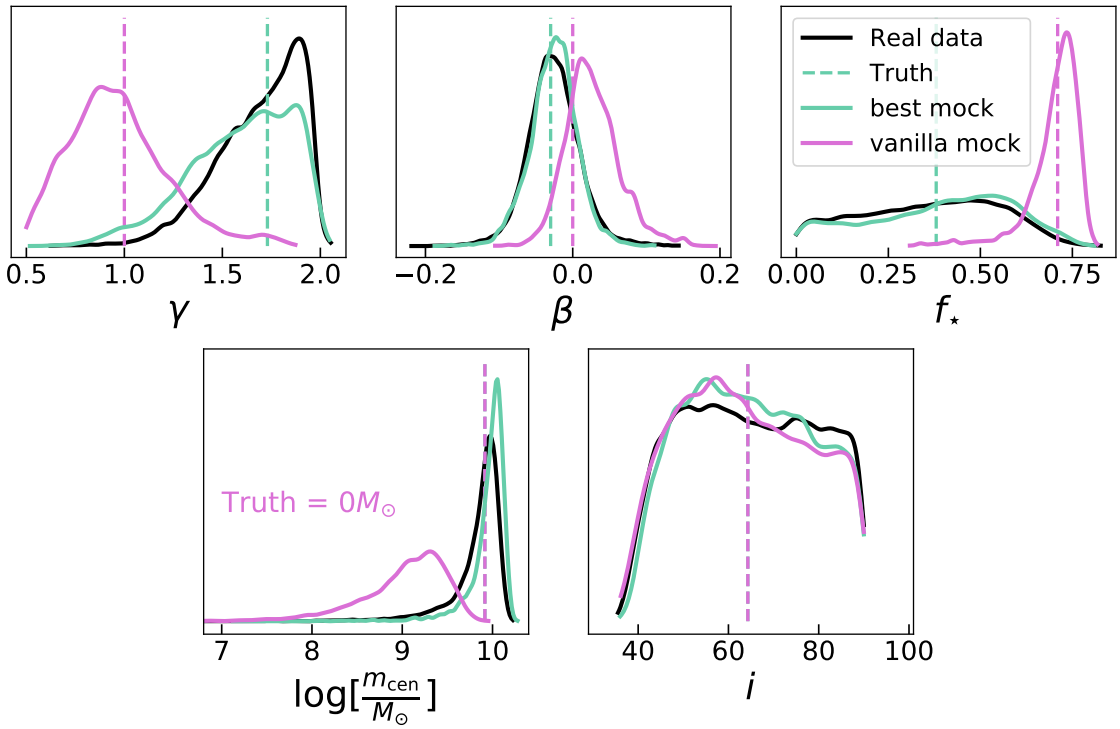

Figure A.2

The marginalised posterior densities for each parameter for the real data and the two sets of mock data, generated from the 'best' and 'vanilla' models. The dashed line represents the 'truth' value used to generate the mock data. The parameters explored are: the inner slope of the DM density profile, γ; the orbital anisotropy parameter, β; the stellar mass as a fraction of the total lensing mass, $f_\star$; any central mass in excess of a constant stellar mass-to-light ratio, $m_{\rm cen}$; the galaxy inclination, i.

galaxy. In the case of the 'vanilla' mock data, in the absence of any real point mass or centrally concentrated mass in excess of a constant $M/L_\star$, the recovered excess central mass is of the order $10^9 M_\odot$ and an order of magnitude smaller than what is recovered from the real data. This value falls below the threshold at which any real central excess mass could be confidently detected. Our synthetic data were generated from JAM predictions of the combined second moment, and therefore implicitly incorporate both the velocity and velocity dispersion. A more sophisticated treatment modelling both components consistently would be needed to address beam-smearing effects at the galaxy centre. However, given the relatively small contribution of the ordered rotation to the second moment for this specific galaxy, it is unlikely to have a significant impact on the results presented in this work. We thus conclude that the central mass recovered from the real data is not an artifact of smoothing or binning effects, but rather reflects the intrinsic properties of the system.